

# The Geometric Basis of Epithelial Convergent Extension

Reviewed Preprint

v2 • July 29, 2024

Revised by authors

Reviewed Preprint

v1 • March 26, 2024

Fridtjof Brauns , Nikolas H Claussen, Matthew F Lefebvre, Eric F Wieschaus, Boris I Shraiman 

Kavli Institute for Theoretical Physics, University of California Santa Barbara, Santa Barbara, California 93106, USA

• Department of Physics, University of California Santa Barbara, Santa Barbara, California 93106, USA •

Department of Molecular Biology, Princeton University, Princeton, NJ, USA; The Lewis-Sigler Institute for Integrative Genomics, Princeton University, Princeton, NJ, USA

 [https://en.wikipedia.org/wiki/Open\\_access](https://en.wikipedia.org/wiki/Open_access) Copyright information

## Abstract

Shape changes of epithelia during animal development, such as convergent extension, are achieved through concerted mechanical activity of individual cells. While much is known about the corresponding large scale tissue flow and its genetic drivers, fundamental questions regarding local control of contractile activity on cellular scale and its embryo-scale coordination remain open. To address these questions, we develop a quantitative, model-based analysis framework to relate cell geometry to local tension in recently obtained timelapse imaging data of gastrulating *Drosophila* embryos. This analysis provides a systematic decomposition of cell shape changes and T1-rearrangements into internally driven, active, and externally driven, passive, contributions. Our analysis provides evidence that germ band extension is driven by active T1 processes that self-organize through positive feedback acting on tensions. More generally, our findings suggest that epithelial convergent extension results from controlled transformation of internal force balance geometry which combines the effects of bottom-up local self-organization with the top-down, embryo-scale regulation by gene expression.

### eLife assessment

This **important** study analyzes in an original way how tension pattern dynamics can reveal the contribution of active versus passive intercalation during tissue elongation. The authors develop a **compelling**, elegant analytical framework (isogonal tension decomposition) to disentangle the passive (adjacent tissues pulling) and active (local tension anisotropy) contributions to intercalation events. This allows the generation of global maps of tissue mechanics that will be extremely helpful in the field of biomechanics.

<https://doi.org/10.7554/eLife.95521.2.sa3>

## Introduction

Tissue elongation is one of the basic processes of morphogenesis. Tissues can elongate by oriented cell divisions and growth [1, 2], or via local rearrangements of cells. The latter happens during epithelial “convergent extension” – a common motif of early development and organogenesis in many organisms – where an epithelium elongates along one axis while contracting along the perpendicular direction [3]. Epithelial convergent extension exemplifies the important role of cell and tissue mechanics in morphogenetic processes, which must be studied alongside developmental genetics and signaling. The fundamental question of developmental mechanics is how force generation is coordinated across cells to produce a coherent morphogenetic outcome.

The *Drosophila* embryo is one of the best-established models of developmental mechanics as it is ideal for live imaging and offers an extensive set of genetic tools [4]. Progress in live imaging and computational image analysis has produced remarkably quantitative data [5, 6]. In this work, we will take advantage of a previously published dataset which we will reanalyze and use as test-bed for theory development. **Figure 1** recapitulates the basic quantitative features of germ band elongation (GBE) during *Drosophila* embryogenesis based on the light-sheet imaging data from [6, 7] which, thanks surface extraction [8] and cell segmentation and tracking [7], provides a global picture of tissue dynamics with cellular resolution. During *Drosophila* gastrulation, the embryonic blastoderm (an epithelial monolayer of about 6000 cells on the surface of the embryo) undergoes dramatic deformation that changes tissue topology and gives rise to the three germ layers [9]. Gastrulation starts (see **Fig. 1A**) with the formation of the Ventral Furrow (VF) which initiates the internalization of mesoderm, followed immediately by Germ Band Extension (GBE), which involves convergent extension of the lateral ectoderm (or germ band) and the flow of tissue from the ventral onto the dorsal side of the embryo [10–12] (see Movie 1). Simultaneous to GBE, the Posterior MidGut (PMG) moves from the posterior pole towards the anterior on the dorsal side of the embryo and invaginates progressively as it moves.

VF and PMG invagination and GBE have been extensively studied, leading to the identification of relevant developmental patterning genes [10–13]. Live imaging has also uncovered the pertinent cell behavior of GBE, namely intercalation of neighboring cells in the lateral ectoderm [13–15]. The elementary step of this cell rearrangement process is called a T1 transition. It involves a quartet of cells where two cells lose contact and the two other cells gain contact (see **Fig. 1B**, bottom). The role of intercalations is highlighted by a “tissue tectonics” [16] analysis, which decomposes the tissue strain rate into cell-level contributions: cell-shape deformation and cell rearrangement (see **Fig. 1B** and **Fig. S1B**). During VF invagination, cells in the lateral ectoderm are stretched along the DV axis with little rearrangement (**Fig. S1A**). Subsequently, during GBE, the lateral ectoderm (i.e. the germ band) extends (**Fig. 1D**) by cell rearrangements with very little cell elongation (**Fig. 1C**, bottom; and **Fig. S1B** and **D**). By contrast, the dorsal tissue (which will become the amnioserosa) deforms in the opposite orthogonal as the germ band, by a combination of cell shape changes and rearrangements (**Fig. 1C**, top; and **Fig. S1C**). Overall, we find that the majority of cell rearrangements happen via T1s (**Fig. 1E** and **E'**) with only a small number of “rosettes” (which involve more than 4-cells transiently sharing a vertex) being formed. This prevalence of T1s is consistent with previous analysis ([7, 17]) with the high coordination of rearrangements that is apparent in the lateral ectoderm (**Fig. 1C**, bottom).

While the above tissue tectonics analysis reveals the cell scale “kinetics” during GBE, it does not address the fundamental question of the underlying driving forces. Intercalations are associated with localized activity of the force generating protein non-muscle myosin II [12, 14, 15] (henceforth simply “myosin”). However, the relative contribution of such locally generated forces vs pulling by adjacent tissues, such as the invaginating PMG remain debated. Previous studies

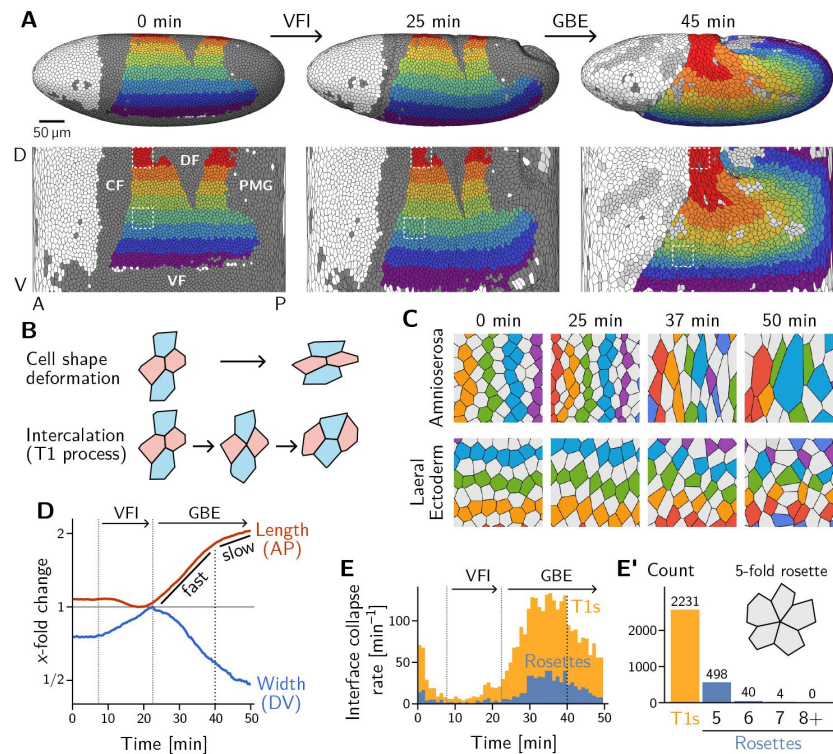


**Figure 1**

**Light sheet imaging, segmentation, and tracking [7] provides a global picture of the cell level contributions to tissue flow (“tissue tectonics” [16]) during *Drosophila* gastrulation.**

**A** Segmented and tracked cells on the ellipsoidal surface of the early *Drosophila* embryo in 3D (top) and projected into the plane (bottom) using a cartographic projection [8]; imaging, segmentation and tracking data from Ref. [7]. Trunk cells are colored in bands along the DV axis to illustrate the major tissue deformations during early development of *Drosophila*: ventral furrow invagination (VFI, 25 min) and germ band extension (GBE, 45 min). The purple to green regions constitute the lateral ectoderm (germ band) which contracts along the DV axis and extends along the AP axis. The posterior part of the germ band moves over the pole as it extends. The red and orange regions constitute the amnioserosa, which contracts along the AP axis and extends along the DV axis. Cells that are internalized in folds are shaded in dark gray (CF: Cephalic furrow; DF: Dorsal folds; VF: Ventral furrow; PMG: posterior midgut). Only one side of the left-right symmetric embryo is shown but both sides were analyzed throughout the manuscript. **B** Tissue deformation is the sum of cell shape changes (top) and cell rearrangements (bottom). The elementary cell rearrangement is a T1 transition in a quartet of cells. The interface between the red cells collapses, giving rise to a transient four-fold vertex configuration (center). The four-fold vertex then resolves to form a new interface between the blue cells. **C** Colored, tracked cells illustrate the cell rearrangements and shape changes in the amnioserosa (top) and lateral ectoderm (bottom). While amnioserosa cells show large deformations and little coordination in their rearrangement, cell intercalations in the lateral ectoderm appear highly choreographed. (ROI size  $40 \times 40 \mu\text{m}^2$ .) **D** Convergence and extension of the lateral ectoderm (x-fold change defined relative to the minimum length and maximum width respectively). During VFI, the lateral ectoderm is stretched along DV axis and slightly contracts along the AP axis. GBE has an initial fast phase before slowing down at around 40 min. **E** and **E'** Rate of interface collapses serves as a measure for the cell intercalation rate. During VFI, there are few intercalations. During GBE, the majority of intercalations are T1 transitions, while rosettes, rearrangements involving more than four cells, contribute significantly less to tissue deformation (E'). At 40 min, there is a noticeable drop in the T1 rate, marking the transition to the slow phase of GBE. Intercalation events before  $t = 12$  min were excluded from the subsequent analysis.

addressing this key question on the tissue level have come to conflicting conclusions [13–22]. A second key question is how myosin dynamics is controlled on a cellular level and how it is orchestrated across cells to create a coherent global morphogenetic flow. Myosin recruitment depends on the expression of key developmental genes [11–14, 23], and, in addition, is subject to positive and negative mechanical feedback that depends on the stress [24, 25] and the rate of strain (rate of cell deformation) [26]. Despite considerable understanding of the genetic and cell-biological components involved in GBE, the relative roles of the genetic pre-pattern (top down) vs local “self-organization” of myosin activity via mechanical feedback loops (bottom up) are still not clear. All of these questions call for a coherent theoretical framework that allows interpreting and reconciling existing experimental findings.

Our approach is based on the assumption of force balance of stresses concentrated in the cell cortices. Intercellular adhesion effectively links the cytoskeletons of neighboring cells, so that a two dimensional epithelial sheet constitutes a transcellular mechanical network put under tension by myosin motors. This internal tension is revealed by laser ablation of cell interfaces, which causes rapid recoil [27]. Cortical force balance provides a direct link between mechanics and geometry: It allows inference of tensions from the angles at the vertices where interfaces meet [28–30], which we utilize to identify from images the stereotyped local geometry and tension dynamics associated with internally driven (active) and externally driven (passive) cell rearrangements (T1s).

The capacity of epithelial tissue to support tension makes it markedly different from passive fluids [31]. How one can reconcile the solid-like capacity of an epithelial monolayer to support tension (as well as shear stress) with its ability to change shape and rearrange internally like a fluid is intimately linked to the fundamental question of internal vs external driving. Our findings suggest that morphogenetic flow of epithelia can be understood as adiabatic deformation of cell array geometry controlled by changes in the internal state of tension. In other words, the tissue behaves as a plastically deforming *active solid* rather than a fluid. Based on these insights, we provide evidence and a minimal model for self-organization of the internally driven cell rearrangements via a local mechanical feedback mechanism. This model reproduces the experimentally observed dynamics on the level of cell quartets and forms the basis for a predictive tissue-scale model that is formulated in a companion paper [32]. Finally, we address how cellular behaviors (shape changes and intercalations) are coordinated across the tissue to generate coherent tissue flow. We will show that coordination of active T1 events among neighboring cells involves a characteristic pattern of cortical tensions which we quantify by introducing the “Local Tension Configuration” (LTC) order parameter. In the companion paper [32], we employ this order parameter to quantitatively compare tissue-scale simulations with experimental data on the cell scale. Taken together, our findings identify the dominant role of active internal tension in the lateral ectoderm in driving the embryo scale flow and suggest mechanical feedback as the mechanism for self-organization on the cell-scale.

## Results

### Force balance and cell geometry in an epithelial monolayer

We begin by laying out the assumptions and concepts that underlie our framework. Epithelial tissues are under internally generated tension, which is revealed by recoil in response to laser ablation. The timescale of this recoil ( $\sim 10$  s) on the scale of cells is at least 10-fold faster than the timescale of local tissue flow [33, 34], so that the tissue can be regarded as being in approximate mechanical equilibrium. This suggests that the apparent tissue flow can be understood in terms of adiabatic remodelling of a quasistatic force balance network [30]. This view contrasts with regular fluid flow, where externally or internally generated forces are balanced by viscosity or substrate friction.

We further assume that mechanical stress in the epithelium is primarily carried by the adherens-junctional cytoskeleton, which resides on cell interfaces. This is supported by the observation that cell-cell interfaces in the *Drosophila* blastoderm are mostly straight. Cells are attached to their neighbors via adherens junctions that are linked to the junctional cytoskeleton in each cell (Fig. 2A) [35]. The myosin motors exert a contractile force on the actin fibers and thereby keep the cortex under active tension ( $T$ ), which we refer to as “cortical tension” [36]. Together, the adherens junctions define a tissue-wide mechanical structure, capable of (i) generating locally controlled internal tension and (ii) adaptively remodelling its architecture. The *Drosophila* blastoderm lies on top of a fluid yolk [37] which exerts negligible drag forces on tissue motion on the surface [38], suggesting that all forces are balanced within the epithelial layer.

Concentration of tension in interfaces tightly links force balance with the readily observable geometry of cell-cell interfaces. Force balance requires that the forces  $T_{ab}$  exerted by the cortical tensions sum to zero at each vertex where three (or more) interfaces meet. (Here, the indices  $a, b$  label the two cells that meet at a interface; see Fig. 2A.) These force-balance constraints relate the *relative* tension on cell interfaces at a vertex to the angles at which the interfaces meet [28]. This link of hard-to-observe cortical tensions to the readily observable local cell geometry enables tension inference methods which have been extensively validated by computational robustness checks [29], direct comparison with measured laser ablation recoils [39] and by correlation with local myosin abundance [30].

Crucially, the link between force balance and the geometry of the cell array goes beyond inference and to the very basis of our proposed mechanism of tissue flow. Force balance implies that tension vectors meeting at a vertex sum to zero and hence form a closed triangle [31], as illustrated in Fig. 4B. The angles of this triangle are complementary to the corresponding angles at which the interfaces meet. (This becomes evident by rotating each triangle edge by 90°. Two angles are complimentary if they sum to 180°) As adjacent vertices share an interface, the corresponding tension triangles must share an edge: the tension triangles form a triangulation, i.e. fit together to form a tiling of the plane. The triangulation is dual to the cell array: For each cell, there is a corresponding vertex in the tension triangulation (Fig. 4B'). It reflects the fact that the force-balance conditions at neighboring vertices are not independent because they share the interface that connects them. (Dual force tilings go back to Maxwell [40] and have been applied to the statics of beam assemblies [41] and granular materials [42].) This triangulation establishes a geometric structure in tension space. Force balance requires that the angles at vertices in the physical cell array are complementary to those in the tension triangulation. This intimately links tension space and epithelial geometry in real space. Myosin-driven local changes in tension change the shapes of tension-space triangles and hence remodel the tension triangulation. The induced changes in the geometry of the cell array drive both the local rearrangement of cells and the global tissue flow. The remainder of the Results section will provide quantitative data analysis and modelling that will work out the above ideas and their implications.

## Cell scale analysis

To map out the relative tensions in the tissue, we perform *local* tension inference for each interface relative to its four neighbors. Geometrically in tension space, the local tension configuration is represented by two adjoined tension triangles forming a kite (see Fig. 2B) and the inference is a simple application of the law of sines on the two triangles (see SI Sec. 1.4).

**Figures 2C** and C' show snapshots from this local tension inference in the dorsal ectoderm (amnioserosa) and the lateral ectoderm (germ band) respectively. Initially, relative tensions are close to unity throughout the embryo, since the cell array is approximately a hexagonal lattice, with vertex angles close to 120°. As gastrulation progresses, the cortical tensions change and one starts to see characteristic differences between the dorsal ectoderm and the lateral ectoderm. In the former, interfaces that contract remain under approximately constant tension while interfaces oriented parallel to the direction of tissue stretching (i.e. along the DV axis) extend and are under increasing tension (Fig. 2C). A very different picture emerges in the lateral ectoderm, where one

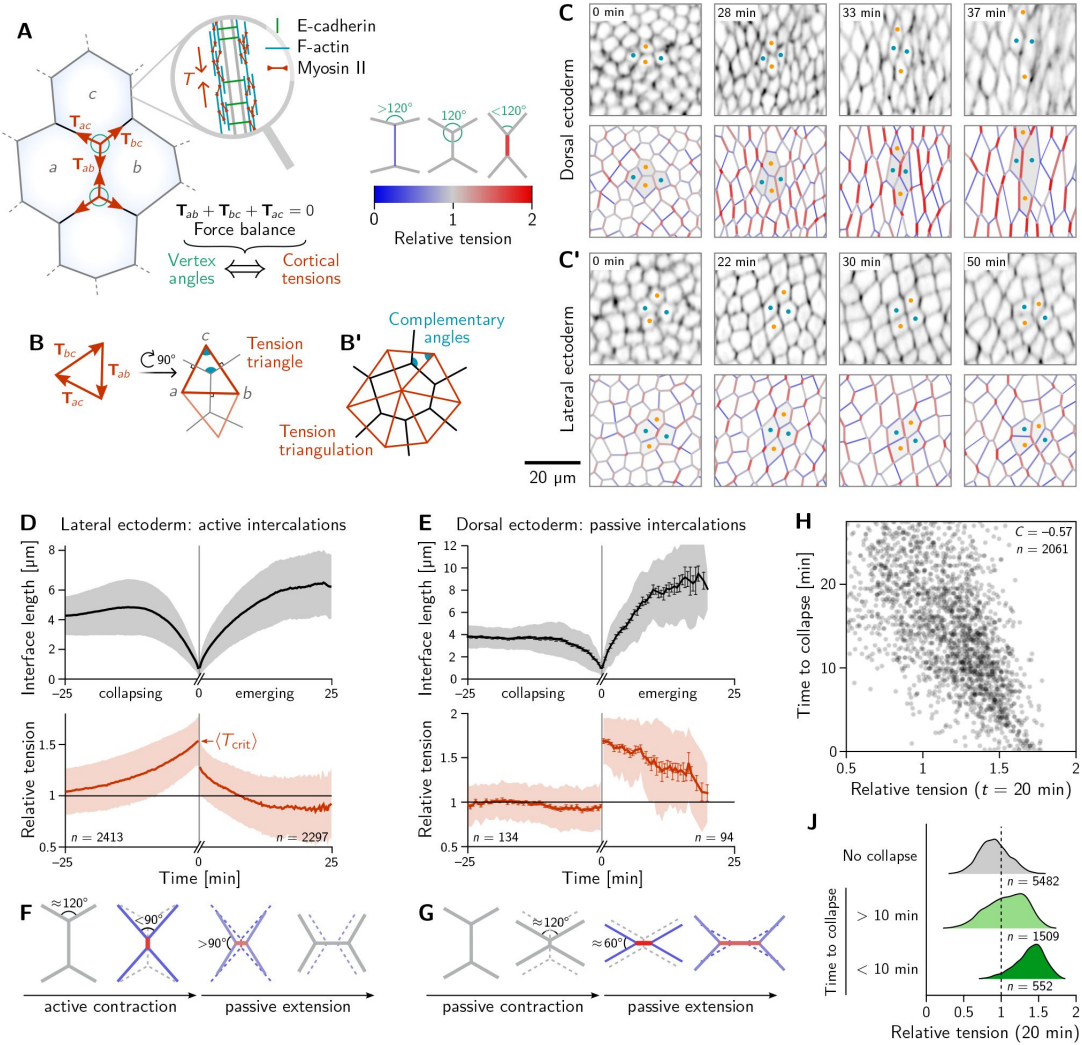


**Figure 2**

### Inferred tension dynamics distinguishes active and passive T1s.

**A** The adherens-junctional cytoskeleton ion in the cortex at cell-cell interfaces via active motors (inset). In force balance, the forces  $T_{ab}$  exerted on a ows) must sum to zero. This allows inferring the relative cortical tensions from the angles at which the interfaces x (see colorbar). **B** and **B'** The angles in the *tension triangles* formed by the force vectors (rotated by 90°) are to the interface angles at the vertex. Tension triangles corresponding to adjacent vertices share an edge and gether to form a *tension triangulation* (B'). **C** and **C'** Relative tensions inferred (bottom) from cell membrane the amnioserosa (C) and in the lateral ectoderm (C'). In the lateral ectoderm, high tension interfaces contract. ttern of alternating high and low tension interfaces therefore leads to coordinated T1s (cf. Fig. 1C), bottom). ge dots mark an intercalating quartet. **D** and **E** While active and passive T1s show similar dynamics of the ner edge (top), they are markedly different in their tension dynamics (bottom). For lateral cells (D), the tension e interface contracts, providing evidence that positive tension feedback actively drives the edge contraction. For, the relative tension remains constant on the contracting edge, indicating that the intercalations are passive. at time zero result from the relation between the angles before and after the neighbor exchange. Collapsing and aces were tracked and analyzed separately (see SI Sec. 1.3). Bands and fences show SD and SEM respectively; is smaller than the line thickness. **F** The increasing tension of the contracting edge during an active T1 causes osite of the central interface to become increasingly acute. **G** The hallmark of passive T1s are constant cortical hus vertex angles) before the neighbor exchange. This geometrically fixes the vertex angles after the neighbor that the emerging edge is under high tension. **H** and **J** In the lateral ectoderm, relative tension predicts time collapses (H) and high relative tension predicts which interfaces collapse (J); see Fig. S4 for analogous plots erosa where no such correlation is observed. Relative tensions were averaged from minute 20 to 21 (over four timepoints), i.e. at the end of VFI (cf. Fig. 1E).

observes an alternating pattern of high and low tensions before intercalations start (22 min). The high tension interfaces contract, leading to coordinated T1 transitions (30 min, cf. **Fig. 2C** and Movie 2). As GBE transitions from the fast phase to the slow phase at around 40 min, the pattern of tensions becomes more disordered. We will return to the pattern of local tension configurations below in the discussion of tissue scale dynamics.

The differences in the patterns of inferred tension in the amnioserosa compared to the lateral ectoderm suggest very distinct mechanisms for cell intercalations in these two tissue regions, matching the fact that their levels of cortical myosin are very different (high in the lateral ectoderm, low in the amnioserosa [18]). In the following, we first focus on intercalating cell quartets to quantitatively analyze these different mechanisms. A quantitative understanding of the cell-scale dynamics will then form the basis for bridging to the tissue scale.

## Relative tension dynamics distinguishes active and passive intercalations

We identify all cell quartets which undergo neighbor exchanges (T1 processes), calculate the length and relative tension of all collapsing and emerging interfaces and align the data to the time of the neighbor exchange [43]. Pooling the data for each of the bands of cells colored in **Fig. 1A**, we find two distinct scenarios for ventro-lateral quartets and dorsal quartets (**Fig. 2D** and **E**; for a breakdown by individual bands, see **Fig. S3**).

The length dynamics of collapsing and extending interfaces in the amnioserosa and the lateral ectoderm is qualitatively similar (**Fig. 2D** and **E**). In the lateral ectoderm, there is a slight increase in interface length preceding contraction. This transient stretching is caused by the VF invagination that precedes GBE [26].

By contrast, the tension dynamics is markedly different between the amnioserosa and the lateral ectoderm. In the lateral ectoderm, the tension on the contracting edge grows non-linearly and reaches its maximum just before the neighbor exchange. In terms of the local cell geometry, this increasing relative tension reflects the fact that the angles facing away from the interface decrease as the interface contracts (**Fig. 2F**). Notably, the non-linearly increasing tension, concomitant with an accelerating rate of interface contraction, is evidence that positive tension feedback plays a role in myosin recruitment [24, 25, 44] and is in excellent agreement with predictions from a recent model where such feedback is a key ingredient [45]. From the data shown in **Fig. 2D** we can read off the average relative tension threshold ( $T_{\text{crit}}$ ) =  $1.530 \pm 0.005$  for interface collapse. As we will see further below, this threshold can be predicted from simple geometric considerations.

The correlation between increasing tension and interface contraction during active T1s can be used to predict active T1s. Indeed, plotting the time to interface collapse against the relative tension for quartets in the lateral ectoderm shows a clear negative correlation (**Fig. 2H**). Conversely, relative tensions below 1 correlate with interfaces that never collapse (**Fig. 2J**).

After the neighbor exchange, the relative tension on the new interface starts at a lower value and then continues decreasing back to 1, corresponding to vertex angles of  $120^\circ$ . Because **Figs. 2D** and **E** show tensions on the collapsing edge for  $t < 0$  and on the emerging edge for  $t > 0$ , there is no reason why the tension should be continuous at  $t = 0$ . The apparent jump in relative tension is a consequence of geometry: Because the angles facing away from the interface are  $< 90^\circ$  before the neighbor exchange, they are necessarily  $> 90^\circ$  afterwards. This implies that a relative tension  $> \sqrt{2}$  on the collapsing interface is necessarily followed by a tension  $< \sqrt{2}$  on the new interface.

Let us now turn to T1s in the amnioserosa. Here, the relative tension on the inner edge remains almost constant near 1 prior to the neighbor exchange, i.e. the vertex angles remain close to  $120^\circ$  (see [Fig. 2G](#)). As a consequence of this tension homeostasis on collapsing interfaces, there is no correlation between relative tension and the time until the interface collapses in the amnioserosa (see [Fig. S4](#)). On the new interface emerging after the neighbor exchange, tension is high and remains constant for an extended period. Again, the tension apparent jump across the neighbor exchange is a consequence of geometry. Just before the neighbor exchange, the vertex angles are close to  $120^\circ$  which implies that the angles facing away from the interface are  $60^\circ$  after the neighbor exchange (see [Fig. 2G](#)). This corresponds to a relative tension of  $\sqrt{3} \approx 1.73$  on the central interface. Just before the neighbor exchange the vertex angles are close to  $120^\circ$  which implies that the angles facing away from the interface are  $60^\circ$  after the neighbor exchange (see [Fig. 2G](#)). This corresponds to a relative tension of  $\sqrt{3} \approx 1.73$  on the emerging central interface.

To understand the high tension observed on emerging interfaces, recall that tension inference only yields the *total* tension, but not on how this tension is generated in the cytoskeleton. On an extending junction, tension carried by passive crosslinkers will add to the tension generated by myosin. The passive tension rapidly relaxes as crosslinkers turn over, giving an effective viscoelastic relaxation timescale on the order of minutes [46]. This passive tension relaxation is a crucial ingredient in the model presented below. In the amnioserosa, the high tension is sustained for a longer time because the tissue there is continually getting stretched as the germ band contracts along the DV axis. Indeed, increased tension is also found in interfaces that start out DV oriented (cf. [Fig. 2C](#)).

### Minimal model based on tension feedback reproduces length and tension-dynamics of T1s

Tension inference and the pooled analysis of T1 events has revealed the cortical tension dynamics on cell-cell interfaces during active and passive cell intercalations. The behavior of cortical tensions differs significantly between distinct spatial regions of the embryo and, on first glance, appears quite counter-intuitive. In particular, it is very different from that of springs or rubber bands: the length and tension of a spring are tied to one another by a constitutive relationship. By contrast, both the length and tension of cell-cell interfaces can change independently and are actively regulated by turnover of junctional proteins (such as actin, myosin and E-cadherin).

These observations call for a new modeling approach, where tension are not governed by constitutive relationships such as the typical area-perimeter elasticity of the vertex model [47, 48]. Instead, our model directly builds on the same assumptions that underlie the tension inference: dominant cortical tensions that are in adiabatic force balance. The dynamics resides in the changes in tension governed by mechanical feedback.

To keep the number of parameters and variables (degrees of freedom) in the model to a minimum, we consider a quartet of cells with identical shapes. This describes a representative quartet in a periodic cell array. Such a cell array is characterized by the three angles at each vertex,  $\varphi_i$ , and the three interface lengths  $\ell_i$  with  $i \in \{0, 1, 2\}$  (see [Fig. 3A](#)). The vertex angles are determined by the relative cortical tensions  $T_i$  via the condition of force balance (see [Fig. 4A](#)). Motivated by the nonlinearly increasing tension observed on contracting interfaces (cf. [Fig. 2D](#)), we equip each interface with self-reinforcing tension dynamics

$$\tau_T \partial_t T_i = T_i^n - \frac{1}{3} \sum_k T_k^n, \quad (1)$$

which models tension-induced myosin recruitment [24] (with excitability exponent  $n$  set to  $n = 4$  in our simulation). The dynamics conserves the total active tension  $\sum_i T_i$ , corresponding to a finite myosin pool in each cell. (Other choices for fixing the overall scale of tension, e.g. via the triangle

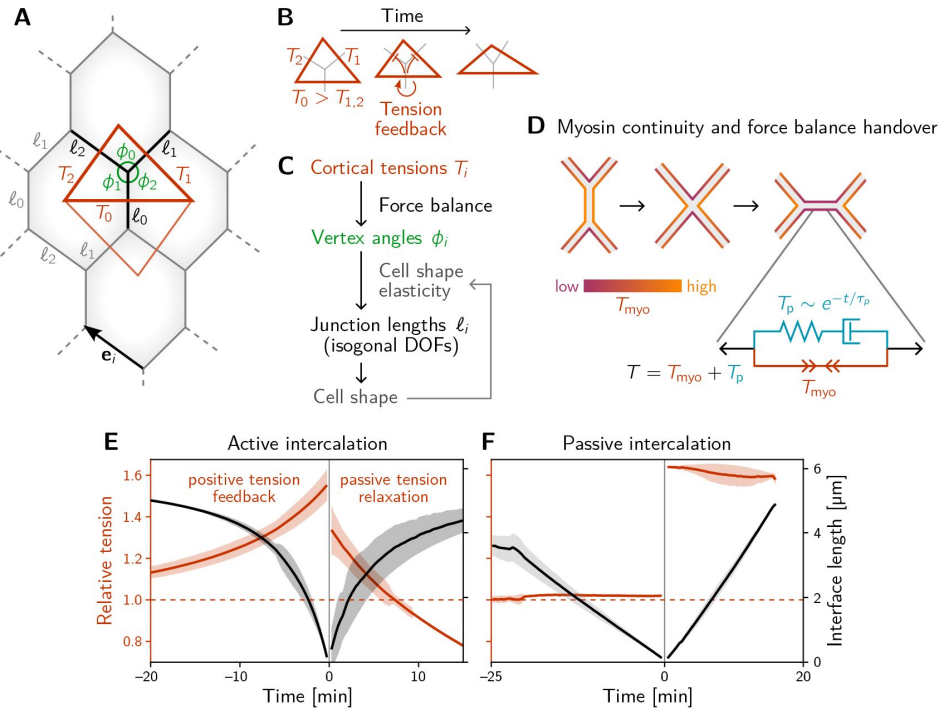


**Figure 3**

**A minimal model for positive tension feedback reproduces the signatures of active T1s, and creates passive T1s when feedback is turned off.**

**A** Single cell quartet of identical cells forms the elementary setting for modelling T1s. This geometry is characterized by two vertex angles ( $\phi_0$ ,  $\phi_1$ , and  $\phi_2 = 2\pi - \phi_0 - \phi_1$ ) and three interface lengths ( $\ell$ ). The interface angles are determined by the pair of identical tension triangles corresponding to the cell quartet. To avoid boundary effects, the cell quartet and tension triangles are set up to tile the plane periodically as a regular lattice. **B** Positive tension feedback causes the longest edge in a tension triangle to grow at the expense of the shorter two edges, thus deforming the triangle to become increasingly obtuse. (We fix the total tension scale. In real cells, the overall tension scale is set by the available myosin pool. Relative tensions change as myosin is redistributed between the cortex at different interfaces.) **C** The tension triangle shape determines the vertex angles,  $\phi_i$ . To fix the interface lengths  $\ell_i$ , we determine the cell shape by minimizing an elastic energy while keeping angles fixed (see SI for details). **D** Two-sided architecture of junctional cortex determines myosin level on newly formed interface. Sketch of intercalating quartet with myosin in each cell's cortex color-coded. After a neighbor exchange, the active tension (i.e. myosin level) on the new edge is determined by a “handover” mechanism that assumes continuity of myosin concentration at vertices within each cell. As consequence, the active tension on the new edge right after the neighbor exchange is below the total tension that is determined by geometry. This tension imbalance causes the new edge to extend by remodeling. To capture the remodeling, we introduce a passive viscoelastic tension  $T_{\text{passive}}$  due to passive cortical crosslinkers.  $T_{\text{passive}}$  decays exponentially with a characteristic remodeling time  $\tau_p$ . Notably, no additional active ingredients (like medial myosin contractility) are required to drive extension of the new edge. **E and F** The model reproduces the signatures of active and passive T1s observed in the *Drosophila* embryo. The tension feedback rate and passive relaxation rate are fitted to match the observed timescales. (Bands show the standard deviation from an ensemble of simulations with initial angles drawn from the experimental vertex angle distribution at 0 min.)

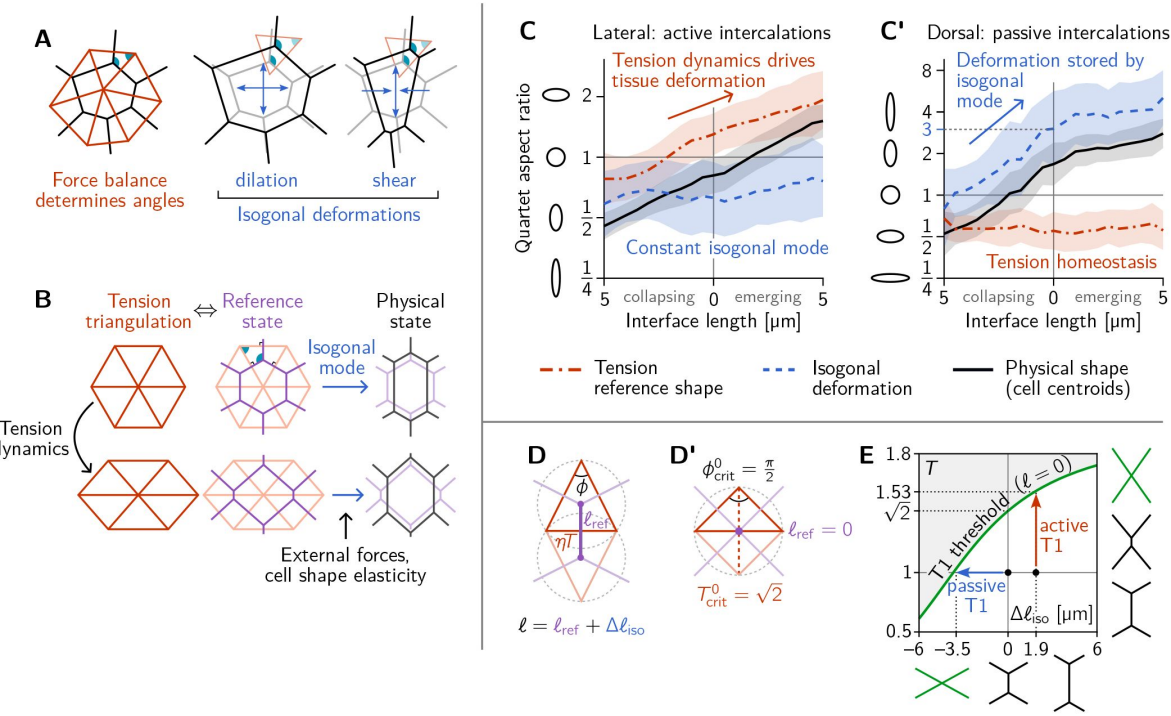


**Figure 4**

**Tension-isogonal decomposition of epithelial geometry identifies active (tension-driven) and passive contributions to tissue deformation.**

**A** The angles in the tension triangulation (red) are complementary to those in the cell array (black) (left). The triangulation acts as a scaffold which leaves freedom for isogonal (angle preserving) deformations which encompass both dilation (center) and shear (right). **B** Deformations of the physical cell array (black, right) can be decomposed into deformations of the tension triangulation (red, left) and isogonal deformations (blue). The former reflect the dynamics of cortical tensions while the latter reflect the effect of external forces and cell shape elasticity. A reference cell array (purple, e.g. a Voronoi tessellation) constructed from the tension triangulation serves as an intermediate relative to which the isogonal deformations are defined. **C and C'** Quartet shape (aspect ratio) and stretch ratio of the isogonal deformation plotted against the length of the quartet's inner interface, which serves as a pseudo-time parametrization of the T1 process. An aspect ratio of 1 indicates an isotropic quartet shape and no isogonal deformation, respectively. Active T1s (left), are driven by a deformation of the tension triangulation while the isogonal mode remains constant. Passive T1s (right), are driven by isogonal deformations while the shape of the tension triangulation remains constant. Bands indicate SD; SEM is smaller than the line width. **D** A symmetric pair of tension triangles is characterized by a single angle  $\phi$ . The cell quartet's central interface in the Voronoi reference configuration (purple) connects the centers of the triangles' circumcircles (dashed gray circles). The general case of asymmetric triangles, characterized by two internal angles, is discussed in the companion paper [32]. **D'** The circumcircles coincide when  $\phi = \phi_{\text{crit}}^0 = \pi/2$ . In this case, the two isosceles tension triangles form a square such that we can read off the critical tension from the diagonal length  $\sqrt{2}$ . **E** T1 threshold for symmetric quartet in the  $T - \Delta l_{\text{iso}}$  plane found by solving Eq. (3) with  $\lambda = 0$  for a symmetric quartet as illustrated in D. The threshold can be reached by isogonal contraction under constant relative tension (blue arrow) or by active contraction under increasing relative tension (red arrow).

area, as well as well as other values of  $n$  do not change the results qualitatively; see Ref. [32]. The timescale of tension dynamics  $\tau_T$  is fitted to the experimental data. Positive feedback drives the relative tension on the quartet's central interface towards the tension threshold discussed above (see **Fig. 3B**) and thus drives active T1s. The interface that collapses is the one that starts with the highest initial tension, which we label with  $i = 0$  by convention such that  $T_0 > T_{1,2}$ .

The tension dynamics described above determines the angles at vertices via adiabatic force balance but leaves the interface lengths  $\ell_i$  as independent degrees of freedom. Further below, we will identify these degrees of freedom as so-called *isogonal* (angle preserving) modes, which are an immediate consequence of having cortical tensions governed by feedback instead of a constitutive relation [31]. To find the lengths  $\ell_i$ , we need to account for subdominant mechanical contributions from internal structures of the cell, such as medial myosin contractility [19, 49] the nucleus [50] and microtubules [51–53]. We account for these contributions through a “cell elastic energy” in terms of the deviation of the cell “shape tensor”  $S_C = \sum_i (\mathbf{e}_i \otimes \mathbf{e}_i) / \ell_i$  from a target shape tensor  $S_0$ :

$$E_C = \lambda [\text{Tr}(S_C - S_0)]^2 + \mu \text{Tr}[(S_C - S_0)^2]. \quad (2)$$

Here,  $\mathbf{e}_i$  are the interface vectors with lengths  $|\mathbf{e}_i| = \ell_i$  (see **Fig. 3A**) and  $\otimes$  denotes the tensor product (We choose this shape tensor because it is linear in interface length, meaning that it does not change if an interface is subdivided by inserting an additional vertex). Importantly, we assume the scale of  $E_C$  to be much smaller than the elastic energy due to cortical tensions. Because of this separation of scales, the angles at vertices are fixed by tensions, and the relaxation of the cell elastic energy only affects isogonal modes.

The coefficients  $\lambda$  and  $\mu$  control the cell's resistance to isotropic compression/dilation and shear deformations, respectively (see SI Sec. 3 for details). Notably, this elastic energy does not engender an “energy barrier” for T1 transitions as is found in vertex models with area–perimeter elasticity [54] (see also **Fig. S10D**). Therefore, our simulations do not require stochastic fluctuations to drive T1s.

The model described thus far captures the dynamics up to the neighbor exchange (time  $< 0$  in **Fig. 3E** and **F**) and qualitatively reproduces the dynamics of interface length and tension observed in the experimental data (cf. **Fig. 2D**). Interface contraction during an active T1 is driven by active remodeling of the force balance geometry: Myosin recruitment increases the cortical tension and thus drives it out of force balance with the external tension from adjacent interfaces. As a result, the interfaces remodel, changing the angles at vertices until force balance is reestablished. Positive tension feedback continually causes further myosin recruitment, which in turn drives further contraction until the interface has fully collapsed.

How does the subsequent resolution and interface elongation work? On the emerging interface, there is typically little myosin [15, 55]. Therefore, active contractility cannot balance the external tension exerted on the interface by its neighbors: The new interface is thrown out of active force balance. This force imbalance naturally leads to the extension of the new edge. As the interface extends, passive tension bearing elements of the cytoskeleton, such as crosslinkers, get loaded until force balance is reestablished. To account for this, we split the total cortical tension  $T$  into the myosin-borne, active tension  $T_{\text{myo}}$  and the passive tension  $T_p$ . Cortical remodeling due to turnover of crosslinkers will gradually relax this passive tension. We account for this by an exponential decay  $T_p \propto e^{-t/\tau_p}$  with a characteristic remodeling rate  $\tau_p$ . This passive tension effectively represents Maxwell-type viscoelasticity of the extending interface, illustrated by the spring and dashpot in **Fig. 3D**. Such visco-elastic behavior on a scale of minutes has been reported in experimental data from the *Drosophila* embryo [46].

Completing the model requires to understand what sets the initial motor protein level on an emerging interface, which will set the initial condition for the tension dynamics on that interface. We propose a myosin “handover” mechanism based on the assumption that the myosin level along the cortex within each cell changes continuously along the interfaces and across vertices [56 [56](#)] (see **Fig. 3D** [57](#)). (Force balance requires that the total tension, the sum of the tensions in the two abutting cortices, is uniform along an interface. However, the individual tensions on either side can be non-uniform, as the resulting traction forces are exchanged via E-cadherin molecules linking the cells along the interface [28 [29](#)].) Importantly, this “handover” model predicts that the myosin level (*not* the total tension) on the newly formed interface is always lower than that on the collapsing interface, in agreement with experimental observations [15 [16](#), 55 [56](#)].

Simulating this model, we find good qualitative agreement between the singlequartet model and experimental data, both for the tension dynamics (compare **Fig. 3E,F** [58](#) and **Fig. 2D,E** [59](#)) and for the tension–isogonal decomposition (compare **Fig. S10A,A'** [60](#) and **Fig. 4C,C'** [61](#)). Movie 3 shows the simulation of an active T1 transition for a symmetric quartet. In the absence of positive tension feedback, the model successfully describes passive intercalations when the displacements of cell centroids are prescribed to mimic external stresses (**Fig. 3F** [62](#); see SI Sec. 3 for details).

Notably, in our model there is no additional active mechanism for interface extension. Instead, interface extension is a consequence of the fundamental temporal asymmetry of T1 processes: high myosin levels on the collapsing interface versus low myosin levels on the emerging interface. No additional active ingredients are required.

Here, we considered a minimal model for an idealized regular lattice geometry here. In a real tissue, there will inevitably be disorder which will impact how cells can coordinate with one another. In the companion paper [32 [33](#)], we investigate the role of such disorder in tissue-scale simulations comprising many cells. For the remainder of this manuscript, we return to the analysis of experimental data, going from the cell scale to the tissue scale.

## A tension–isogonal decomposition quantifies active vs passive contributions to tissue deformation

The above analysis and minimal model have revealed the distinct mechanical forces that drive active and passive cell intercalations. These forces manifested themselves through their effect on the geometry of the cell array. Dominant cortical tensions constrain the angles at vertices. These angle constraints are represented by the tension triangulation. Interface lengths can change collectively while keeping those angles fixed via isogonal modes [31 [32](#)], as illustrated in **Fig. 4A** [63](#). These isogonal modes therefore represent cell and tissue deformations that take place under *constant cortical tensions*. They can be caused, for instance, by external forces and cell-internal elasticity (medial myosin, stiffness of the nucleus, intermediate filaments). It is important to keep in mind that this association of isogonal deformations with nonjunctional stresses is based on the assumption that (active) cortical stresses are the dominant source of stress in the tissue (separation of scales).

These above considerations suggest that we can use the observed geometry of the cell array to decompose cell and tissue deformations into two distinct components: (i) deformations of the tension triangulation reflecting changing cortical tensions, and (ii) isogonal deformations reflecting all other mechanical forces. We will call this a *tension–isogonal decomposition*. This decomposition only assumes the dominance of cortical tensions over other stresses in the tissue and in particular is independent of the specific form of the cell elastic energy **Eq. (2)** [64](#) we used in the minimal model above.

The key elements of the tension–isogonal decomposition are illustrated in **Fig. 4B**. Changes in cortical tension are reflected in deformations of the tension triangulation (i.e. changes of the angles at vertices). To each tension triangulation, we can construct a reference state for the polygonal cell array – compatible with the force balance constraints – from the tension triangulation using a Voronoi tessellation.

Isogonal deformations then transform this reference state into the physical cell array. In practice, we do not need to explicitly construct the reference cell array. Instead, we utilize the fact that the physical cell array can be quantified by the triangulation defined by the cells' centroids [57]. The isogonal modes are calculated as the transformations that deform the tension triangulation into the centroidal triangulation.

We first apply the tension–isogonal decomposition to intercalating quartets. For a given quartet of cells labelled  $i = 1–4$ , we quantify the physical shape in terms of the centroid positions  $\mathbf{c}_i$  by calculating the moment of inertia tensor (see **Fig. 4C**). The tension reference shape is given by the tension vectors  $\hat{\mathbf{T}}_{ij}$ , which are obtained from the interface angles using tension inference and are rotated by 90° relative to the interfaces (see **Fig. 2B**). The ratios of eigenvalues of the moment-of-inertia tensors defines the shape aspect ratios, illustrated by ellipses in **Fig. 4C** and **C'**. The quartet's isogonal deformation tensor  $\mathbf{I}_{\text{quartet}}$  transforms the cell centroids into the tension vertices  $\eta \mathbf{I}_{\text{quartet}} \cdot \hat{\mathbf{T}}_{ij} = \mathbf{c}_i - \mathbf{c}_j$  (see **Fig. S7A** for a labelled sketch). Given  $\hat{\mathbf{T}}_{ij}$  and  $\mathbf{c}_i$  the equations can be (approximately) solved for the best fitting  $\mathbf{I}_{\text{quartet}}$  using least squares (an exact solution is not possible in general because the equations are overdetermined; see SI Sec. 1.5.) The constant global scale factor  $\eta \approx 4.2 \text{ } \mu\text{m}$  translates units from relative tensions (a.u.) to length ( $\mu\text{m}$ ) and can be calculated from the average interface length ( $\mathcal{A}0$ )  $\approx 3.5 \text{ } \mu\text{m}$  at the first timepoint using the Voronoi–Delaunay duality as explained in SI Sec. 1.5.

In **Figs. 4C** and **C'**, we plot the quartet shape aspect ratios and the eigenvalue ratio of the isogonal deformation tensor against the length of the quartet's inner edge. The latter serves as a pseudo-time parameterization of the T1 process; plots against real time are shown in **Figs. S7B** and **B'**. In the lateral ectoderm, the tensiontriangle deformation leads the quartet shape deformation, indicating that tension dynamics drives the intercalation (**Fig. 4C**). This confirms our conclusion from the relative tension analysis (**Fig. 2D**). The isogonal strain is approximately constant and, in fact, slightly counteracts the deformation. This is a consequence of the ventral furrow invagination which pulls on the lateral ectoderm cells and passively stretches them along the DV axis. A very different picture emerges in the passively deforming amnioserosa (**Fig. 4C'**). Here, the tension mode is constant—indicating tension homeostasis—while the cell quartet deformation is entirely stored in the isogonal mode. While the behaviors observed in the lateral ectoderm and in the amnioserosa represent the extreme cases, being purely tension driven (active) in the former and purely isogonal (passive) in the latter, there is continuous spectrum in between. Intermediate scenarios where both cortical tensions and external stresses contribute to tissue deformation are conceivable and can be detected and analyzed using the tension–isogonal decomposition.

Taken together, the tension–isogonal decomposition quantitatively distinguishes between active and passive intercalations. Tensions are controlled locally, while the isogonal modes accommodate external, non-local forces, such as pulling by adjacent tissue. We associate isogonal deformations with passive deformations because active stresses in the lateral ectoderm are generated at interfaces. In systems where active stresses are generated in the cell's interior, e.g. due to nuclear migration [58] or due to intracellular actin cables [59], the isogonal mode is actively controlled. Another example for this is apical constriction during VF invagination which is driven by medial myosin pulses that drive isogonal cell contractions [31].

## Tension space geometry sets the threshold for interface collapse

A puzzle that has remained open so far is the threshold for interface collapse during a cell neighbor exchange. In the lateral ectoderm, where the isogonal strain is approximately constant (**Fig. 4C**), the neighbor exchange takes place at a critical relative tension of  $1.530 \pm 0.005$  on average (cf. **Fig. 2D**). By contrast, in the amnioserosa, where T1s take place under constant tension (**Fig. 2E**), there is an average critical aspect ratio  $\sim 3$  of the isogonal deformation at the point of neighbor exchange (see **Fig. 4C**’).

We now explain these numbers in terms of the geometric tension–isogonal decomposition introduced in the previous section. We start by decomposing the length  $\ell$  of a cell quartet’s central interface into a reference length  $\ell_{\text{ref}}(\{T_i\})$ , determined purely in terms of the local relative tensions, and an isogonal length  $\Delta\ell_{\text{iso}}$  depending on the quartet’s isogonal strain:

$$\ell = \ell_{\text{ref}}(\{T_i\}) + \Delta\ell_{\text{iso}}. \quad (3)$$

A neighbor exchange takes place when  $\ell$  shrinks to zero. Thus, setting  $\ell = 0$  in **Eq. (3)** defines the threshold values of the local tensions  $\{T_i\}$  and the isogonal length  $\Delta\ell_{\text{iso}}$  where T1s take place (see green line in **Fig. 4E**). It is immediately apparent that the interface collapse can be driven by the isogonal mode, by changes in tensions, or by a mixture of both.

Let us start with the passive T1s observed near the dorsal pole. In this case, the relative tensions are homeostatic (cf. **Fig. 2E**), so  $\ell_{\text{ref}} \approx \langle \ell \rangle \approx 3.5 \mu\text{m}$  remains constant. The neighbor exchange therefore happens when  $\Delta\ell_{\text{iso}} = \langle \ell \rangle$  (see blue arrow in **Fig. 4E**). By a geometric construction (**Fig. S7D**) one finds that the corresponding isogonal deformation has an aspect ratio of 3, in good agreement with observations (**Fig. 4C**’).

To find the tension threshold for active T1s, we calculate  $\ell_{\text{ref}}$  using the Voronoi construction based on the vertices of the tension triangulation (see SI Sec. 1.5 for details). The length of a quartet’s central interface in the Voronoi reference state is determined by the pair of tension triangles corresponding to the cell quartet as illustrated in **Fig. 4D**. For simplicity, we consider the case of two identical, isosceles tension triangles which is fully characterized by the relative tension  $T = 2 \sin(\varphi/2)$  on the central interface, with  $\varphi$  the angle in the tension triangle. (The general case of asymmetric tensions is discussed in the companion paper [32], where we show that the T1 threshold is shifted towards stronger tension anisotropy with increasing asymmetry of the tension configurations.) In the symmetric case, the Voronoi construction for the reference length yields  $\ell_{\text{ref}} = \eta T \cot(\varphi)$ . In the absence of isogonal deformations ( $\Delta\ell_{\text{iso}} = 0$ ), the interface length vanishes when  $\varphi = \pi/2$ , implying the critical relative tension  $T_{\text{crit}}^0 = T_{\text{crit}}(\Delta\ell_{\text{iso}} = 0) = \sqrt{2} \approx 1.41$ . One can understand the value  $\sqrt{2}$  for the critical relative tension directly from the circumcircle construction of the Voronoi tessellation as shown in **Fig. 4D**.  $\ell_{\text{ref}}$  vanishes when the two adjacent tension triangles share the same circumcircle. In the case of isosceles triangles, this implies that they form a square such that we can read off the critical relative tension from the length of the diagonal.

In general, the condition  $\ell_{\text{ref}}(T) = -\Delta\ell_{\text{iso}}$  for the neighbor exchange defines the “T1 threshold” in the  $\Delta\ell_{\text{iso}}\text{-}T$  plane (see **Fig. 4E**). This diagram quantifies how active and passive forces interact to drive cell intercalations. Active tension dynamics and passive isogonal strain appear as orthogonal ways to drive T1s, as illustrated by the red and blue arrows.

In the following section, we will generalize the tension–isogonal decomposition to the tissue scale. From this analysis one can then estimate a local average value for  $\Delta\ell_{\text{iso}}$  and then read off the T1 threshold from **Fig. 4E**. This will allow us to explain the value  $T_{\text{crit}} \approx 1.53$ .

## Tissue scale

Our analysis so far has focused on the mechanism of individual T1 transitions in cell quartets. To bridge the gap from cell quartets to tissue-scale convergent–extension flow, we need to address three key questions: (i) How are active T1s oriented? (ii) Which regions of the tissue deform actively due to internally generated local tension and which ones yield passively to stresses created by adjacent regions? (iii) How are active T1s coordinated across cells, so that different interfaces do not “attempt” to execute incompatible T1s? In the following, we will address these three questions by building on the tools (tension inference and tension–isogonal decomposition) we employed above to analyze intercalating cell quartets.

## Initial anisotropy of tension directs flow

Convergent–extension flow of tissue requires that the T1 transitions are oriented. If cortical tensions are regulated by positive feedback, the tissue-scale tension anisotropy sets the orientation the interfaces which will collapse, and hence, the direction of tissue flow. Therefore, tissue-scale anisotropy of active tension is central to drive and orient convergent–extension flow [18, 55, 60, 61].

We assess tension anisotropy by locally averaging the anisotropy of inferred tensions  $T_{ij}$  at a given individual vertices as illustrated in **Fig. 5A** (see SI Sec. 1.4 for details). The inferred tension anisotropy (**Fig. 5B**) and its time course (**Fig. 5C**) are consistent with previously published experimental observations: During VF invagination, DV oriented interfaces in the lateral ectoderm are stretched causing myosin recruitment [26]. Remarkably, we find strong DV alignment of tension anisotropy in the trunk already before VF invagination (**Fig. 5D**, 0 min). This confirms our hypothesis that tension anisotropy is set up in the initial condition. As GBE progresses, the DV alignment of tension anisotropy decreases (**Fig. 5C** and **Fig. 5D**, 37 min). Numerical simulations presented in the companion paper [32] reproduce this loss of global tension anisotropy and show that it is responsible for the slow down of GBE after two-fold extension.

## Isogonal strain identifies regions of passive tissue deformation

We started our investigation by a “tissue tectonics” analysis [16] that identifies the contributions of cell intercalations and cell shape changes to tissue deformations. This kinematic quantification in itself is not informative of the mechanical forces driving epithelial dynamics. To quantify the relative contributions of active (local) vs passive (non-local) forces acting on intercalating cell quartets we introduced the tension–isogonal decomposition (**Fig. 4C**). Just as a tissue tectonics analysis, this decomposition can be performed on the scale of entire tissue regions without the need to track cells and identify T1 events. Specifically, we exploit the fact that the isogonal strain tensor can be calculated for each individual triplet of cells that meet at a vertex (see **Fig. 6A** and SI Sec. 1.5 for details). Locally averaging over nearby vertices then yields the tissue-scale isogonal deformation (see **Fig. 6B** and B'). At the end of VF invagination (25 min), significant isogonal strain has built up adjacent to the VF indicating that the tissue there is passively stretched by the invaginating VF (see purple shaded region in **Fig. 6B**). The lateral ectoderm further dorsal also accumulates some isogonal extension along the DV axis (green shaded region, see time traces in **Fig. 6E**). Specifically, from the DV-DV component of the isogonal strain tensor, we can estimate the average isogonal contribution to the length of DV oriented interfaces  $\langle \Delta L_{iso} \rangle \approx 1.9 \mu\text{m}$  in the lateral ectoderm. Using this value, one can read off the predicted relative tension threshold  $T_{crit} \approx 1.53$  in from the green curve in **Fig. 4C**. This value is in excellent agreement with the value found by tension inference (cf. **Fig. 2D**), thus validating the model for active T1s. An immediate prediction from this model is that abolishing VF invagination will eliminate isogonal stretching of the lateral ectoderm and thereby shift the T1 threshold to  $T_{crit} = \sqrt{2}$ . To test this prediction, we analyzed a light-sheet recording of a *snail* mutant, which lacks the VF as illustrated in **Fig. 7A** [62]. This movie is taken from the *Drosophila* morphodynamic atlas [6]. As expected, we find

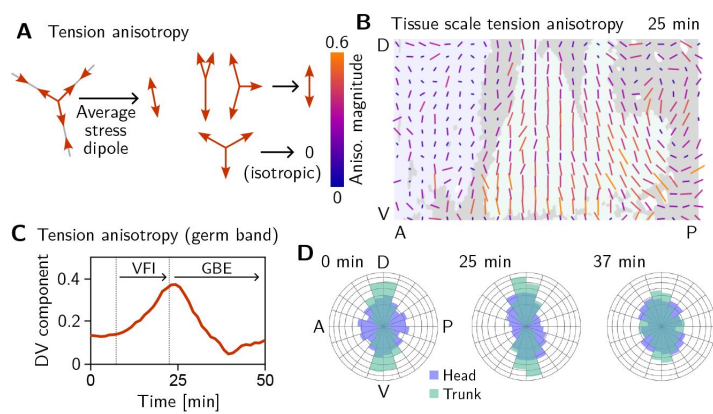


**Figure 5**

**Tissue scale tension anisotropy orients convergent-extension flow.**

**A** Local anisotropy of tension (double-ended arrow) at a single tri-cellular vertex. **B** Tension anisotropy at the end of VF invagination/onset of GBE (25 min) locally averaged on a grid with 20  $\mu\text{m}$  spacing. Line segments indicating the local orientation and magnitude (length and color of the line segments) of tension anisotropy. **C** Mean DV component of locally averaged anisotropic tension in the trunk (green region in **B**). (DV component measured along a fixed axis orthogonal to the long axis of the embryo; SE is smaller than the line width.) **D** Significant DV alignment of the tension orientation in the trunk precedes any tissue flow, while the tension in the head shows no orientation bias (0 min). The DV alignment of tension slightly increases during VF invagination (25 min) and decreases during GBE (37 min).

almost no isogonal strain in the lateral ectoderm of the *snail* mutant (see **Fig. S6**). Analyzing the dynamics of relative tension in intercalating quartets, we find  $T_{\text{crit}} \approx \sqrt{2}$  (see **Fig. 7B**), confirming that tension–isogonal decomposition faithfully captures the interplay of internally generated stresses and external forces during T1 transitions.

During GBE, the isogonal strain near the ventral furrow relaxes back to nearly isotropic, suggesting that the passive deformation stored in the isogonal mode is elastic rather than plastic (**Fig. 6B** and **C**). At the same time, the actively contracting lateral ectoderm stretches the dorsal tissue (amnioserosa) along the DV axis. This passive deformation of the amnioserosa is consistent with the transition of cells from columnar to squamous [7] and low myosin density in the amnioserosa [18]. There is also significant isogonal strain just anterior of the PMG (highlighted by the dashed outline in **Fig. 6B**), as well as on the lateral side of the PMG, suggesting that the hyperbolic (convergent-extension) tissue flow near the dorsal pole [18] exerts a pulling force on the PMG. Quantitative re-analysis of previously published cauterization experiments [19] provides independent evidence of such a pulling force (see SI Sec.4).

Taken together, isogonal strain identifies regions where passive tissue deformation is caused by mechanical coupling across the tissue. Importantly, the absence of isogonal strain along the AP axis in the germ band provides strong evidence that the main driver of GBE is internally generated stress, rather than an external pulling force from the PMG. This conclusion from cell-scale analysis is in line with quantitative tissue-scale analysis of previously published experimental data which we address in the Discussion.

## A geometric order parameter quantifies local tension configurations

Tissue-scale tension anisotropy is not enough to drive coherent “parallel” T1s. Such coordination requires an alternating pattern of high and low tensions as seen in **Fig. 8A** (center; cf. **Fig. 2C**). In contrast, when several connected interfaces are under high tension, they form a tension cable, contraction of which leads to rosette formation [24, 63]. Tension patterns do not appear globally with perfect regularity, but rather as local motifs that can be distinguished based on the tension configuration at individual vertices. These configurations correspond to characteristic triangle shapes in the tension triangulation (see **Fig. 8B**): The elementary motif of the alternating tension pattern is a “tension bridge” where a high tension interface is surrounded by low tension interfaces (see **Fig. 8A**, right), corresponding to an obtuse triangle (**Fig. 8B**, top right). In contrast, an acute tension triangle (**Fig. 8F**, bottom right) corresponds to the local motif of a tension cable, where neighboring interfaces along the cable are under high tension while those transverse to the cable are under low tension (see **Fig. 8A**, left). We can therefore use the tension triangle shape to define a *local tension configuration* (LTC) parameter. The LTC parameter space (i.e. the space of triangle shapes), shown in **Fig. 8B**, is spanned by two axes, measuring how elongated and how acute or obtuse the tension triangle is (see Ref. [32], **Fig. S8** and SI Sec. 1.7 for details). These axes correspond to the magnitude of local tension anisotropy and the cable vs bridge character of the local tension configuration, respectively.

## LTC order choreographs T1s

The geometric condition for neighbor exchanges discussed above (cf. **Fig. 4E**) defines a threshold in the LTC-parameter space (dashed line in **Fig. 8B**, see [32] for details). When the shapes of a pair of adjacent tension triangles cross this threshold, the interface corresponding to the triangles’ shared edge collapses, giving rise to a T1 transition. From the position of the T1 threshold in the LTC-parameter space, it is immediately evident that for tension cables (acute tension triangles), the tension anisotropy required to cross the T1 threshold is higher compared to tension bridges. Tension cables are therefore less efficient at driving T1s: they require stronger anisotropy of tension to cause an interface collapse.

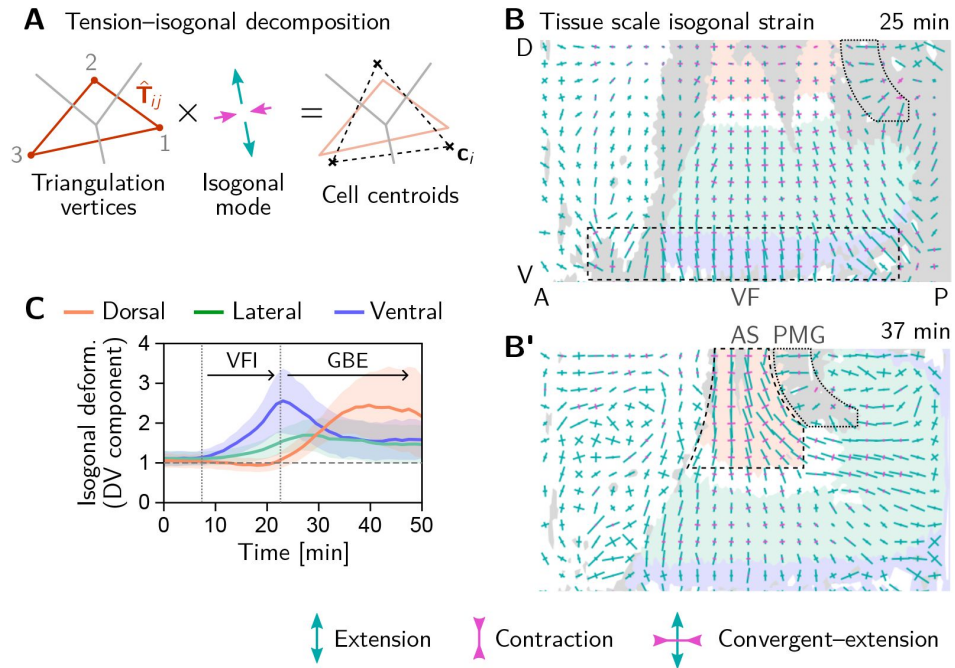


**Figure 6**

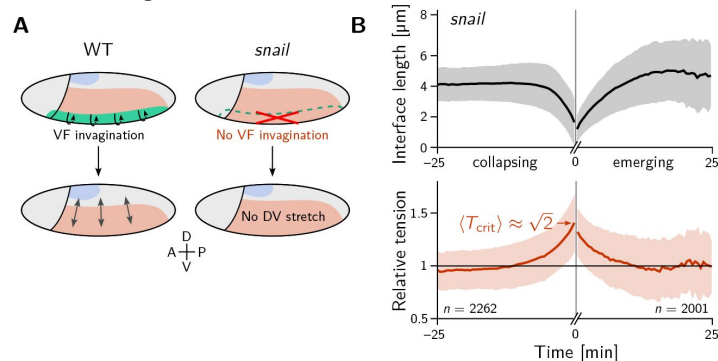
**Tissue scale quantification of isogonal strain identifies regions of passive tissue deformation.**

**A** Tension-isogonal decomposition at a single tri-cellular vertex. The isogonal strain tensor (illustrated by blue arrows) transforms the tension triangle (solid red lines) into the centroidal triangle (dashed black lines). **B and B'** Isogonal strain at the end of VF invagination (25 min, B) and during GBE (37 min, B') averaged over vertices in a grid with 20  $\mu\text{m}$  spacing. High isogonal strain in the tissue adjacent to the VF at 25 min (dashed black rectangle) and in the amnioserosa (AS, dashed black outline) at 37 min indicate passive tissue deformations in these regions. High isogonal strain is also found at the front of the invaginating posterior midgut (PMG, dotted outline). Crosses indicate the principal axes of isogonal strain. Bar lengths indicate the magnitude of strain (green: extensile, magenta: contractile). Colored tissue regions are quantified in (C). **C** Time traces of the DV component of isogonal strain. The isogonal (i.e. passive) stretching of the tissue adjacent to the VF (purple) is transient. The lateral ectoderm as a whole (green and blue) is stretched weakly, but persistently. The amnioserosa (red) is strongly stretched as the lateral ectoderm contracts along the DV axis during GBE. (DV component is defined with respect to the local co-rotating frame, see SI; Shaded bands show one SD; SEM is comparable to the line width.)

**Figure 7**

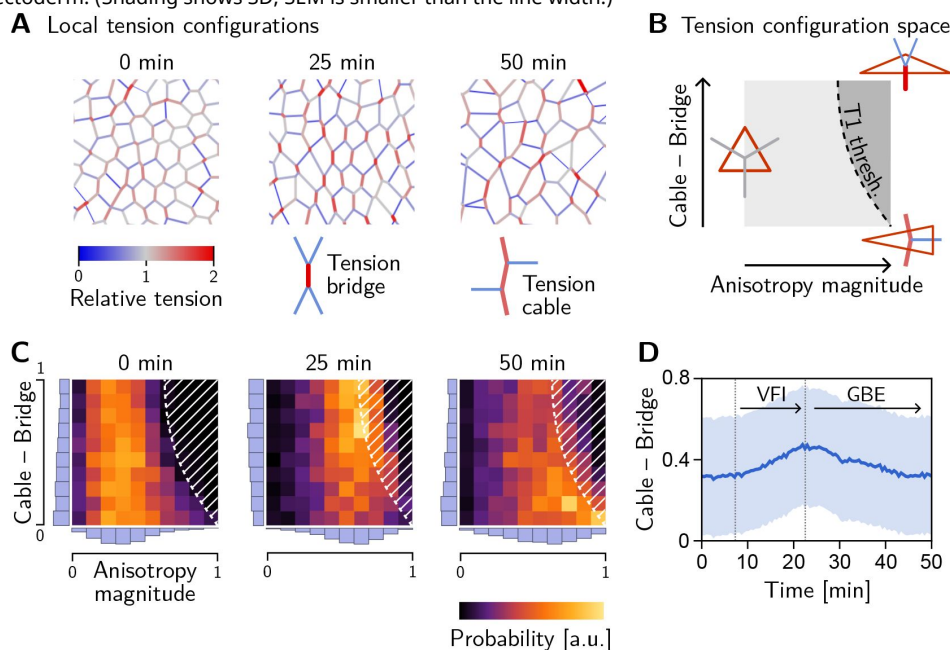
**The relative tension threshold for T1s is shifted in a *snail* mutant.**

**A** In a WT embryo (left), the invaginating ventral furrow (green) stretches the lateral ectoderm (red) along the DV axis prior to GBE. In a *snail* mutant (right), the ventral furrow is abolished, such that no DV-stretch of the lateral ectoderm occurs. **B** In a *snail* mutant, the T1 threshold of active T1s in the lateral ectoderm is shifted to the value  $\sqrt{2}$  predicted by our model in the absence of isogonal deformation (cf. Fig. 4E).



**Figure 8**

Emergence and loss of order in local tension configurations. **A** Distinct configurations of tension are found on the cell scale: “Tension bridges”, characterized by a high-tension interface connected to four low-tension interfaces, are the local motif of an alternating pattern of high and low tensions. This alternating pattern gives rise to coordinated T1s as the high-tension interfaces collapse, driven by positive tension feedback. By contrast, tension cables, characterized by multiple adjacent high-tension interfaces, cause frustrated or incoherent T1s which manifest as rosettes. **B** Space of local tension configurations at a single vertex (quantified by the tension triangle shape, see Ref. [32] and SI Sec. 1.7 for details). The dashed line indicates the “T1 threshold” calculated for the average isogonal strain in the germ band (cf. Fig. 4G). This threshold is at lower anisotropy magnitude for tension bridges than for tension cables, indicating that the former are more efficient at driving active intercalations. **C** Distribution of tension configurations defines an order parameter that quantifies the relative abundance of tension cables and bridges in the lateral ectoderm. Arrows highlight the increasing fraction of tension bridges before GBE (0–25 min) and its decrease during GBE (25–50 min). **D** Median of the obtuse-acute triangle shape parameter in the lateral ectoderm. (Shading shows SD; SEM is smaller than the line width.)



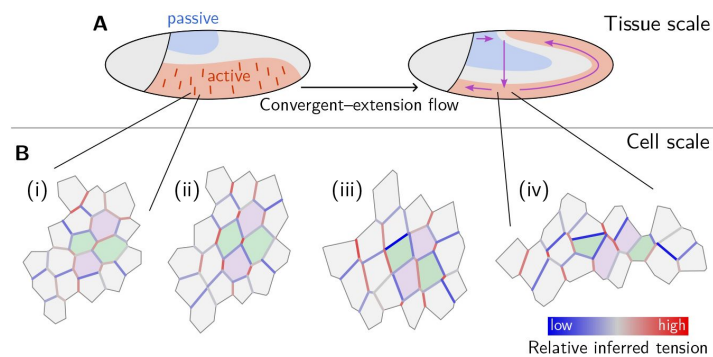


**Figure 9**

Mechanical coordination of convergent-extension flow on the tissue and cell scale. **A** Dorso-ventral patterning of mechanical properties and tension anisotropy (red lines) organize and orient tissue flow. **B** A cell scale pattern of tensions coordinates active cell intercalations that drive convergent extension of the lateral ectoderm. From relatively uniform but weakly anisotropic initial tensions (i), an alternating pattern of high and low tensions emerges (ii). Subsequently, high-tension interfaces fully contract thereby driving parallel active T1 transitions (iii). As T1s proceed, order in the tension configurations is lost and convergent-extension flow cedes (iv).

Two-dimensional histograms of the LTC-parameter distribution in the lateral ectoderm show that the fraction tension of bridges increases before the onset of GBE (see [Fig. 8C](#)). The bridge fraction reaches its maximum around 25 min, just at the onset of GBE (see [Fig. 8D](#)). The corresponding alternating pattern of tensions is clearly visible in [Fig. 8A](#) (center). This suggests that the pattern of tensions on the (sub-)cellular scale is biologically relevant to choreograph parallel T1s. As the tension anisotropy increases (cf. [Fig. 5C](#)), the local tension configurations eventually hit the T1 threshold where a cell neighbor exchange happens, causing a reconfiguration of local tensions. Therefore, tension configurations beyond the T1 threshold are strongly suppressed (hatched region in [Fig. 8C](#)). We observe that as cell intercalations take place in the lateral ectoderm, the fraction of tension bridges decreases and the fraction of tension cables increases (see [Fig. 8G](#), 50 min; and [Fig. 8H](#)). In fact, the distribution of tension triangle shapes appears to approach that of a random Delaunay triangulation (see SI [Fig. S9](#)), a completely disordered distribution. This suggests that the triangle edge flips can be statistically understood as a random “mixing” process that generically causes a loss of LTC order and global alignment of tension anisotropy. This result, as well as the results of the tissue-scale analysis more generally, can be reproduced by tissue-scale simulations of our minimal model, as shown in the companion paper Ref. [\[32\]](#).

## Discussion

### Cortical tensions drive and constrain tissue deformations on the cellular scale

We have developed a novel perspective on tissue dynamics based on the underlying principle of force balance. Central to our approach is the balanced network of active forces generated and transmitted by cells. In epithelia where contractility in the adherens-junctional cortex is the strongest source of stress, the force network takes the form of a triangulation in tension space [\[31\]](#) which fixes the angles at tri-cellular vertices in the tissue. Tissue deformations are driven by the adiabatic transformation of this force-balance geometry, allowing the epithelium to rearrange like a fluid, while supporting internal tension like a solid. Alternatively, one can think of this behavior as a form of plasticity where the internal “reference” structure of the material can be actively remodelled, resulting in spatial displacement of material points. However, the focus on the force balance geometry associated with the internal structure is more useful as it holds the key to understanding possible mechanisms of active control. We find two mechanically distinct modes of tissue deformation: a cortical-tension driven mode and an isogonal (angle preserving) mode that is unconstrained by the cortical force-balance geometry. The former represents active remodeling of interfaces, e.g. by myosin recruitment, while the latter accounts for passive tissue deformations that are controlled by external (non-local) forces and cell shape elasticity. The *tension-isogonal decomposition* quantifies the contributions of these two modes in experimental data based on cell geometry alone. This allows us to disentangle whether deformations are due to locally or non-locally generated forces, i.e. whether they are active or passive. Importantly, tension-isogonal decomposition is based on the same assumptions as tension inference which has been validated extensively in previous literature [\[29, 30, 38, 39\]](#).

In the early *Drosophila* embryo, we observe both active and passive cell rearrangements (T1 events). Generally, both modes—tension-driven and isogonal—interact and contribute to tissue deformations at the same time. We have found that ventral furrow invagination isogonally stretches the lateral ectoderm which increases the tension threshold for active T1s there. This predicts that the local relative tension threshold will be lower (namely  $\sqrt{2}$ ) in mutants which lack a ventral furrow (*twist* and *snail* [\[62\]](#)). Indeed, analysis of a *snail* mutant embryo confirmed this prediction and thus validates that tension-isogonal decomposition captures the interplay of internal and external forces acting on a tissue.

## Internal and external contributions to germ band extension

Where the forces driving tissue deformations during morphogenesis originate is a fundamental question of developmental biology. In the context of *Drosophila* gastrulation, the question is whether the germ band elongates due to internally generated stresses [13, 15, 18, 20, 26, 55] or due to external pulling by the posterior midgut invagination [19–21, 22, 64] has been intensively debated. Experimental evidence shows that both processes contribute, making a nuanced, quantitative analysis necessary. We therefore re-analyzed microscopy data from previously published cauterization and mutant experiments [19] to quantify tissue flow (see SI Sec. 4). The results from this quantitative analysis indicate that forces generated in the germ band contribute significantly to tissue flow. This conclusion is further supported by the observations from mutants where posterior midgut invagination is disrupted (*fog*, *torso-like*, *scab*, *corkscrew*, *ksr*). In these mutants, the germ band buckles forming ectopic folds [65, 66] or twists into a corkscrew shape [67, 68] as it extends, pointing towards a buckling instability characteristic of internally driven extensile flows [69, 70]. This suggests that the main effect of PMG invagination on the germ band lies not in creating pulling forces, but rather in “making room” to allow for its orderly extension.

However, these tissue-scale observations only provide circumstantial evidence for internally driven GBE. To conclusively settle the debate, evidence from the cell scale – where the forces are generated – is needed. Such evidence is provided by our tension–isogonal analysis, which yields a fine grained picture with various regions of active and passive deformation (see **Figs. 6B** and **B**). It clearly shows that tissue deformation in the germ band is driven by internal remodeling of tensions and therefore active. In stark contrast, the amnioserosa, and the tissue just anterior and lateral of the invaginating posterior midgut deforms passively.

## Cells orchestrate tissue flow by self-organizing in tension space

The internally driven nature of germ-band elongation flow immediately raises the question of how force generation is coordinated across cells in order to drive coherent tissue flow. In other words, how can local behavior of cells orchestrate global tissue flow? Cells exert active stresses on each other and, at the same time, constantly sense their mechanical environment [71–73].

Mechanical stresses and strains can propagate over long distances and contain information about the tissue geometry (e.g. in the form of hoop stresses [74]). In an epithelium dominated by cortical tensions, this mechanical environment forms a “tension space”, linked to physical space via force balance. Tension space takes the form of a triangulation which allows an intuitive visualization. The angles in the cell array are fixed by complementary angles in the tension triangulation. Thus, the tensions are geometric dials cells can directly sense and control.

We found that cells can control their configuration in tension space by defining local dynamics of cortical tension. In experimental data from gastrulating *Drosophila* embryos, we identified two distinct behaviors: (i) amplification of tension on the interfaces that are already most tense, suggestive of positive tension feedback (observed in lateral ectoderm) and (ii) apparent tension homeostasis (observed in the amnioserosa). Mechanical homeostasis is found in various systems and organisms [75–77]. We hypothesize that tension homeostasis allows the amnioserosa to undergo large cell deformations while maintaining tissue integrity [76, 78]. Tension feedback, on the other hand, continuously modifies local force balance, driving the change in cell and tissue geometry. To the extent that cortical responses can be controlled by spatially modulated gene expression, evolution thus has the means to define a program of non-trivial spatio-temporal dynamics of tissue during morphogenesis. Evidence for positive feedback is provided by the nonlinearly increasing inferred tension on contracting interfaces (**Fig. 2D**) and by laser ablation experiments in earlier work [24]. The underlying molecular mechanisms are yet to be identified and might rely on the catch-bond behavior of myosin [79, 80] or mechano-sensitive binding of  $\alpha$ -catenin [81, 82].

We have found that T1 events can be explained quantitatively by a simple geometric criterion which defines a “T1 threshold” in terms of the local tension configuration and the local isogonal strain. A minimal mathematical model of an intercalating cell quartet demonstrates how positive tension feedback can drive the tensions towards this T1 threshold and thus generate active T1s. In contrast, passive T1s result from external forces changing the isogonal modes until a cell neighbor exchange occurs, while tensions (and thus interface angles) remain constant.

Our mathematical model for an intercalating cell quartet also sheds light on the long-standing puzzle of how interfaces extend after a neighbor exchange, even though cortical myosin can only exert contractile forces. We show that no additional active mechanism is necessary. Our minimal model captures interface extension as a purely passive process. In our model, interface extension during both active and passive intercalations is driven by the tension on adjacent interfaces which exceeds the low active contractility of the new edge. The low myosin level on the emerging interface is predicted by a simple model for the myosin “handover” during a neighbor exchange. In tissue-scale simulations [32 [2](#)], the model reproduces experimental observations (interface extension even if tissue extension is blocked, generation of irregular cell shapes) that were previously taken as evidence for actively driven interface extension [19 [2](#), 83 [2](#)].

Our findings on the dynamics of interface length and tension during active T1s (Fig. 2D [2](#)) are similar to another recently proposed model [45 [2](#)]. This model extends the classical “vertex model” with perimeter-area elasticity by active cortical contractility. Like in our model, active T1s are driven by a positive feedback loop of cortical tension. Since our model is formulated in adiabatic force balance, it requires fewer parameters than the one of Ref. [45 [2](#)] and might be obtained from the latter in the limit of fast mechanical relaxation and dominant active tensions.

Other recent theoretical work has interpreted *Drosophila* germ band extension as a result of tissue fluidization [84 [2](#)], i.e. the loss of resistance to shear stress due to vanishing of cortical tensions [47 [2](#), 85 [2](#)]. However, laser ablation experiments [19 [2](#), 27 [2](#)] show that cortical tensions remain finite during the morphogenetic process. In fact, interfaces under vanishing would generically buckle into a wiggly shape (as observed, for instance, in the amnioserosa during dorsal closure [86 [2](#)]). This is not observed in the *Drosophila* ectoderm during gastrulation where interfaces instead appear straight, serving as a simple visual indicator of finite tension. We have therefore investigated tissue mechanics in the regime where the tissue internally generated tension at all times, and hence is a solid rather than a fluid. Tissue flow occurs as a result of internally driven *plastic rearrangements*, and does not require or imply tissue fluidization. The capacity of an epithelial tissue to internally rearrange in a controlled manner which may be thought of as *active plasticity* falls beyond the fluidization paradigm. The results of our analyses on the cell and tissue scale corroborate this point of view. We return to the question of fluid vs solid behavior in the companion paper [32 [2](#)].

## Order in local tension configurations coordinates active T1s

We found a striking alternating pattern of cortical tensions that explains how T1s are coordinated between neighboring cells. The prevalence of this organizing motif is quantified by an order parameter for local tension configurations (LTC). LTC order precedes intercalations in lateral ectoderm and the loss of LTC order correlates with the slowdown of tissue flow at the end of GBE. This raises two important questions: First, how does LTC order emerge? Second, is loss of LTC order the cause for the termination GBE? These questions are addressed in a companion paper [32 [2](#)] using a tissue-scale mathematical model based on the quartet-scale model introduced here. We show that LTC order is driven by positive tension feedback and requires an initial regular hexagonal packing of cells. Intercalations disrupt this regular hexagonal packing and thus lead to the loss of LTC order as GBE progresses. Together with a degradation of coherent tension orientation, loss of LTC order causes T1s to become incoherent and therefore ineffective at driving tissue flow. Taken together, this implies that convergent-extension flow is selflimiting and that the

final tissue shape is encoded in the initial degree hexagonal order and tension anisotropy. Moreover, we predict that disrupting the hexagonal packing of nuclei prior to cellularization will prevent the emergence of LTC order and thus cause slower GBE.

## Genetic patterning and initial anisotropy

Because *Drosophila* embryo is a closed surface, convergent extension of the germ band must be compensated by an orthogonal deformation of the dorsal tissue, the amnioserosa (see **Fig. 6B**). To achieve that, mechanical properties of the tissue must be modulated along the dorso-ventral axis: Positive tension feedback driving active rearrangements in the lateral ectoderm, and tension homeostasis in the amnioserosa allowing it to yield to external forces while maintaining tissue integrity. This highlights the importance of the DV-axis patterning. Recent work [26] has shown that mechanical feedback loops in the embryo are patterned along the DV axis. Notably, the DV patterning system is conserved across species [87]. Our work also highlights a second interaction between tissue flow and DV patterning: because the coherent T1s we observe do not mix cells in the tissue (**Fig. 1A**), distinct DV fates (e.g. neural and surface ectoderm) remain clearly demarcated, a clear biological necessity.

In addition to the DV gradient, tension anisotropy along the DV axis is required to orient the GBE flow along the AP axis. This anisotropy might be due to mechanics (pulling of the ventral furrow [26] and hoop stresses resulting from ellipsoidal embryo geometry [74], since we observe anisotropy already prior to VF formation), or indeed due to AP-striped genetic patterning [88, 89]. Thanks to the positive tension feedback, a weak initial anisotropy is sufficient to bias the direction of tissue elongation. This explains why *twist* and *snail* mutants, which have significantly reduced initial myosin anisotropy, still extend their germ band, albeit at a slower rate [26].

Our findings show how genetic patterning and self-organization are interconnected during GBE. Genetic patterning provides tissue scale input by demarcating distinct tissue regions with different mechanical properties. Self-organization via positive tension feedback orchestrates myosin contractility on the cellular scale and drives T1s. In the companion paper [32], we show that mechanical self-organization via tension feedback also allows cells to coordinate their behaviors (such as active T1s) on the tissue scale to give rise to coherent morphogenetic flow. As of yet, no genetic mechanism has been found that produces cell scale coordination – as manifested, for instance, in the alternating pattern of high and low tensions (**Fig. 8A**, center) – from predetermined genetic patterns alone. Moreover, many interfaces in the lateral ectoderm that undergo T1 transitions at late stages of GBE are initially oriented along the AP, rather than the DV axis and only rotate into DV alignment briefly before they collapse (see **SI Fig. S2**). This shows that an initially set up genetic pattern is not sufficient to explain the coordination of cell rearrangements, in line with evidence from tissue scale analysis [74]. Instead, the emerging overarching picture is that of morphogenesis driven by an interplay of bottom-up local self-organization controlled by top-down genetic patterning that sets initial conditions and modulates parameters on the tissue scale [90, 91]. Indeed, this interplay has recently been shown to underlie posterior midgut invagination, where genetic patterning initiates and channels a wave that mechanically propagates due to a local feedback mechanism acting on myosin [64].

Going forward, we expect that geometric insight into tension space will provide a new perspective on many different systems [92], for example *Xenopus* neural tube formation [93], amniote primitive streak formation [94–96], wing disk elongation [97, 98], the sea urchin archenteron [99], or kidney tubule elongation [100]. Further, it will be interesting to study intercalations driven by actin “protrusions” [101]: they too are governed by cortical force balance on the cellular level, making tension inference and the tension-isogonal decomposition applicable.

## Acknowledgements

We thank Noah Mitchell, Sebastian Streichan, and Arthur Hernandez for stimulating discussions and careful reading of the manuscript. We would also like to thank the anonymous reviewers for excellent feedback on the manuscript. FB acknowledges support of the GBMF post-doctoral fellowship (under grant #2919). NHC was supported by NIGMS R35-GM138203 and NSF PHY:1707973. MFL was support by NSF Career grant No. PHY-2047140. EFW acknowledges support from Howard Hughes Medical Institute. BIS acknowledges support via NSF PHY:1707973 and NSF PHY:2210612.

## Supplementary Material

### 1 Analysis of experimental data

#### 1.1 Data source

Whole embryo cell segmentation and tracking data for a WT embryo was obtained from the repository DOI:10.6084/m9.figshare.18551420.v3 deposited with Ref. [7 [2](#)]. We analyzed the dataset with id number 1620 since it had the highest time resolution (15 s) and covered the longest time period (50 min), starting ca. 7 min before the onset of ventral furrow invagination.

For the analysis of the *snail* mutant, we used data from the *Drosophila* morphodynamic atlas [6 [2](#)]. This data is available on the data repository Ref. [102 [2](#)]. We used recording No. 202207111700 of a *halo snail*[IIG05]; *CAAX-mCherry* fly. For cell segmentation and tracking, we used the Fiji plugin *TissueAnalyzer* [103 [2](#)] and custom Mathematica code. For analysis of T1 transitions and isogonal strain, we excluded regions that form folds. Note that in recording No. 202207111700 the one dorsal fold ectopically extends all the way to the ventral side.

#### 1.2 Tissue tectonics analysis

Based on segmented and tracked cells, the tissue strain rate and cell deformation rate can be calculated via the methods described in Ref. [16 [2](#)]; see also [104 [2](#)] and [57 [2](#)]. In brief, the local tissue strain rate is calculated from the centroid positions  $\mathbf{c}_i$  of the cells in a small neighborhood  $N$  of a cell (we use nearest neighbors). One looks for a linear transformation that maps the positions of the cell centroids at one timepoint to those at the next one. Because the resulting equations are overdetermined, an approximate solution minimizing the error is obtained using the least-squares algorithm. The linear transformation is then further decomposed into a symmetric part, describing local shear and area changes, and an antisymmetric part, describing the tissue rotation. Because the *Drosophila* ectoderm is a surface in three dimensional space, we need to calculate these quantities in the local tangent plane. The cell deformation rate is calculated from the rate of change of the cell's moment of inertia tensor in the frame that co-rotates with the tissue.

**Figure S1A** [2](#)–**B** [2](#)’ show the tissue and cell deformation rates during VF invagination (A and A’) and during GBE (B and B’). **Figure S1C** [2](#) shows the cell elongation as measured by the Beltrami coefficient  $\mu = |a - b| / (a + b)$ , where  $a$  and  $b$  are the half-axes of a best-fit ellipse to the cell.

### Local tangent plane and coordinate frames

The analysis of local tissue geometry (including tissue tectonics, tension inference, and tension-isogonal decomposition) is performed in the local tangent plane. The local tangent plane is determined by the local normal vector  $\mathbf{n}$  which we find by a singular value decomposition of the point set of interest (vertex coordinates for a single cell, cell centroids for a patch of cells). The normal vector is read-off as the basis vector corresponding to the smallest singular value.

Depending on the context, we use three different coordinate bases within the tangent plane: (i) The “Eulerian” (or “lab frame”) basis formed by the azimuthal vector  $\mathbf{e}_{DV}^E$  along the DV axis and its orthogonal complement  $\mathbf{e}_{AP}^E = \mathbf{n} \times \mathbf{e}_{DV}^E$ , along the AP axis. The Eulerian frame is used to plot orientation and strain fields in the flat map projections (“pullbacks”) of the tissue (e.g. [Fig. 4D](#) and [Fig. 8B](#)). (ii) A “Lagrangian” (or “tissue frame”) basis which co-rotates with the tissue is used to quantify the DV component of the isogonal deformation tensor ([Fig. 4E](#)). This co-rotating frame is defined by tracking a patch of cells and fitting a linear transformation  $A(t)$  to the displacement of cell centroids relative to the patch’s center of mass. The linear transformation is constrained to transform the initial into the final normal vector  $A.\mathbf{n}(0) = \mathbf{n}(t)$ . A polar decomposition  $A(t) = S(t).R(t)$  then yields the local rotation matrix  $R(t)$  for the tissue patch. The co-rotated basis vectors are obtained by applying  $R$  to the Eulerian basis vectors at time zero:  $\mathbf{e}_i^L(t) = R(t).\mathbf{e}_i^E(0)$ . (iii) For the tension-isogonal decomposition of intercalating cell quartets ([Fig. 4C](#) and [C'](#) and [Fig. S7](#)), we define a co-moving orthogonal basis based on the cell centroids: The basis vectors are defined as the pair of orthogonal vectors that best fit the displacement vectors that connect opposite cells in the quartet. Before the neighbor exchange, the first basis vector is aligned with the two cells that touch and the second basis vector is aligned with the cells that don’t touch. After the neighbor exchange, the roles are flipped. This ensures that the basis vectors vary smoothly through the neighbor exchange.

### 1.3 Identification and classification of intercalation events

Cell interface collapse and emergence events can be identified by tracking cell contacts. We start by identifying all pairs of cells that share a interface at some timepoint. For each pair, one can then identify the time periods where the cells are in contact. This allows one to identify interface collapse and emergence events. We exclude cases where a cell pair loses contact because one of the cells invaginates or divides and cases where cells come into contact because cells in between them invaginate.

Some cell pairs transiently lose or gain contact. For the interface collapse rate shown in [Fig. 1E](#), we only account for the first collapse event for cell pairs that are not in contact at the last frame, i.e. for those that *permanently* lose contact. Similarly, for interface emergence events, we only account for the last event where a pair of cells not in contact at the first frame comes into contact.

### Spatial distribution of interface collapses

From the tracked interface collapses, we can count the number of interface collapses that each cell is involved in, giving us a spatially resolved map of intercalations ([Fig. S1D](#)). In the lateral ectoderm (regions 4–8 in [Fig. S3A](#)), we find 2.58 interface collapses per cell. From this, we can estimate the total tissue extension by cell rearrangements. In a hexagonal lattice, synchronous T1s cause two interface collapses per cell and elongate the tissue by a factor  $\sqrt{3}$ , assuming that the cells do not elongate. (The tissue also contracts by a factor  $1/\sqrt{3}$  along the orthogonal axis.) For 2.58 interface collapses per cell, therefore cause tissue elongation by a factor  $(2.58/2) \times \sqrt{3} \approx 2.23$ , in good agreement with the total elongation of the germ band (cf. [Fig. 1D](#)).

In contrast to the lateral ectoderm where cells don't elongate coherently, cell elongation contributes significantly to tissue deformation near the dorsal pole (see [Fig. S1C](#)). This is a generic feature of passive T1s driven by isogonal deformations (see [Fig. S7D](#)).

### Orientation of collapsing interfaces

The convergent-extension flows in the lateral ectoderm and near the dorsal pole (amnioserosa) are oriented perpendicular to each other (see [Fig. S1](#)). We therefore also expect perpendicular orientation of the collapsing interfaces in these two regions. We quantify interface orientation of collapsing edges at the blastoderm stage (i.e. before the onset of tissue flow,  $t = 0$  min) as shown in [Fig. S2A](#) and [C](#). In the ectoderm, interfaces that collapse before  $t = 42$  min, i.e. within the first ca. 15 min of GBE are predominantly DV oriented at  $t = 0$  min (see [Fig. S2B](#)). By contrast, interfaces near the dorsal pole predominantly oriented along AP. The orientation of interfaces in the lateral ectoderm that collapse after  $t = 42$  min is initially not strongly biased along the DV axis [Fig. S2C](#) and [D](#). However, during GBE, these interfaces progressively align with the DV co-rotated DV axis before they eventually start contracting (see [Fig. S2C'](#) and [D](#); the coordinate frame co-rotating with the tissue is described in Sec. 1.2).

### Tracking quartets and identifying rosettes

The above procedure for identifying intercalation events is very fast and easy to implement. However, it does not distinguish between T1s and higher order intercalation events (rosettes). Moreover, it cannot easily be determined which interface collapse corresponds to which interface emergence.

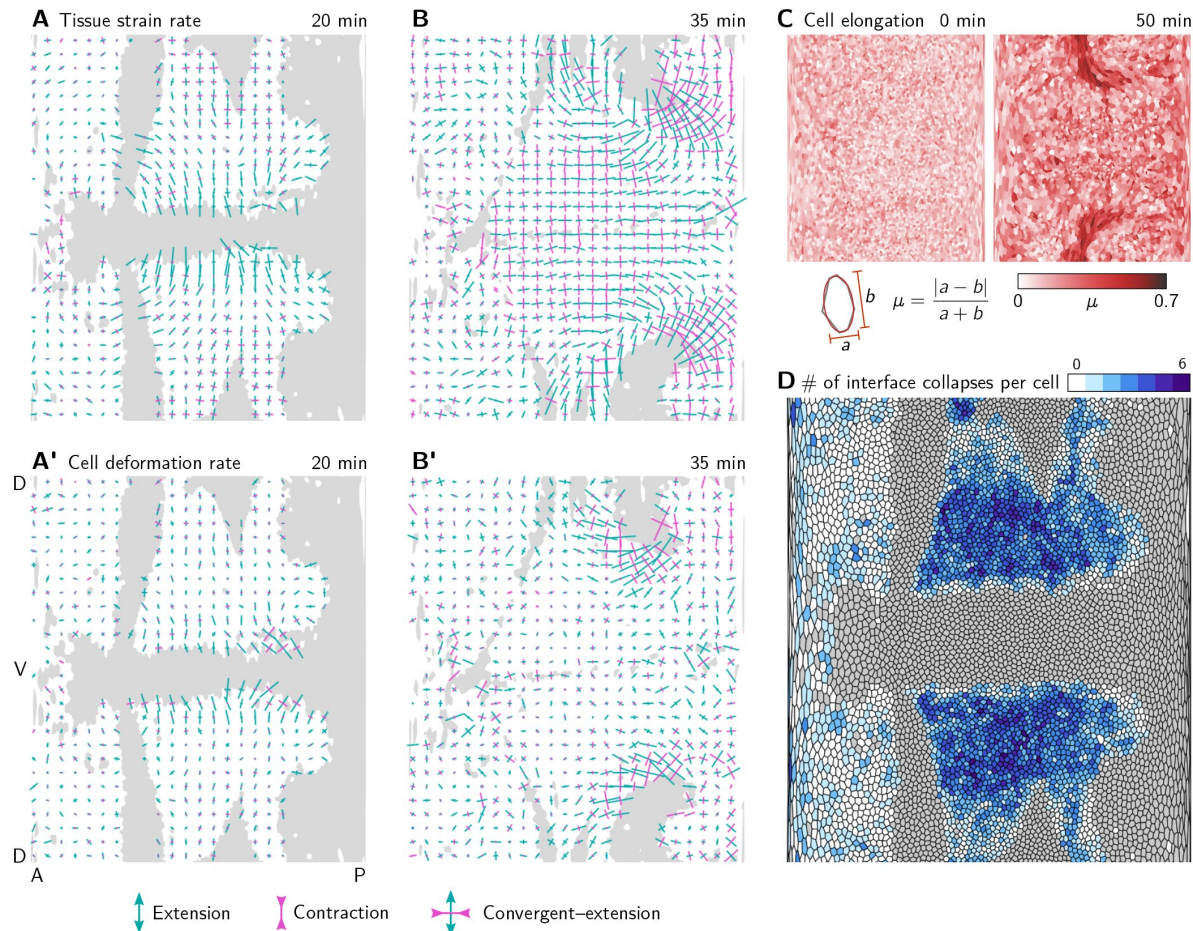


**Figure S1**

Tissue tectonics analysis. **A and A'** During VF invagination, the tissue strain rate (A) and cell deformation rate (A') are high in the lateral ectoderm adjacent to the ventral furrow, where cells get stretched along the DV axis. Crosses show the principal axis of strain averaged in a grid with 20  $\mu\text{m}$  spacing. Bar length is proportional to the strain rate and color indicates extension (green) and convergence (magenta). **B and B'** During GBE, the tissue strain rate (B) is high in the lateral ectoderm which undergoes convergent extension. The cell deformation rate (B') there is low, and incoherent implying that the tissue deforms via cell rearrangements. In contrast, near the dorsal pole, both cell deformation and cell rearrangements contribute to tissue strain rate. **C** Cell elongation measured by the Beltrami coefficient  $\mu$  from the best-fit ellipse. Cells near the dorsal pole become highly elongated. **D** Total number of interface collapses per cell. Note that in Ref. [7] (the source of the segmentation data), the number of intercalations per cell is instead calculated as the sum of collapsed interfaces and new interfaces per cell, leading to numbers higher by a factor of 2. (Invaginating cells are shown in gray. Strain rates are only shown for cells that do not invaginate.)

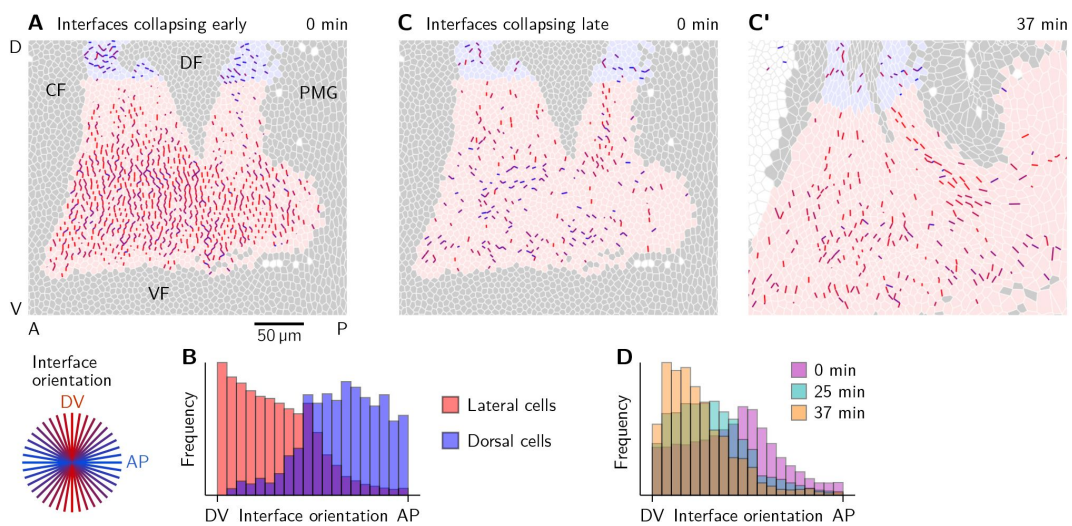


**Figure S2**

Orientation of collapsing interfaces. **A** and **B** interfaces collapsing early (before 42 min) colored by their orientation at time 0 min (A) and histograms showing the interface orientation (B). Collapsing interfaces near the dorsal pole (shaded blue) are predominantly oriented along the AP axis. In the lateral ectoderm, the orientation is predominantly along the DV axis. **C**–**D** Interfaces collapsing late (after 42 min) have low initial orientational bias (C) but progressively align with the co-rotated DV axis before they start contracting (C').

We therefore implemented an alternative algorithm to identify intercalations, by tracking quartets of cells. This is possible by identifying cycles of length four in the neighborhood graph of the cell array at each time point. We exclude cases where the four cells surround one or more cells that are not part of the cycle and cases where one of the cells is surrounded by the three others.

Notably, the quartets don't necessarily exist for the entire time series. Namely, when one of the “inner” interfaces in the quartet, other than the central interface, collapses, the quartet is destroyed.

A T1 event happens when the opposite pairs of cells in the quartet exchange neighbors (i.e. one pair loses contact and the other one gains it). In some cases, the neighbor exchange is not instantaneous, but instead there is a fourfold vertex in the center of the quartet for an extended period. Cases where the central interface and one of its neighbors are simultaneously shorter than a threshold length (0.5  $\mu\text{m}$ ) are classified as rosettes and not counted as T1s. The threshold value 0.5  $\mu\text{m}$  corresponds to the average vertex-positions fluctuations on the timescale of 1 min. Higher order rosettes can be “decomposed” into overlapping 5-fold rosettes and therefore can be identified by finding such overlaps.

Using this procedure, we identified 2231 T1 events, 498 five-fold rosettes, 40 six-fold rosettes, 4 seven-fold rosettes and no higher order rosettes (see Fig. 1E<sup>15</sup>). Because the number of rosettes is small compared to the number of T1s, we have focused on T1 events for the subsequent analysis. Expressed in terms of a participation ratio of interface contractions in T1s vs rosettes, we find a ratio 2231 : (2 · 498 + 3 · 40 + 4 · 4)  $\approx$  2 : 1, matching observations from previous studies [7<sup>16</sup>, 17<sup>17</sup>].

#### 1.4 Local tension inference

Consider the triplet of cells that meet at a tri-cellular vertex and label them  $i = 1, 2, 3$ . Denote the unit vectors pointing along the three interfaces that meet at the vertex by  $\mathbf{e}_{ij}$ , where  $i, j$  are the labels of the pair of cells that share the respective interface. Force balance implies that

$$T_{12}\mathbf{e}_{12} + T_{23}\mathbf{e}_{23} + T_{31}\mathbf{e}_{31} = 0, \quad (4)$$

where  $T_{ij}$  are the cortical tensions. Multiplying the above equation with  $\hat{\mathbf{e}}_{12}$  and  $\hat{\mathbf{e}}_{23}$  (where  $\hat{\mathbf{e}}$  denotes the vector orthogonal to  $\mathbf{e}$  and with the same magnitude) yields two equations

$$\begin{aligned} T_{23} \sin \alpha_{123} - T_{31} \sin \alpha_{312} &= 0, \\ T_{12} \sin \alpha_{123} - T_{31} \sin \alpha_{231} &= 0. \end{aligned} \quad (5)$$

Here,  $\alpha_{ijk}$  denotes the angle subtended by the interfaces  $(ij)$  and  $(jk)$ . An alternative, more geometric way to arrive at these equations is by applying the law of sines to the tension triangle, using that its angles are complementary to those at the vertex and  $\sin(\alpha - \pi) = \sin(\alpha)$ .

Eqs. (5)<sup>18</sup> equations do not constrain the overall level of tension. We fix this by setting the average tension to 1 which gives the solution. These equations are solved by

$$T_{12} = \mathcal{N} \sin \alpha_{231}, \quad T_{23} = \mathcal{N} \sin \alpha_{312}, \quad T_{31} = \mathcal{N} \sin \alpha_{123}, \quad (6)$$

with the normalization factor  $\mathcal{N} = \sum_{(ijk)} \sin \alpha_{ijk}$ .

The above calculation can be generalized to an arbitrary number of vertices. Notably, the equations become overconstrained once the set of vertices contains entire cells [31<sup>18</sup>]. This is because force balance implies that the tension vectors  $\mathbf{T}_{ij} = T_{ij}\mathbf{e}_{ij}$  form a triangulation (see below).

Here, we limit ourselves to local tension inference for the central interface in a cell quartet (see **Fig. 2A**). In this case, the equations are not overconstrained. Labelling the cells 1–4, the equations read

$$\begin{aligned} T_{23} \sin \alpha_{123} - T_{13} \sin \alpha_{312} &= 0, \\ T_{12} \sin \alpha_{123} - T_{13} \sin \alpha_{231} &= 0, \\ T_{34} \sin \alpha_{143} - T_{13} \sin \alpha_{314} &= 0, \\ T_{14} \sin \alpha_{143} - T_{13} \sin \alpha_{431} &= 0. \end{aligned} \quad (7)$$

We solve these equations under the normalization condition that the average of the “outer tensions”  $T_{12}$ ,  $T_{23}$ ,  $T_{34}$  and  $T_{14}$  is 1. The inferred value for “inner” cortical tension  $T_{13}$  then is that relative to the average tension of its neighbors. We call this the *relative tension* of a interface throughout the manuscript.

The use of local tension inference is justified because we are interested in local cell behaviors, namely rearrangements. Tension inference is also most robust on the local level, since this is where force balance, the underlying physical determinant of the link between mechanics and geometry, resides. In global tension inference, spurious large scale gradients can appear when small deviations from local force balance accumulate over large distances. For this reason we do not try to infer tension gradients in the magnitude of tension across the embryo, e.g. between the amnioserosa and the lateral ectoderm.

### Analysis of collapsing and emerging interfaces

For the analysis presented in **Fig. 2D** and **E**, collapsing and emerging interfaces were identified separately as described in Sec. 1.3. All events before 12 min were excluded from the analysis.

When a interface is short, the interface angles become highly susceptible to fluctuations of the vertex positions. We therefore excluded all timepoints where the central interface or one of its neighbors is shorter than a threshold length (0.75  $\mu\text{m}$ ).

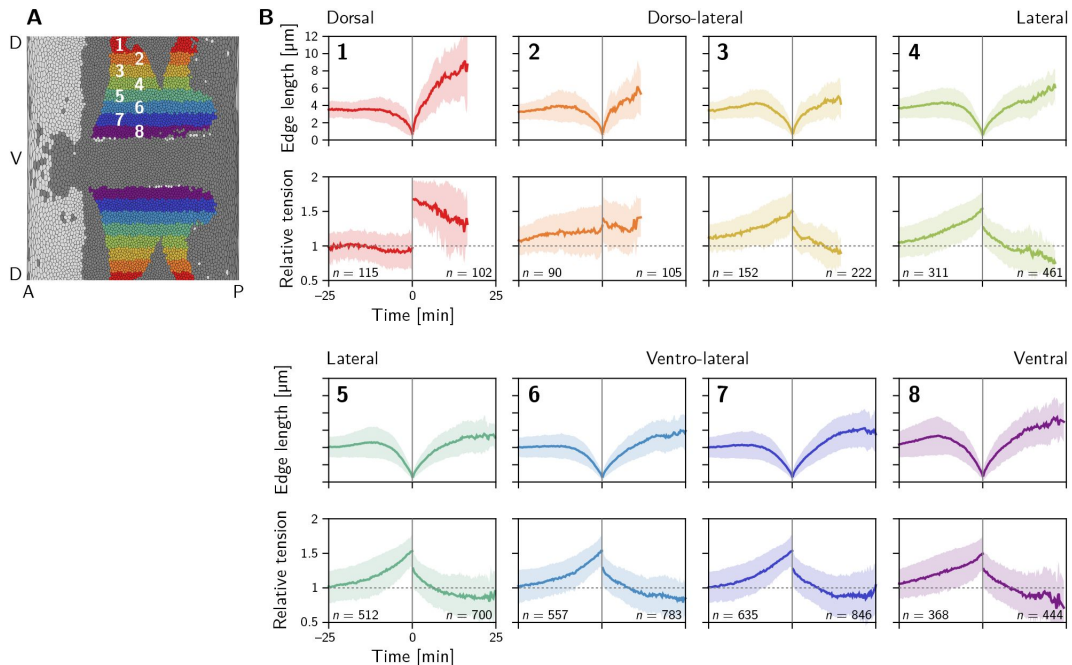


**Figure S3**

Length and relative tension of the central interface in intercalating cell quartets resolved by DV position. Two distinct classes of behavior are found: in the dorsal-most region (1), the relative tension remains constant at one on the contracting interface and jumps to a high value ( $\approx \sqrt{3}$ ) on the collapsing interface where it slowly relaxes back towards one. In contrast in the lateral ectoderm (regions 3-8), relative tension increases nonlinearly during interface contraction while the tension on the emerging interface starts at a lower value and rapidly relaxes to a value below one. Region 2 is an exception and appears to fall between the two above cases. Collapsing and emerging interfaces were analyzed separately, such that the numbers of events do not match exactly between them. Events are counted as part of a stripe when at least one of the two cells that come into contact comes from that stripe. Because cells converge along the DV axis in the lateral ectoderm, this implies that many interface emergence events are double counted there which inflates the number of emergence events relative to the collapse events.

This value was chosen because the vertex positions fluctuate about  $0.5\text{ }\mu\text{m}$  between timepoints. These fluctuations are partially due to intrinsic fluctuations in cortical tension and partially result from limitations in vertex localization during segmentation because of limited optical resolution.

Time series of interface length and relative tension are then aligned such that the interface collapse (respectively emergence) is at  $t = 0$ . **Figure S3** shows the pooled data resolved by the position of the quartet along the DV axis.

### 1.5 Tension-isogonal decomposition

Because the angles in the tension triangulation are complementary to the angle at vertices in the cell array, one can find a unique tension triangulation (up to a global scale factor) for a given physical cell array in force balance (see dashed gray arrow in **Fig. S7A**). However, the reverse is not true. For a given tension triangulation, there is a continuous family of cell arrays that share the same tension triangulation and that are related by *isogonal* deformations which change the interface lengths collectively while preserving the angles. (Mathematically, there are fewer triangulation vertices than cell vertices, so that the triangulation leaves one isogonal mode degree of freedom per cell undetermined. We will use this in Sec. 2 to define an “isogonal potential” that parametrizes the isogonal modes.)

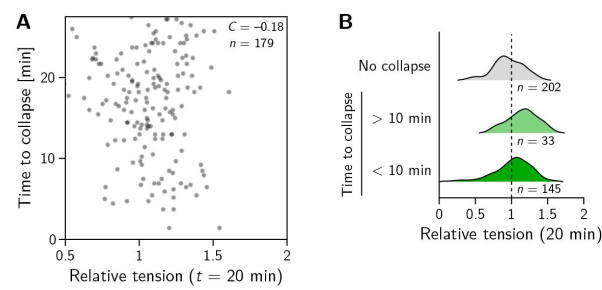


**Figure S4**

**A** In the amnioserosa relative tension is not correlated with the time until a interface collapses. **B** The distribution of relative tensions on interfaces that collapse is similar to those that persist. Compare to **Fig. 2H** and **J** for the quantification of interface collapses in the lateral ectoderm.

The isogonal degrees of freedom reflect tissue deformations that are not constrained by force balance of cortical tensions. This means that weaker contributions to stress, e.g. from intermediate filaments, microtubules and the nucleus in the cell interior, as well as externally applied stresses will drive the isogonal modes. This has two important consequences: (i) For the analysis of experimental data, it implies that we can decompose the tissue deformations into active, tension-driven and passive, isogonal contributions. (ii) For modeling, it implies that we need to specify a cell shape elasticity to fix the isogonal modes.

In the following, we discuss the details of the *tension-isogonal decomposition*. To achieve a well-defined decomposition of tissue deformation, we need to specify a reference tessellation that is uniquely determined by the tension triangulation. There will then be a unique isogonal deformation that deforms the reference configuration into the physical cell array. Fortunately, we do not need to explicitly construct the reference configuration. Rather, we use the triangulation formed by the cell centroids to quantify the physical tissue shape [57 [57](#)]. (This implies to some degree of coarse-graining, as information about the non-affine displacements of individual vertices is lost.) We can then obtain the isogonal deformation by comparing the tension triangulation to the centroidal triangulation.

### Single-vertex level

To make this construction concrete, we first consider a single tri-cellular vertex, with the associated tension triangle  $\hat{\mathbf{T}}_{ij}$  and the centroids  $\mathbf{c}_i$ . The indices  $i, j = 1, 2, 3$  label the three cells that meet at the vertex (see [Fig. S5A](#)). The tension triangle vectors  $\hat{\mathbf{T}}_{ij}$  are obtained by local tension inference based on the angles at the vertex (see Sec. 1.4). The orientation of the tension vectors is determined by demanding that they are at right angles to the cell-cell interfaces  $\mathbf{e}_{ij}$ . To fix the tension scale, we normalize the area of the tension triangle to unity. Fixing the tension triangle area is justified because it maintains the total area of the tension triangulation such that cell dilation/contraction are purely isogonal. The numerical value of the tension triangle area is immaterial, since it can be absorbed in the scale factor  $\eta$ .

We define the local isogonal deformation tensor  $\mathbf{I}_{\text{vertex}}$  such that it transforms the tension triangle into the centroidal triangle. Mathematically, this definition is written as the equations  $\eta \mathbf{I}_{\text{vertex}} \cdot \hat{\mathbf{T}}_{ij} = \mathbf{c}_j - \mathbf{c}_i$ ,  $i \neq j \in \{1, 2, 3\}$ . Since there are two independent displacement vectors in tension space and physical space each, these equations represent four independent constraints which uniquely determine the four components of the  $2 \times 2$  matrix  $\eta \mathbf{I}_{\text{vertex}}$ . The scale factor  $\eta$  converts units of tension (a.u.) into units of length. How we fix  $\eta$  is described below.

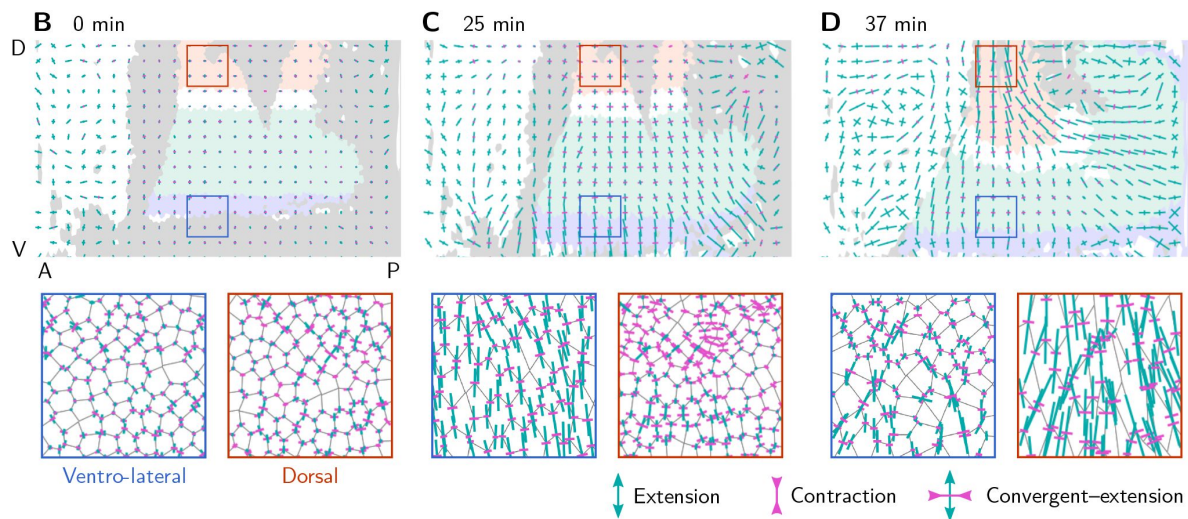
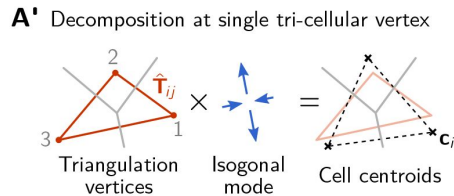
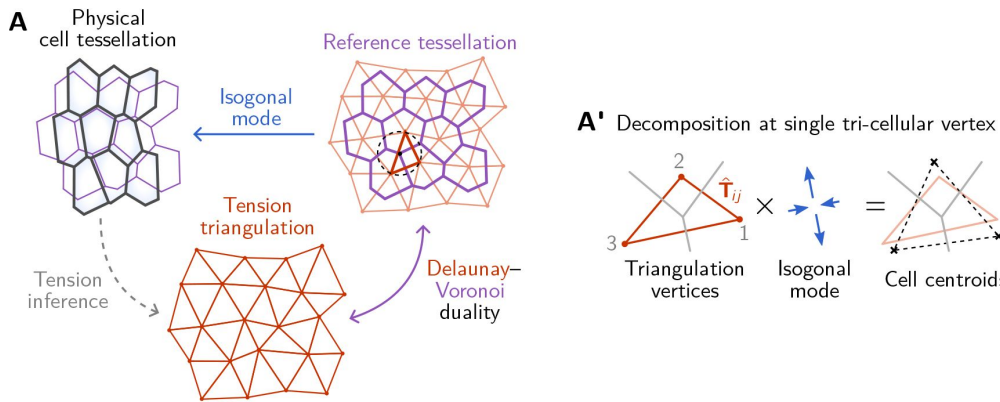


**Figure S5**

Tension-isogonal decomposition: Single-vertex analysis and coarse graining. **A** To a given tension triangulation (red), a corresponding dual cell array is obtained via the Voronoi construction (purple), which is based on the circumcircles of the triangles. Because the tension triangulation fixes only the angles, it leaves freedom for *isogonal* (angle-preserving) modes that collectively change the interface lengths. Deformations of the tissue can be decomposed into deformations of the tension triangulation and isogonal deformations. **A'** The tension-isogonal decomposition at a single vertex based on the tension triangulation vectors  $\hat{T}_{ij}$  and the cell centroids  $\mathbf{c}_i$ . The indices  $i, j$  label the three cells that meet at the vertex. **B–D** Coarse-grained isogonal strain (top) and isogonal strain at individual vertices (insets) for different timepoints. The initial isogonal strain (B) is minimized to fix the scale factor  $\eta$ . During VF invagination, the lateral ectoderm close to the ventral furrow is stretched (C). During GBE, the isogonal strain in the lateral ectoderm remains approximately constant while the amnioserosa gets stretched. Crosses show the principal axes of the local isogonal strain tensor. Bar length indicates the amount of strain (green = extension, magenta = contraction). Coarse-grained strain tensors were averaged on a grid with spacing 20  $\mu\text{m}$ . Insets show regions with size 50  $\times$  50  $\mu\text{m}^2$ .

The isogonal deformation tensor  $\mathbf{I}_{\text{vertex}}$  can be decomposed into a symmetric strain tensor  $\mathbf{U}$  and a rotation  $\mathbf{R}$  using polar decomposition  $\mathbf{UR} = \mathbf{I}_{\text{vertex}}$ . The appearance of a rotational component in the isogonal deformation might appear surprising at first glance, since isogonal modes leave angles at vertices invariant. However, the centroidal triangle can be sheared relative to the tension triangle by a simple shear which is a composition of pure shear with a rotation.

### Fixing the scale factor $\eta$

To fix  $\eta$  we use that the tension triangles are initially close to equilateral (as evidenced by the angle distribution peaked around  $\pi/3$ , see **Fig. 8L**). Recall that we have normalized the area of the tension triangle to unity by convention. For an equilateral tension triangle, the edge length  $T$  is uniquely determined by the area, giving  $T = 2/3^{1/4} \approx 1.52$ . To find  $\eta$ , we compare this value to the average edge length of the *centroidal triangles*, i.e. the average centroid distance between adjacent cells, which we find to be  $6.38 \mu\text{m}$ . The ratio of these two numbers gives a scale factor  $\eta \approx 4.2 \mu\text{m}$ . Note that the scale factor  $\eta \approx 4.2 \mu\text{m}$  minimizes the isogonal strain at  $t = 0$  (see **Fig. S5B**), indicating that at early times, the cell array geometry closely matches Voronoi dual of the tension triangulation. Indeed, we can also calculate  $\eta$  from the initial average cell-cell interface length  $\langle \lambda_0 \rangle \approx 3.6 \mu\text{m}$ . To this end, we use that the Voronoi dual to an equilateral triangulation with edge length  $T = 2/3^{1/4}$  is a hexagonal lattice with edge length  $T/\sqrt{3} \approx 0.88$ , giving  $\eta \approx 4.1$ . Finally, minimizing  $\langle \|\mathbf{I}\| \rangle$  at a reference time provides an alternative way to determine  $\eta$  in cases where the initial triangulation is not as uniform and regular as in the *Drosophila* blastoderm.

### Coarse-grained isogonal strain

To find the tissue scale isogonal strain, we coarse grain the isogonal deformation tensor on a square grid in the flat map projection (“pullback”). The grid spacing is set to  $20 \mu\text{m}$ , such that each grid facet contains ca 10–15 cells (grid facets near the poles contain less cells because of the distortion caused by the pullback projection). We calculate  $\mathbf{I}_{\text{vertex}}$  for all tri-cellular vertices in a grid facet and take the average to find  $\mathbf{I}_{\text{facet}}$ .

**Figures 4D** and **S5B–D** (top panels) show the isogonal strain tensor  $\mathbf{I}_{\text{facet}} - \mathbb{I}$ , where  $\mathbb{I}$  is the identity matrix. The bottom panels in **Fig. S5B–D** show the individual, single-vertex strain tensors  $\mathbf{I}_{\text{facet}} - \mathbb{I}$  at each vertex. Crosses indicate the principal eigenvectors of the strain tensors. The bar length is proportional to the eigenvalue. Green (magenta) indicates a positive (negative) eigenvalue, i.e. contraction (elongation).

To calculate the average isogonal deformation in different tissue regions (**Fig. 4E**), we first transform the single-vertex isogonal deformation tensor to the local corotating (“Lagrangian”) frame (see Sec. 1.2). This is important because the germ band rotates as it moves over the posterior pole during elongation.

To estimate the critical tension for T1s in the lateral ectoderm, we need the average isogonal contribution to the length of DV-oriented interfaces,  $\langle \Delta \zeta_{\text{iso}} \rangle$  (see SI Sec. 1.5). At the end of VF invagination ( $t = 25 \text{ min}$ ), we find  $\langle (\mathbf{I}_{\text{vertex}})_{22} \rangle \approx 1.538 \pm 0.006$ , where the index 2 denotes the DV component and the average is taken over cells in the lateral ectoderm (region shaded in blue in **Fig. S5C**). We thus have  $\langle \Delta \zeta_{\text{iso}} \rangle = (\mathbf{I}_{22} - 1) \langle \lambda_0 \rangle \approx 1.9 \mu\text{m}$  for DV-oriented interfaces, where  $\langle \lambda_0 \rangle \approx 3.5 \mu\text{m}$  is the average initial interface length.

**Figure S6** shows the coarse-grained isogonal strain in a *snail* mutant, where the ventral furrow is abolished. Without the ventral furrow invagination pulling on the lateral ectoderm, no isogonal strain is found in the lateral ectoderm before and during germ-band extension. This validates that isogonal strain reliably indicates tissue deformation driven by external forces, and, vice versa, the absence of isogonal strain indicates the lack of external driving forces.

### Filtering of degenerate tension triangles

When one of the angles at a vertex is close to  $\pi$ , the tension triangle becomes highly elongated. In fact, sometimes one of the angles at a vertex exceeds  $\pi$  due to fluctuations and inaccuracies in detection. In the tension inference, this leads to negative tensions. The (nearly) degenerate tension triangles, in turn lead to extreme apparent local isogonal deformations. We therefore exclude nearly degenerate tension triangles whose perimeter is larger than 8 after normalizing the area to 1 (ca. 2% of the tension triangles are filtered out this way).

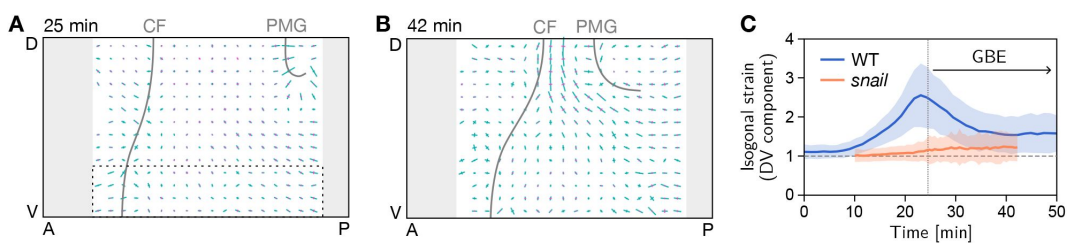


**Figure S6**

**Isogonal strain in a *snail* mutant.**

**A** At the onset of GBE (25 min) there is no isogonal strain in the lateral ectoderm, in particular the most ventral region (dashed box), where large isogonal strain is found in the WT (cf. **Fig. 6B** ). Gray lines mark the cephalic furrow (CF) and the invagination front of the posterior midgut (PMG). **B** Towards the end of GBE (42 min), significant isogonal strain has build up near the dorsal pole (amnioserosa), similar to the WT (cf. **Fig. 6B** '). **C** DV component of isogonal strain in the ventral ectoderm (dashed box in A). (Gray regions near the anterior and posterior pole where excluded from the image segmentation.)

### Tension-isogonal decomposition for cell quartets

The calculation for cell quartets (vertex pairs) is analogous to the case of single vertices. The two tension triangles associated to the inner vertices of the cell quartet form a “kite” (see [Fig. S7A](#)). We normalize tension such that the average area of the tension triangles is one. The quartet’s isogonal deformation tensor  $\mathbf{I}_{\text{quartet}}$  is defined such that it transforms the vectors  $\mathbf{T}_{ij}$  into the corresponding centroidal displacement vectors  $\mathbf{c}_j - \mathbf{c}_i$ . Here, we only use the vectors around the perimeter of the tension and centroidal kite. This ensures that the isogonal deformation tensor varies continuously through the cell neighbor exchange where the inner edge in the kite is flipped. As in the single-vertex case, we find  $\mathbf{I}_{\text{quartet}}$  using least squares.

To quantify the deformations of the tension kite and the physical cell quartet, we define the shape tensors

$$\mathbb{G}_T = \eta^2 \sum_{(ij)} \hat{\mathbf{T}}_{ij} \otimes \hat{\mathbf{T}}_{ij}, \quad (8)$$

$$\mathbb{G}_C = \sum_{(ij)} (\mathbf{c}_i - \mathbf{c}_j) \otimes (\mathbf{c}_i - \mathbf{c}_j), \quad (9)$$

where the index pairs  $(ij)$  run over cell pairs going around the quartet, i.e.  $(ij) = (12), (23), (34), (41)$ . Notably, with these definitions, one has the relation

$$\mathbf{I}_{\text{quartet}} \cdot \mathbb{G}_T \cdot \mathbf{I}_{\text{quartet}} \approx \mathbb{G}_C. \quad (10)$$

### Remarks on the Voronoi construction for the reference cell array

For the tension-isogonal decomposition, we have circumvented the explicit construction of a reference cell array by directly comparing the tension triangulation to the centroidal triangulation of the physical cells. This approach is particularly useful because a local isogonal deformation tensor can be obtained on the level of a single tri-cellular vertex.

The explicit construction of the reference cell array allows us understand the geometry of cell-neighbor exchanges and find a criterion for when they occur (see main text for a discussion simple symmetric case and the companion paper [\[32\]](#) for the general case). We define the reference tessellation using a generalized Voronoi construction based on the tension triangulation. The vertices of this generalized Voronoi tessellation are given by the circumcircle centers of the triangles in the triangulation. The generalized Voronoi tessellation is only free of self-intersections when the triangulation fulfills the Delaunay criterion that opposite angles in adjacent triangles must sum to a value smaller than  $\pi$ . As we will see, in the following section, this provides a purely geometric criterion for neighbor exchanges in the absence of isogonal strain. In the presence of isogonal strain, the reference can have self intersections (i.e. negative interface lengths). This is similar to how the reference state encoding plastic deformations in finite strain theory isn’t necessarily geometrically compatible [\[105\]](#).

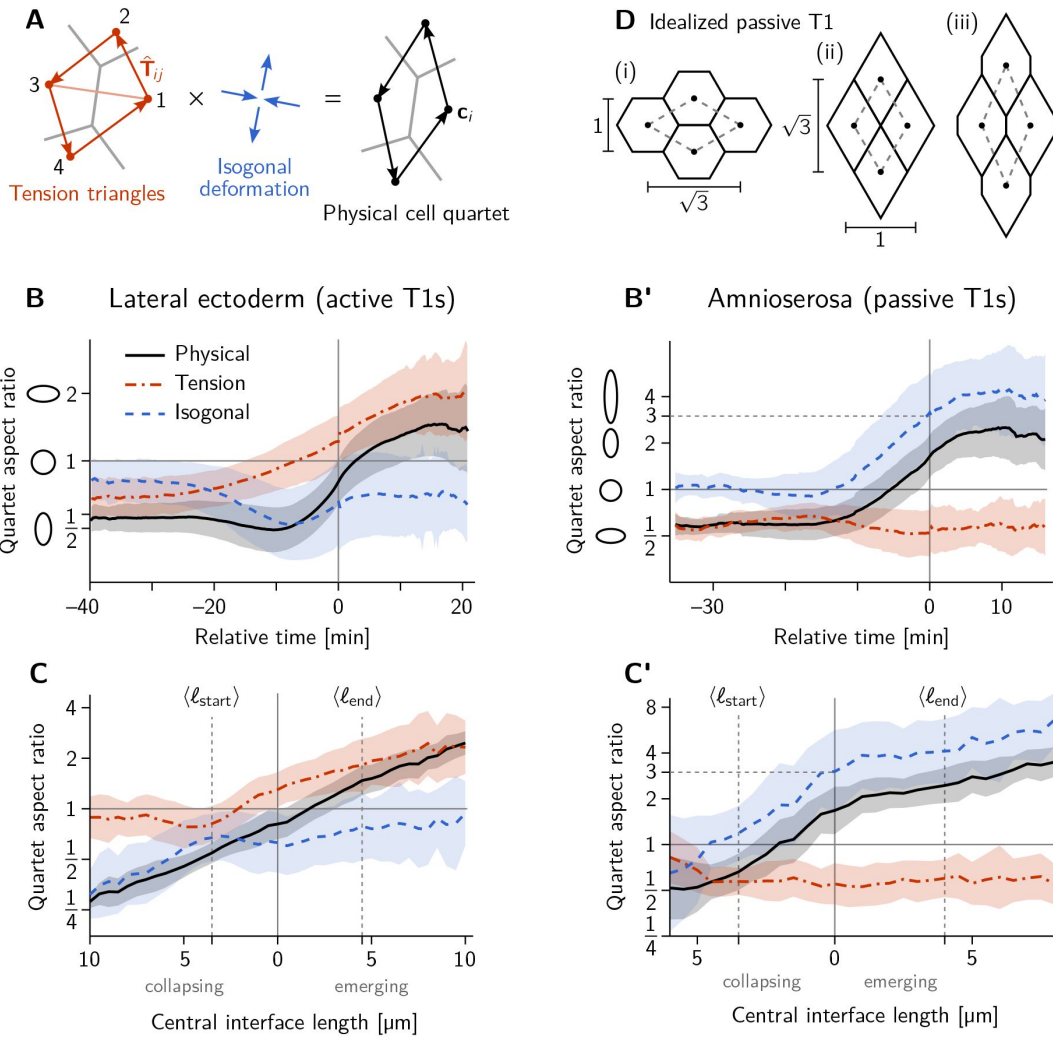


**Figure S7**

**A** Tension-isogonal decomposition for a cell quartet. The isogonal deformation is defined as the tensor that deforms the “kite” formed by the tension vectors  $\mathbf{T}_{ij}$  into the corresponding centroidal kite, formed from the cell centroids  $\mathbf{c}_i$ . The indices  $(ij)$  label the four cell pairs going around the kite: (12), (23), (34), (41). **B-C'** Quartet aspect ratio and eigenvalue ratio of the isogonal deformation tensor as a function of time relative to the T1 event (B and B') and as a function of the central interface's length (C and C'). The isogonal deformation seen in B from -20 to -10 min and in C for collapsing edge lengths  $> 4 \mu\text{m}$  is driven by the VF invagination which stretches the germ band.) **D** Passive intercalation of an idealized cell quartet composed of regular hexagons: (i) initial configuration; (ii) four-fold vertex configuration after area-preserving isogonal shear changing the aspect ratio by a factor 3; (iii) further isogonal deformation after the neighbor exchange. Black disks mark the cell centroids used to define the quartet shape (see A).

In general, the centroids of the generalized Voronoi cells will not coincide with the vertices of the tension triangulation. This means that the definition of the isogonal deformation tensor based on the tension triangulation vertices is not exactly identical to that based on an explicit Voronoi construction. However, the two agree for a periodic lattice of identical tension triangles. In this case, the vertices of the tension triangulation coincide exactly with the centroids of the generalized Voronoi tessellation. In other words, using the tension triangulation vertices to define isogonal deformations amounts to approximating tissue as locally lattice-like, which is valid when spatial gradients are small on the cell scale.

In passing, we note that the generalized Voronoi tessellation is not the only possible reference state. Any tessellation that is uniquely defined by a given tension triangulation is in principle a valid reference state. The Voronoi tessellation is a useful choice for the following analysis because the Voronoi cell shapes behave similar to the actual cell shapes and because it is defined purely geometrically. Other choices of the reference state might be of use depending on the particular question and when one has more detailed information about the mechanical properties of the cells.

## 1.6 Local tension anisotropy

From the tension vectors  $\mathbf{T}_{ij}$  at a vertex, we calculate the “tension anisotropy” tensor

$$\mathbb{T} = \frac{1}{N^2} \sum_{(ij)} \mathbf{T}_{ij} \otimes \mathbf{T}_{ij} \quad (11)$$

where the sum runs over pairs from the set of the three cells that meet at the vertex. The normalization factor  $N^2 = \sum_{(ij)} T_{ij}^2$  is chosen such that  $\text{Tr } \mathbb{T} = 1$ . The difference of the eigenvalues of  $\mathbb{T}$  quantifies the magnitude of tension anisotropy. When the interface angles at the vertex are all identical to  $120^\circ$  the tension anisotropy vanishes. For non-identical vertex angles the tension is locally anisotropic and the dominant eigenvector of  $\mathbb{T}$  points along the principal axis of stress. Anisotropic tension also implies that the tension triangle is non-equilateral. The tension triangle’s axis of elongation is perpendicular to the principal axis of tension because the tension triangle vectors are rotated by  $90^\circ$  relative to the interfaces (cf. [Fig. 2B](#)).

In passing, we note that the tension anisotropy tensor is closely related, but not exactly equal, to the stress tensor  $\sigma$ . Instead it has the form of a metric tensor and thus describes the local geometry of tension space. Specifically, the  $\mathbb{T}$  measures the *extrinsic* anisotropy of tension and is complementary to the *intrinsic* shape tensor that we will introduce in the next section.

## 1.7 Local tension configuration

In the main text, we argued that local configuration of tensions at a vertex is characterized by the shape of the tension triangle. Specifically, acute triangles correspond to tension cables, while obtuse triangles correspond to tension bridges (see [Fig. S8A](#)).

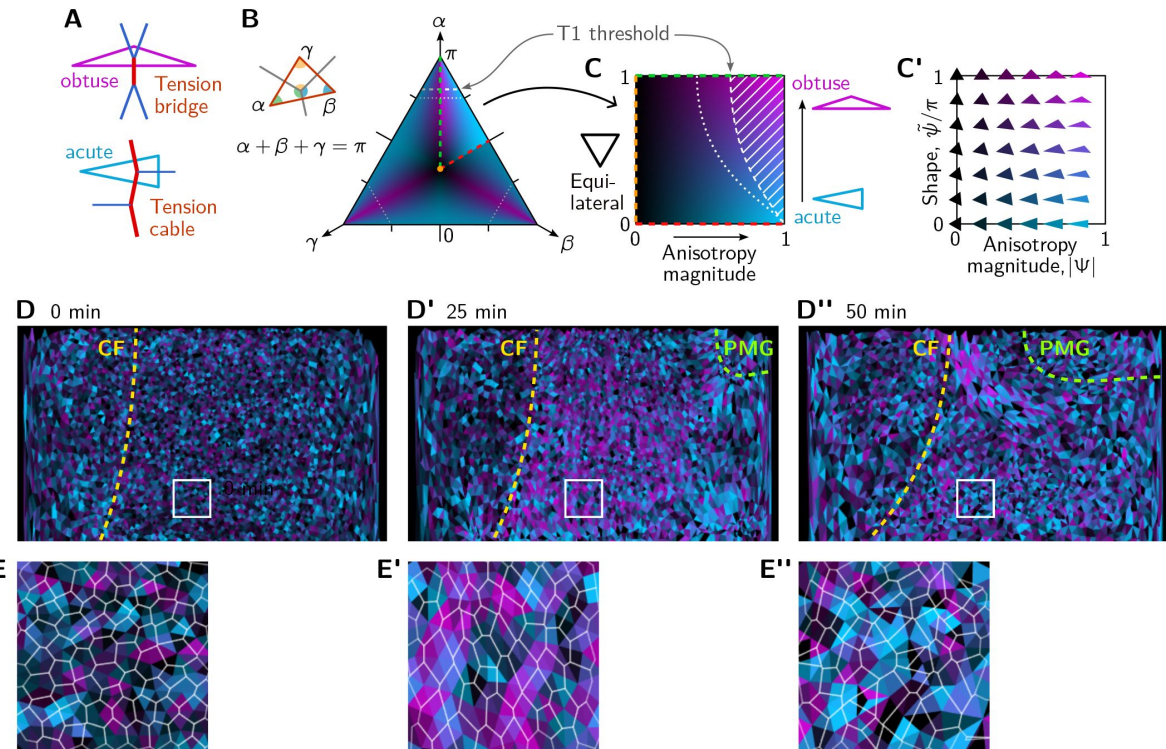


**Figure S8**

**Quantification of local tension configurations (LTC) in terms of tension triangle shape.**

**A** Tension triangle shape characterizes the local tension configuration. **B** Space of triangles in barycentric coordinates using the angles  $\alpha + \beta + \gamma = \pi$ . Color indicates the degree of acuteness vs obtuseness by hue from cyan to magenta and the magnitude of anisotropy by brightness (see text for details). A single fundamental domain is highlighted. The remaining shape space is composed of rotated and reflected copies of this fundamental domain, corresponding to permutations of the angles  $\alpha, \beta, \gamma$ . Dashed white lines indicate the threshold for neighbor exchanges based on the (generalized) Delaunay condition for pairs of identical tension triangles [32 [2](#)]. **C and C'** Triangle shape space spanned by the anisotropy magnitude  $|\Psi|$  and acute-vs-obtuse parameter  $\tilde{\psi}$  as axes. See main text for the definitions of  $\Psi$  and  $\tilde{\psi}$ . **D-D''** Snapshots showing the tension configuration at the onset of GBE. For each vertex, a triangle is drawn between the centroids of the adjacent cells and colored according to the tension triangle associated to the vertex. Yellow and green lines marks the cephalic furrow (CF) and the boundary of the posterior midgut (PMG), respectively. **E-E''** Blowups of the white square in (D-D'').

Whether a triangle is obtuse or acute is an *intrinsic* property, i.e. it is independent of the position, orientation and size of the triangle in the embedding space. The intrinsic shape of a triangle is given by its angles. Since these angles sum to  $\pi$ , we can represent the space of triangle shapes in barycentric coordinates (see **Fig. S8B**). The center of the barycentric shape space corresponds to an equilateral triangle, while the edges correspond to triangles where one angle is zero and the corners to triangles where two angles are zero. Because the order of labeling the angles in the triangle is arbitrary, the shape space is invariant under permutations of the angles and a single fundamental domain (highlighted in **Fig. S8B**) is representative.

In the triangle shape space, we have colored each point according to how anisotropic and how acute-vs-obtuse it is. We already know that we can read off the magnitude of anisotropy from the eigenvalues of the tensor  $\mathbb{T}$ , defined in the previous subsection. To quantify the shape (acute vs obtuse), we define a second tensor

$$(\mathcal{S})_{IJ} = \frac{1}{\mathcal{N}^2} \mathbf{T}_I \cdot \mathbf{T}_J, \quad (12)$$

where the indices  $I, J \in \{1, 2, 3\}$  are short hand labels for the three interfaces that meet a triangular vertex. Because  $\sum_I \mathbf{T}_I = 0$  (force balance), this tensor has the null vector  $(1, 1, 1)^T$ . To get rid of this nullspace, we go to barycentric coordinates by defining the pair of vectors,  $\tau_{1,2}$  that we pack into a matrix

$$\mathfrak{T} = \begin{pmatrix} \tau_1 \\ \tau_2 \end{pmatrix} = \frac{1}{\sqrt{2}\mathcal{N}} \begin{pmatrix} \mathbf{T}_1 - \mathbf{T}_2 \\ \mathbf{T}_3 / \sqrt{3} \end{pmatrix}. \quad (13)$$

These vectors have the defining property that they are orthogonal to one another and to the null vector  $(1, 1, 1)^T$  of  $\mathcal{S}$ . Now we can define the shape tensor

$$\mathbb{S} = \mathfrak{T} \mathfrak{T}^T = \begin{pmatrix} \|\tau_1\|^2 & \tau_1 \cdot \tau_2 \\ \tau_1 \cdot \tau_2 & \|\tau_2\|^2 \end{pmatrix}. \quad (14)$$

Observe that

$$\mathfrak{T}^T \mathfrak{T} = \tau_1 \otimes \tau_1 + \tau_2 \otimes \tau_2 = \mathbb{T}, \quad (15)$$

which implies that  $\mathbb{T}$  and  $\mathbb{S}$  share the same eigenvalues. In fact we can perform a singular value decomposition of  $\mathfrak{T}$

$$\mathfrak{T} = R(\psi/2) \Lambda R(-\phi), \quad (16)$$

where  $R(\phi)$  is the rotation matrix with angle  $\phi$  and  $\Lambda = \text{diag}(\lambda_1, \lambda_2)$  is a diagonal matrix of singular values whose squares  $\lambda_1^2, \lambda_2^2$  are the eigenvalues of  $\mathbb{T}$  and  $\mathbb{S}$ . Because we normalized the tension vectors,  $\text{Tr } \mathbb{T} = \text{Tr } \mathbb{S} = \lambda_1^2 + \lambda_2^2 = 1$ .  $\phi$  is the angle of the dominant eigenvector in physical space, which gives the orientation of the principal axis of stress. As we will see below, the angle  $\psi$  indicates whether the triangle is obtuse or acute. The reasoning to define the rotation based on  $\psi/2$  will become apparent below when we represent the shape tensor by a complex number.

The shape tensor  $\mathbb{S}$  has only two degrees of freedom, the difference of eigenvalues  $\lambda_1^2 - \lambda_2^2$  (which it shares with the tensor  $\mathbb{T}$ ) and the angle  $\psi$  that sets the orientation of its two orthogonal eigenvectors. We can represent  $\mathbb{S}$  by a complex number

$$\Psi = \frac{\tau_1^2 - \tau_2^2 + 2i \tau_1 \cdot \tau_2}{\tau_1^2 + \tau_2^2} = |\Psi| e^{i\psi}, \quad (17)$$

where  $|\Psi| = |\lambda_1^2 - \lambda_2^2|$  is the magnitude of tension anisotropy and the phase  $\psi$  is the “shape space angle” defined by [Eq. \(16\)](#).

Permutations of the edge indices  $a$  correspond to sign changes and rotations of  $\psi$  by integer multiples of  $2\pi/3$ . To mod out these group actions (which correspond to the symmetries of the barycentric shape space [Fig. S8B](#)), we define

$$\tilde{\psi} = |3\psi \bmod_{\pi} 2\pi| \in [0, \pi], \quad (18)$$

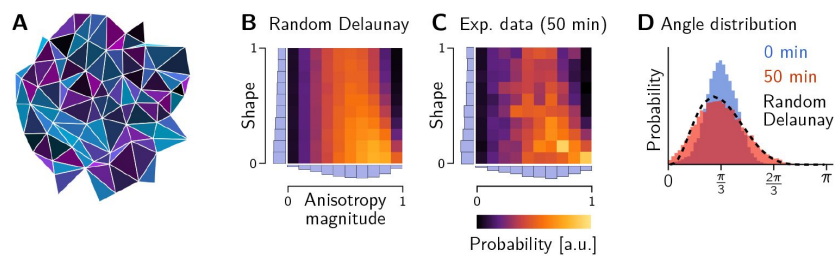


**Figure S9**

Shape statistics of random Delaunay triangulation. **A** Example of a random Delaunay triangulation seeded by a Ginibre random point process. Triangles have been colored according to the shape parameters ( $|\Psi|$ ,  $\tilde{\psi}$ ) (cf. Fig. S8C). **B and C** Histograms showing the triangle shape distribution for the Ginibre-based random Delaunay triangulation (B), tension triangles from the lateral ectoderm at the end of GBE (C, cf. Fig. 8C). **D** Initial and final angle distributions in the lateral ectoderm compared to a random Delaunay triangulation. The initial distribution matches a perturbed equilateral triangular lattice.

where  $x \bmod_d n = (x+d \bmod n) - d \in [-d, n-d]$  is the modulo operation with offset  $d$ . This shape parameter informs how acute or obtuse a tension triangle is. For an acute isosceles triangle,  $\tilde{\psi} = 0$ , whereas for an obtuse isosceles triangle  $\tilde{\psi} = \pi$ . For non-isosceles triangles,  $\tilde{\psi}$  takes values in  $[0, \pi]$  quantifying the relative degree of acuteness vs obtuseness. For an equilateral triangle,  $|\Psi| = 0$  and  $\tilde{\psi}$  is not defined. The axes  $|\Psi|$  and  $\tilde{\psi}/\pi$  span the space of triangle shapes shown in **Fig. S8**.

As an alternative to the above mathematical derivation of the shape parameter, we briefly discuss a more intuitive parameter as follows: For a given tension triangle, label its edges in ascending order of length (i.e.  $T_2$  and  $T_3$  will second highest and highest tension, respectively). We can now define a the parameter

$$p = 2 \frac{|T_2 - T_3|}{T_2 + T_3} \in [0, 1], \quad (19)$$

which quantifies the relative tension difference between the two largest tensions at a vertex. For a tension cable, there are two large tensions which are similar in magnitude, implying that  $p$  is small. For a tension bridge, there is one high tension edge meeting two low tension edges so  $p$  will be closer to 1. The maximal value  $p = 1$  is reached for  $T_1 = T_2 = T_3/2$ . Remarkably, to very good approximation  $p \approx |\Psi|\tilde{\psi}/\pi$ .

### Random Delaunay triangulation

As a reference for the triangle shape distributions, we generated random Delaunay triangulations based on the Ginibre random point process [106]. A small sample of such a random triangulation is shown in **Fig. S9A**. The histograms in the triangle shape space **Fig. S9B** shows good agreement between the Ginibre-based random Delaunay triangulation and the distribution of tension triangle shapes at the end of GBE. Moreover, the marginalized angle distribution (black dashed line), closely matches the experimentally observed distribution (**Fig. S9D**).

These findings suggest that the local coordination of cortical tensions is lost during GBE and that the local tension configurations approach a maximally disordered state.

## 2 Isogonal shear

As discussed in the main text (and further elaborated in Ref. [32]) our simulations show that a non-zero cell-level shear modulus is required for extension via active T1s. Here, we analyze the relation of cell-level and tissue-level shear modulus. Crucially, because of the dominance of cortical tensions, a tissue patch in our model will respond to externally applied forces via an isogonal deformation. We first show that an isogonal deformation can create tissue-scale pure shear (on the level of cell centroid displacement – the transformation of cell vertices is necessarily non-affine to preserve angles). Then we show that these pure shear modes correspond to the response of the tissue to external force by computing the Hessian of our cell elastic energy in the subspace spanned by isogonal deformations, and measure the shear modulus.

To show that isogonal modes can create pure shear, not just dilation/contraction of cells, we make use of the isogonal mode parametrization introduced in Ref. [31]. It assigns an isogonal “potential”  $\Theta_i$  to each cell, and calculates the cell displacements from the  $\Theta_i$  and the edge tension vectors. In the following, we will show that a constant gradient in the isogonal potential generates a uniform translation in real space. By integration, this implies that a quadratic spatial profile of the isogonal potential creates a pure shear.

Let us identify the real space edge unit vectors by the two adjacent cells  $\mathbf{e}_{ij} = -\mathbf{e}_{ji}$  and denote the corresponding tensions as  $T_{ij}$ . Then the tension vectors  $T_{ij}\hat{\mathbf{e}}_{ij}$  form a triangulation, where  $\hat{\mathbf{a}}$  denotes the normal vector to  $\mathbf{a}$ , i.e.  $\hat{\mathbf{a}} \cdot \mathbf{a} = 0$  and  $||\hat{\mathbf{a}}|| = ||\mathbf{a}||$ .

The isogonal displacement  $\mathbf{u}_{ijk}$  of the real space vertices  $\mathbf{r}_{ijk}$  (identified by the three adjacent cells) is given by

$$\mathbf{r}_{ijk} \rightarrow \mathbf{r}_{ijk} + \mathbf{u}_{ijk} = \mathbf{r}_{ijk} + \frac{1}{S_{ijk}} [\Theta_i \mathbf{T}_{jk} + (\text{cyc.})] \quad (20)$$

where  $S_{ijk} = \hat{\mathbf{T}}_{ij} \cdot \mathbf{T}_{ik}$  is the area of the tension triangle  $(ijk)$ .

First, observe that the uniform isogonal mode  $\Theta_i = \text{const.}$  has no effect on the vertex positions because

$$\mathbf{T}_{jk} + \mathbf{T}_{ki} + \mathbf{T}_{ij} = 0 \quad (\text{force balance}). \quad (21)$$

Now we aim to show that a constant gradient in  $\Theta_i$  drives a uniform displacement of the  $\mathbf{r}_{ijk}$ . Specifically, by uniform gradient we mean  $\Theta_i = \mathbf{t}_i \cdot \mathbf{a}$ , i.e. a linear gradient in the tension space ( $\mathbf{t}_i$  is the position of the tension triangulation vertex corresponding to cell  $i$ , such that  $\hat{\mathbf{T}}_{ij} = \mathbf{t}_j - \mathbf{t}_i$ ). To show that the displacement in real space is uniform, it is enough to show that two adjacent vertices are displaced identically. By induction, this implies that all displacements are identical. It is therefore sufficient to consider a quartet of cells ( $i = 1--4$ ), corresponding to a “kite” in tension space (note that  $\hat{\mathbf{a}} \cdot \mathbf{b}$  is identical to the wedge product  $\mathbf{a} \wedge \mathbf{b}$ .)

Because a constant can be arbitrarily added to all  $\Theta_i$ , we can set  $\Theta_1 = 0$  and thus have  $\Theta_i = \hat{\mathbf{T}}_{ij}$  for  $i = 2, 3, 4$ . The displacements now read

$$\mathbf{u}_{123} = \frac{1}{S_{123}} (\hat{\mathbf{T}}_{12} \cdot \mathbf{a} \mathbf{T}_{31} + \hat{\mathbf{T}}_{13} \cdot \mathbf{a} \mathbf{T}_{12}) \quad (22)$$

$$\mathbf{u}_{134} = \frac{1}{S_{134}} (\hat{\mathbf{T}}_{13} \cdot \mathbf{a} \mathbf{T}_{41} + \hat{\mathbf{T}}_{14} \cdot \mathbf{a} \mathbf{T}_{13}) \quad (23)$$

To show that these displacements are identical, we project them onto two conveniently chosen, linearly independent vectors, namely  $\hat{\mathbf{T}}_{12}$  and  $\hat{\mathbf{T}}_{13}$ . For the latter we find

$$\hat{\mathbf{T}}_{13} \cdot \mathbf{u}_{123} = \frac{1}{S_{123}} \hat{\mathbf{T}}_{13} \cdot \mathbf{a} \hat{\mathbf{T}}_{13} \cdot \mathbf{T}_{12} = -\hat{\mathbf{T}}_{13} \cdot \mathbf{a}, \quad (24)$$

$$\hat{\mathbf{T}}_{13} \cdot \mathbf{u}_{134} = \frac{1}{S_{134}} \hat{\mathbf{T}}_{13} \cdot \mathbf{a} \hat{\mathbf{T}}_{13} \cdot \mathbf{T}_{14} = -\hat{\mathbf{T}}_{13} \cdot \mathbf{a}, \quad (25)$$

where we used that  $\hat{\mathbf{T}}_{ij} \cdot \mathbf{T}_{ij} = 0$  and applied the definition of  $S_{ijk}$ .

Projecting (22) and (23) onto  $\hat{\mathbf{T}}_{12}$  gives

$$\hat{\mathbf{T}}_{12} \cdot \mathbf{u}_{123} = \frac{1}{S_{123}} \hat{\mathbf{T}}_{12} \cdot \mathbf{a} \hat{\mathbf{T}}_{12} \cdot \mathbf{T}_{31} = -\hat{\mathbf{T}}_{12} \cdot \mathbf{a} \quad (26)$$

$$\hat{\mathbf{T}}_{12} \cdot \mathbf{u}_{134} = \frac{1}{S_{134}} (\hat{\mathbf{T}}_{13} \cdot \mathbf{a} \hat{\mathbf{T}}_{12} \cdot \mathbf{T}_{41} + \hat{\mathbf{T}}_{14} \cdot \mathbf{a} \hat{\mathbf{T}}_{12} \cdot \mathbf{T}_{13}) \quad (27)$$

To show equality of these two right-hand sides, we use that given  $\hat{\mathbf{T}}_{13} \cdot \mathbf{a}$  and  $\hat{\mathbf{T}}_{14} \cdot \mathbf{a}$  we can find  $\mathbf{a}$  and substitute the result into  $\hat{\mathbf{T}}_{12} \cdot \mathbf{a}$ . We start by “expanding the identity”

$$\begin{pmatrix} -\hat{\mathbf{T}}_{13} \\ -\hat{\mathbf{T}}_{14} \end{pmatrix} \mathbf{a} = \begin{pmatrix} \hat{\mathbf{T}}_{13} \cdot \mathbf{a} \\ \hat{\mathbf{T}}_{14} \cdot \mathbf{a} \end{pmatrix} \Rightarrow \mathbf{a} = \begin{pmatrix} -\hat{\mathbf{T}}_{13} \\ -\hat{\mathbf{T}}_{14} \end{pmatrix}^{-1} \begin{pmatrix} \hat{\mathbf{T}}_{13} \cdot \mathbf{a} \\ \hat{\mathbf{T}}_{14} \cdot \mathbf{a} \end{pmatrix} \quad (28)$$

Explicitly writing out the inverse matrix then gives

$$\mathbf{a} = \frac{1}{\hat{\mathbf{T}}_{13} \cdot \hat{\mathbf{T}}_{14}} \begin{pmatrix} 1 & -1 \\ \hat{\mathbf{T}}_{14} & \hat{\mathbf{T}}_{13} \end{pmatrix} \begin{pmatrix} \hat{\mathbf{T}}_{13} \cdot \mathbf{a} \\ \hat{\mathbf{T}}_{14} \cdot \mathbf{a} \end{pmatrix} \quad (29)$$

With this, we find the relation

$$\hat{\mathbf{T}}_{12} \cdot \mathbf{a} = -\frac{1}{S_{134}} (\hat{\mathbf{T}}_{12} \cdot \mathbf{T}_{41} \hat{\mathbf{T}}_{13} \cdot \mathbf{a} + \hat{\mathbf{T}}_{12} \cdot \mathbf{T}_{13} \hat{\mathbf{T}}_{14} \cdot \mathbf{a}) \quad (30)$$

where we used  $\mathbf{T}_{ij} = -\mathbf{T}_{jk}$  to flip the indices on  $\mathbf{T}_{14}$ . Comparing to (26) and (27) now shows the identity of their RHSs.

Taken together, we have shown that

$$\hat{\mathbf{T}}_{12} \cdot \mathbf{u}_{123} = \hat{\mathbf{T}}_{12} \cdot \mathbf{u}_{134} \quad \text{and} \quad \hat{\mathbf{T}}_{13} \cdot \mathbf{u}_{123} = \hat{\mathbf{T}}_{13} \cdot \mathbf{u}_{134}, \quad (31)$$

Because  $\hat{\mathbf{T}}_{12}$  and  $\hat{\mathbf{T}}_{13}$  are linearly independent, it follows that  $\mathbf{u}_{123} = \mathbf{u}_{134}$ . QED. We just showed that a constant gradient in  $\Theta_i$  corresponds to a uniform displacement of the real space vertices  $\mathbf{r}_{ijk}$ . We can therefore think of  $\Theta(\mathbf{t})$  as a “potential” for the isogonal displacement field:  $\mathbf{u} \approx \nabla_{\mathbf{t}} \Theta$ , where the approximation is valid for slowly varying gradients and exact for constant gradients. The gradient  $\nabla_{\mathbf{t}}$  is taken in *tension space* because the function  $\Theta(\mathbf{t}_i) = \Theta_i$  is defined on the vertices of the tension triangulation  $\mathbf{t}_i$ .

A pure shear aligned with the coordinate axes is given by a displacement field  $\mathbf{u}(\mathbf{r}) = \varepsilon \text{ diag}(1, -1) \cdot \mathbf{r}$  and is therefore generated (approximately) by a quadratic isogonal potential  $\Theta = \varepsilon \mathbf{t}^T \cdot \text{diag}(-1, 1) \cdot \mathbf{t} = \varepsilon [(t^1)^2 - (t^2)^2]$ .

### 3 Simulation methods

In the following, we explain the simulation details for [Fig. 3](#), where we present a model of a single intercalating quartet. The code for the simulations shown is available online: [https://github.com/nikolas-clausen/geometric\\_basis\\_of\\_convergent\\_extension\\_simulation](https://github.com/nikolas-clausen/geometric_basis_of_convergent_extension_simulation).

Our model is based on two assumptions: adiabatic force balance, and dominance of cortical tensions. The first assumption means that we obtain the instantaneous cell geometry by solving force-balance equations. The second assumption means the we do so in two steps: first, we determine the interface angles from the cortical tension force balance. The remaining forces in the system are much weaker than cortical tensions and only affect the residual degrees of freedom, the isogonal modes.

In this work, we only consider a symmetric lattice of identical tension triangles, so a number of simplifications occur (the general case of a disordered cell array is the subject of the companion paper [\[107\]](#)). In this case, the cell shape is completely specified by the three vertex angles  $\varphi_i$  and edge lengths  $\ell_i$  at each vertex, with  $i \in \{0, 1, 2\}$ . Because the cell array is a symmetric lattice, the edge lengths  $\ell_i$  can be changed without affecting the angles and therefore parameterize the isogonal degrees of freedom.

We assume that the dynamics of the tensions are determined by a mechanosensitive feedback loop implementing positive tension feedback. To account for the dynamics of a junction post T1, each junction at a vertex is characterized by the total tensions  $T_i$ , and the passive tension  $T_{p,i}$ . The tensions at a vertex evolve according to:

$$\dot{T}_i = \tau_T^{-1} T_i^n - \tau_p^{-1} T_{p,i} - \frac{1}{3} \sum_k (\tau_T^{-1} T_k^n - \tau_p^{-1} T_{p,k}) \quad (32)$$

where  $n > 1$  and  $\tau_T$  is a time scale converting simulation time into minutes (fit to the data). The passive tension is 0 on all junctions except those that were newly created by a T1 transition. The initial value of  $T_p$  on those interfaces is discussed below. Given the tensions, we first calculate the angles from the tensions using the law of sines as  $\phi_i = \sin^{-1} \left( \frac{T_i}{2R} \right)$ , where  $R$  is the tension triangle circumradius.

## Cell shape energy

To determine the  $\ell_i$ , we minimize the an elastic energy based on the cell shape tensor:

$$S_C = \sum_i \frac{\mathbf{e}_i \otimes \mathbf{e}_i}{\ell_i} \quad (33)$$

where  $i$  runs over the edges of the cell  $\mathcal{C}$ , and  $\mathbf{e}_i$  is the vector pointing from one vertex of the interface to the other. Note that in this shape tensor, each edge contributes linearly in length to the cell shape. This means that artificially subdividing an edge has no effect on the cell shape tensor. This makes sense if we assume that the elasticity we aim to model using  $S$  resides in the cell interior (incompressibility, microtubules, intermediate filaments, nucleus). The shape tensor can also be defined using vectors from the cell centroid to its vertices (in the lattice, the two definitions are equivalent). An alternative definition of the elastic energy using  $\tilde{S}_C = \sum_i \mathbf{e}_i \otimes$  instead gives broadly similar results (although interface collapse happens more abruptly, because of the higher order non-linearity).

We assign a reference shape  $S_0$ . An isotropic  $S_0 \propto \text{Id}$  favours equilateral hexagons. We chose a slightly anisotropic reference shape  $S_0$  (15% anisotropy) to model the isogonal stretching caused by the ventral furrow before onset of GBE. This anisotropy sets the angle at which the inner interface collapses,  $\gamma_0 = 0$ . The experimental value of the collapse tension was therefore used to fit the  $S_0$ -anisotropy.

We define the cell elastic energy via

$$E_C = \lambda [\text{Tr}(S_C - S_0)]^2 + \mu \text{Tr}[(S_C - S_0)^2] \quad (34)$$

with bulk modulus  $\lambda$  and shear modulus  $\mu$ . We used a shear/bulk ration of  $\mu/\lambda = 0.1$ . Because of the separation of scales between cortical tensions and elastic energy baked into the model, the absolute values of  $\lambda, \mu$  are irrelevant. Further, for the case of active T1s, the results do not depend on  $\mu/\lambda$ , as long as  $\mu > 0$ .

The edge lengths  $\ell_i$  can now be determined by minimizing the elastic energy Eq. (34) w.r.t. the  $\ell_i$  for the angles determined by the tension dynamics.

## Comparison to area-perimeter elastic energy

Strikingly, within the singlequartet model, the “shape strain”  $S_C - S_0$  can always be set to 0 by choice of the edge lengths, and the energy  $E_C = 0$  throughout. This can already be seen from a degreeof-freedom count (three  $\ell_i$  for the three independent components of  $S_C - S_0$ ). The elastic

energy therefore acts only on the isogonal modes (i.e.  $\partial_{\phi_i} E_C|_{\ell_i=\text{minimizers}} = 0$ ) and there is no energy barrier for intercalations. Consequently, there is no need for noise to drive intercalations in our model. By contrast, for the widely-used areaperimeter elastic energy  $E = (A - A_0)^2 + (P - P_0)^2$  (where  $A, P$  are the cell area and perimeter, and  $A_0, P_0$  their target values) [54], there exists an energy barrier, and the inner interface  $\gamma$  only collapses when  $\phi_0 = \pi$ . This is shown in **Fig. S10B**. Note that the area-perimeter energy is a special case because of the geometric incompatibility of area and perimeter constraints. Combining area elasticity with shear elasticity based on the shape tensor,  $E = (A - A_0)^2 + \mu \text{Tr}[(S_C - S_0)^2]$ , (or perimeter elasticity with cell shape bulk elasticity) leads to similar results as [Eq. \(34\)](#). Note also that because of the degree-of-freedom count, the system is under-specified if the shear modulus is 0, foreshadowing the fact that without shear modulus, no convergence extension takes place [107].

### Myosin handover and passive tension

When an interface collapses,  $\gamma = 0$ , the tension triangulation is modified topologically: the edge corresponding to the collapsed interfaces is replaced by one corresponding to the new interface (triangulation “flip”). To complete our model, we must specify the initial conditions of this new edge.

As shown in [Fig. 3D](#), we propose a myosin handover mechanism to explain the extension of the new interface post intercalation. A interface with cortical tension  $T$  is comprised of the adherens-junctional actomyosin cortex of the two adjacent cells, which are coupled mechanically via adherens junctions. Under force balance, the total tension  $T$  has to be constant along the cortex, but the individual tensions on either side can be non-uniform, as the resulting traction forces are exchanged via adherens junctions. In the following, we assume as a first order approximation that the level of active tension (i.e. myosin concentration) varies linearly along an interface (similar calculations have been performed in Ref. [56] to calculate interfacial shear stress). This allows us to geometrically obtain the myosin concentration at the individual cortices that will form the two juxtaposed sides of the new interface (see [Fig 3D](#)).

Consider the tensions  $T_0, T_1, T_2$  at a vertex, and let 0 be the interface about to collapse. The three cells that meet at the vertex will be referred to by (01), (12), (21) (where e.g. (01) is the cell abutting interfaces 0 and 1). Let  $m_{01}, m_{12}, m_{21}$  be the motor molecule concentrations (in units of tension) at the vertex in the junctional cortices of the three cells. Then, the tensions are related to the motor molecule concentrations as:

$$T_0 = m_{21} + m_{01}, \quad T_1 = m_{01} + m_{12}, \quad T_2 = m_{12} + m_{21}.$$

This uses the assumption of myosin continuity at vertices, and the fact that the tension on an interface is the sum of the tensions of the two cortices that make it up. The motor molecule concentration on the cortex belonging to the new interfaces, post collapse, will be equal to  $m_{12}$ . Solving for this in terms of the tensions:

$$m_{12} = \frac{T_1 + T_2 - T_0}{2}$$

The new interface consists of two cortices, coming from the two vertices of the old junction. Let the tensions at the two triangles be  $T_0, T_1, T_2$  and  $T_0, T'_1, T'_2$ . Let  $T_a$  be the active tension on the new junction immediately after the T1. It is the equal to

$$T_a = \frac{(T_1 + T_2 - T_0) + (T'_1 + T'_2 - T_0)}{2} \quad (35)$$

Note however that the total tension  $T_n$  on the new junction is not necessary equal to  $T_a$ . The total tension is defined geometrically from the angles at the new junction (or, equivalently, the tension triangle vertices). Indeed, generally,  $T_n > T_a$ , i.e. the active tension on the new junction is not enough to balance the tension due to the adjacent edges. We introduce a passive tension  $T_p$  on the new edge which balances this deficit

$$T_p = T_n - T_a = T_n - (m_{12} + m'_{12})$$

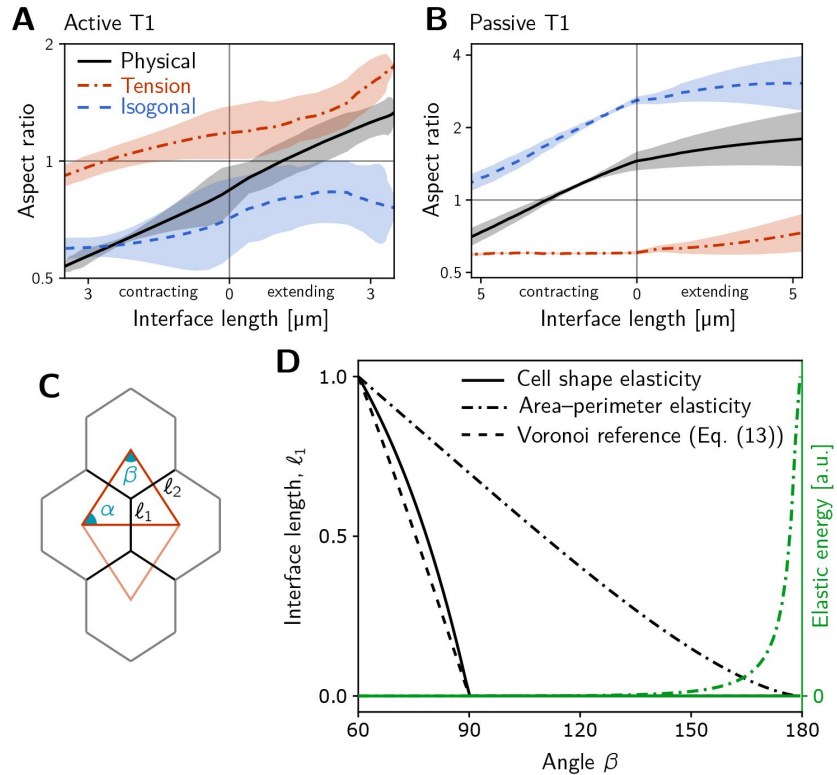


**Figure S10**

Additional quantification of single-quartet simulations. **A and B** Tensionisogonal decomposition of cell quartet shape during active (A) and passive (B) T1s in the single-quartet model (same simulations as Fig. 3E-F). **C** Geometry of a quartet of identical cells and the corresponding tension triangles (red) parametrized by the angles  $\alpha, \beta$ . **D** Comparison of different cell shape elastic energies which determine the cell interface lengths  $\ell_1$  as a function of the angles  $\alpha, \beta$ . The plot shows the inner interface length for a left-right symmetric quartet (i.e. an isosceles tension triangle) where  $\alpha = (\pi - \beta)/2$ . For reference, the inner interface length  $\ell_{\text{ref}}$  for a Voronoi tessellation based on the tension triangles is shown (dashed black line). The interface length obtained by minimizing elastic energy Eq. (2) with isotropic target shape (solid black line) closely follows the reference Voronoi length and vanishes at the same critical angle. By contrast, minimizing the “areaperimeter” energy of the vertex-model  $E_{\text{cell}} \sim (A - A_0)^2 + (P - P_0)^2$  gives a interface length (dot-dashed black line) that vanishes only for  $\beta \rightarrow \pi$  and the elastic energy diverges in this limit (dashed green line). This implies that tension dynamics, changing the angles at vertices, cannot drive T1s for this choice of elastic energy in the absence of noise.

For example, if a perfectly symmetric quartet collapses when the vertex angle facing the collapsing edge is  $90^\circ$ ,  $T_1 = T_2 = T'_1 = T'_2 = 1$  and  $T_0 = T_n = \sqrt{2}$ . Therefore,  $T_{a,n} = 2 - \sqrt{2} \approx 0$  and  $T_{p,n} = \sqrt{2} - (2 - \sqrt{2}) \approx 0.8$ . Note that by the triangle inequality, for any convex quadrilateral with perimeter  $P$  and diagonals  $D_1, D_2$ , one has  $P/2 \leq D_1 + D_2 \leq P$ . Applying this to the quadrilateral formed by the two tension triangles at the collapsing interface, we get  $T_{a,n} \geq 0$  and  $T_{p,n} \geq 0$ : the handover formula always results in positive active and passive tensions. Further, the “handover” mechanism robustly generates irreversible T1s: if a junction were to collapse back after a T1, the newly formed junction would inherit high myosin levels and therefore be likely to collapse again.

The passive tension subsequently relaxes visco-elastically with rate  $\tau_p^{-1}$ :  $\dot{T}_p = -\tau_p^{-1}T_p$ . Combining this with the feedback equation yields [Eq. \(32\)](#). The relaxation rate  $\tau_p = \tau_f/6$  was fit to the measured tension decay post intercalation.

## Numerical implementation

We integrated [Eq. \(32\)](#) using a 4th order RungeKutta method as implemented in the SciPy software package [108], using as initial conditions the vertex angles in the experimental data at time  $t = 5$  min (the vertex angles from the data were temporally smoothed with a window of 2 min to reduce noise).

In our simulations, we triggered an intercalation event once the collapsing edge length, as determined by energy minimization, reached 0. We then initialized the passive tension as given by [Eq. \(35\)](#) and simulated the combined active/passive tension dynamics. The overall time and length-scale were likewise fit to the data. The feedback exponent was  $n = 4$ . Numerically, energy minimization was carried out using the `scipy.optimize` package, specifically its Nelder-Mead optimizer.

## Passive intercalation

Within the same framework, we can also model passive intercalations, shown in [Fig. 3F](#). We can either specify cortical tension dynamics (in this case, tension homeostasis,  $\dot{T} \sim -(T - 1)$ ) and then minimize an elastic energy that includes the influence of externally imposed shear. This will trivially reproduce the isogonal behavior shown in [Fig. 2E](#). Alternatively one can reason that on the dorsal side there is very little active tension (cortical myosin), so that cortical tensions are expected to be low. Then, the passive elastic energy, together with the imposed shear, should determine the also angles. Both models are consistent with the data.

In [Fig. 3F](#), we show simulations based on the latter option. We implement the externally imposed shear causing the passive intercalations as follows. We calculate the four cell centroids  $\mathbf{c}_i$  of the cell quartets, and demand that at simulation time  $t$

$$\mathbf{c}_i(t) = S(t) \cdot \mathbf{c}_i(t = 0) \quad (36)$$

where  $S(t)$  is a diagonal matrix representing (area-preserving) shear, increasing over time with constant shear rate  $\gamma$ .

We then minimize the elastic energy under the constraint (numerically, this is done by adding a penalty term to the elastic energy), but this time with respect to both the lengths  $\ell_i$  and the angles  $\varphi_i$ . As long as the shear modulus  $\mu \ll \lambda$ , this procedure results in approximately isogonal behavior. We chose  $\mu = 0.01\lambda$ . To obtain continuity across the intercalation, the rest shape  $S_0$  needs to be adjusted. Otherwise, post intercalation, the cell quartet jumps back to a hexagonal lattice configuration. This can be done by introducing a viscous relaxation scale for the rest shape; for

simplicity, we simply set the rest shape to the current shape tensor at the time of intercalation. The initial conditions are obtained by varying the angle between the shear axis and the collapsing interface orientation from 0° – 25°.

## 4 PIV and tissue tectonics analysis of experiments assessing the role of the posterior midgut

To obtain additional evidence on the influence of posterior midgut (PMG) invagination on GBE, we carried out a quantitative re-analysis of data published in Ref. [19]. In brief, in Ref. [19] – among other experiments and analyses – the authors used an IR-laser to fuse germ band tissue to the overlaying vitelline membrane by cauterization. This creates a “cauterization fence” along the posterior end of the germ band which mechanically uncouples the germ band and the region of PMG invagination [19]. The authors then analyse tissue between the cauterization fence and the PMG. In wild-type embryos, they find that this tissue rips off from the cauterization fence, indicating pulling forces. This tissue ripping is also observed in mutants where force generation in the germ band is impaired (*eve/rnt* and *twi/snl*). In contrast, for *tor* mutants where the PMG does not invaginate, no tissue ripping is observed [19]. This suggests that the PMG exerts a pulling force on the germ band.

However, tissue ripping is only a qualitative measure for such pulling forces. To obtain a more quantitative estimate of the relative contributions of internally generated forces in the germ band and “external” pulling forces from the PMG we re-analyzed the movies from [19] using Particle Image Velocimetry (PIVlab [109]) to measure the average tissue flow in the region posterior to the cauterization fence. The results are shown in Fig. S11. In *tor* embryos, where no PMG invagination occurs, there is essentially no tissue flow, in line with the qualitative assessment from tissue ripping. Notably, in the *eve/rnt* and the *twi/snl* embryo, tissue flow velocity posterior of the cauterized region is reduced by about two-fold compared to wild-type. This shows that impairing active force generation in the germ band has a strong influence on the tissue flow anterior of the PMG. This flow originates from the dorso-ventral contraction of the germ band that pulls on the dorsal amnioserosa and drives the hyperbolic flow there [18]. These quantitative observations based on the data from [19] are in line with the much reduced tissue flow in *eve* and *twist* embryos imaged *in-toto* using light-sheet microscopy [74].

This above tissue flow quantification, is complemented by the following “anatomical” considerations. As shown in Ref. [64], the tissue that will invaginate to form the posterior midgut consists of two distinct regions, the “initiation” and the “propagation” region, both have an AP-length of approximately 7–8 cell diameters. On the other hand, the germ band has a length of approximately 40 cell diameters (Fig. 1A). Invagination of the initiation domain can hence create at most a strain  $\approx 8/40 = 0.2$  (since the initiation region is anchored on its anterior side). Moreover, the PMG forms a deep fold separating its anterior front, where the force driving invagination originates [64], from the germ band. It is unclear how a pulling force could be transmitted across this fold. Instead, the pulling force originating from the hyperbolic fixed point on the dorsal pole bypasses the PMG laterally where it manifests as isogonal stretching along the AP axis (see Fig. 6B').

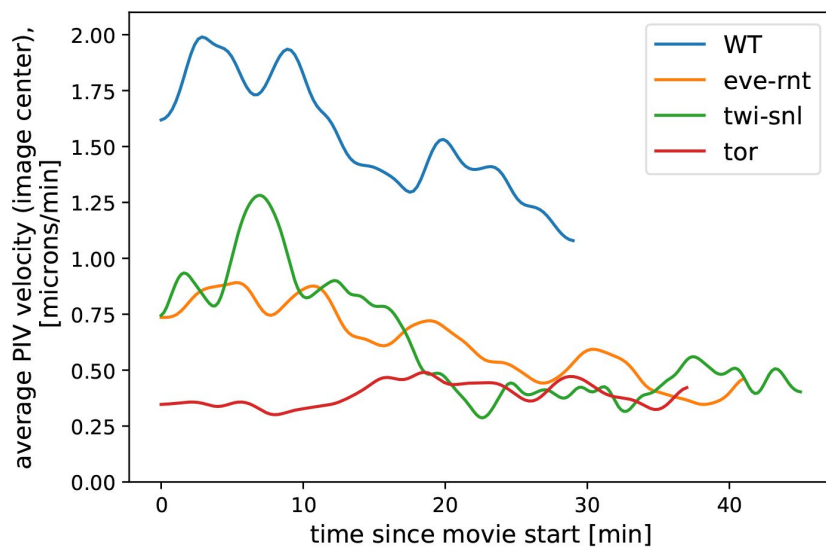


**Figure S11**

PIV-analysis of tissue flow ahead of a DV cauterization fence in different genetic backgrounds. In the *eve/rnt* and the *twi/snl* embryo, where active force generation in the germ band is impaired, tissue flow is strongly reduced compared to WT. For analysis, we excluded the cauterization fence itself. Data from Ref. [19] ([19](#)) ( $N = 1$  movie for each genotype).

## References

- [1] Mao Y., et al. (2011) **Planar polarization of the atypical myosin Dachs orients cell divisions in *Drosophila*** *Genes & Development* **25**:131–136
- [2] Gillies T. E., Cabernard C. (2011) **Cell Division Orientation in Animals** *Current Biology* **21**:R599–R609
- [3] Huebner R. J., Wallingford J. B. (2018) **Coming to Consensus: A Unifying Model Emerges for Convergent Extension** *Developmental Cell* **46**:389–396
- [4] Hales K. G., Korey C. A., Larracuente A. M., Roberts D. M. (2015) **Genetics on the Fly: A Primer on the *Drosophila* Model System** *Genetics* **201**:815–842
- [5] Krzic U., Gunther S., Saunders T. E., Streichan S. J., Hufnagel L. (2012) **Multiview light-sheet microscope for rapid *in toto* imaging** *Nature Methods* **9**:730–733
- [6] Mitchell N. P., et al. (2022) **Mitchell, N. P. et al. Morphodynamic Atlas for *Drosophila* Development** doi:10.1101/2022.05.26.493584 (2022). URL <http://biorxiv.org/lookup/doi/10.1101/2022.05.26.493584>. <https://doi.org/10.1101/2022.05.26.493584>
- [7] Stern T., Shvartsman S. Y., Wieschaus E. F. (2022) **Deconstructing gastrulation at single-cell resolution** *Current Biology* **32**:1861–1868
- [8] Heemskerk I., Streichan S. J. (2015) **Tissue cartography: Compressing bio-image data by dimensional reduction** *Nature Methods* **12**:1139–1142
- [9] Gilbert S. F., Barresi M. J. F. (2016) **Developmental Biology**
- [10] Leptin M. (1995) ***Drosophila* Gastrulation: From Pattern Formation to Morphogenesis** *Annual Review of Cell and Developmental Biology* **11**:189–212
- [11] Martin A. C., Kaschube M., Wieschaus E. F. (2009) **Pulsed contractions of an actin-myosin network drive apical constriction** *Nature* **457**:495–499 <https://doi.org/10.1038/nature07522>
- [12] Martin A. C. (2020) **The Physical Mechanisms of *Drosophila* Gastrulation: Mesoderm and Endoderm Invagination** *Genetics* **214**:543–560
- [13] Irvine K., Wieschaus E. (1994) **Cell intercalation during *Drosophila* germband extension and its regulation by pair-rule segmentation genes** *Development* **120**:827–841
- [14] Zallen J. A., Wieschaus E. F. (2004) **Patterned Gene Expression Directs Bipolar Planar Polarity in *Drosophila*** *Developmental Cell* **6**:343–355
- [15] Bertet C., Sulak L., Lecuit T. (2004) **Myosin-dependent junction remodelling controls planar cell intercalation and axis elongation** *Nature* **429**:667–671
- [16] Blanchard G. B., et al. (2009) **Tissue tectonics: Morphogenetic strain rates, cell shape change and intercalation** *Nature Methods* **6**:458–464

- [17] Farrell D. L., Weitz O., Magnasco M. O., Zallen J. A. (2017) **SEGGA: A toolset for rapid automated analysis of epithelial cell polarity and dynamics** *Development* **144**:1725–1734
- [18] Streichan S. J., Lefebvre M. F., Noll N., Wieschaus E. F., Shraiman B. I. (2018) **Global morphogenetic flow is accurately predicted by the spatial distribution of myosin motors** *eLife* **7**
- [19] Collinet C., Rauzi M., Lenne P.-F., Lecuit T. (2015) **Local and tissue-scale forces drive oriented junction growth during tissue extension** *Nature Cell Biology* **17**:1247–1258
- [20] Butler L. C., et al. (2009) **Cell shape changes indicate a role for extrinsic tensile forces in Drosophila germ-band extension** *Nature Cell Biology* **11**:859–864
- [21] Lye C. M., et al. (2015) **Mechanical Coupling between Endoderm Invagination and Axis Extension in Drosophila** *PLOS Biology* **13**
- [22] Gehrels E. W., Chakrabortty B., Perrin M.-E., Merkel M., Lecuit T. (2023) **Curvature gradient drives polarized tissue flow in the Drosophila embryo** *Proceedings of the National Academy of Sciences* **120**
- [23] Lecuit T., Lenne P.-F., Munro E. (2011) **Force Generation, Transmission, and Integration during Cell and Tissue Morphogenesis** *Annual Review of Cell and Developmental Biology* **27**:157–184
- [24] Blankenship J. T., Backovic S. T., Sanny J. S., Weitz O., Zallen J. A. (2006) **Multicellular Rosette Formation Links Planar Cell Polarity to Tissue Morphogenesis** *Developmental Cell* **11**:459–470
- [25] Fernandez-Gonzalez R., Simoes S. d. M., Röper J.-C., Eaton S., Zallen J. A. (2009) **Myosin II Dynamics Are Regulated by Tension in Intercalating Cells** *Developmental Cell* **17**:736–743
- [26] Gustafson H. J., Claussen N., De Renzis S., Streichan S. J. (2021) **Patterned mechanical feedback establishes a global myosin gradient** <https://doi.org/10.1101/2021.12.06.471321>
- [27] Ma X., Lynch H. E., Scully P. C., Hutson M. S. (2009) **Probing embryonic tissue mechanics with laser hole drilling** *Physical Biology* **6**
- [28] Chiou K. K., Hufnagel L., Shraiman B. I. (2012) **Mechanical Stress Inference for Two Dimensional Cell Arrays** *PLoS Computational Biology* **8**
- [29] Ishihara S., et al. (2013) **Comparative study of non-invasive force and stress inference methods in tissue** *The European Physical Journal E* **36**
- [30] Noll N., Streichan S. J., Shraiman B. I. (2020) **Variational Method for Image-Based Inference of Internal Stress in Epithelial Tissues** *Physical Review X* **10**
- [31] Noll N., Mani M., Heemskerk I., Streichan S. J., Shraiman B. I. (2017) **Active tension network model suggests an exotic mechanical state realized in epithelial tissues** *Nature Physics* **13**:1221–1226
- [32] Claussen N. H., Brauns F., Shraiman B. I. (2023) **A Geometric Tension Dynamics Model of Epithelial Convergent Extension**

[33] Bambadekar K., Clément R., Blanc O., Chardès C., Lenne P.-F. (2015) **Direct laser manipulation reveals the mechanics of cell contacts in vivo** *Proceedings of the National Academy of Sciences* **112**:1416–1421

[34] Munjal A., Philippe J.-M., Munro E., Lecuit T. (2015) **A self-organized biomechanical network drives shape changes during tissue morphogenesis** *Nature* **524**:351–355

[35] Lecuit T., Yap A. S. (2015) **E-cadherin junctions as active mechanical integrators in tissue dynamics** *Nature Publishing Group* **17**:533–539 <https://doi.org/10.1038/ncb3136>

[36] Prost J., Jülicher F., Joanny J.-F. (2015) **Active gel physics** *Nature Physics* **11**:111–117

[37] Doubrovinski K., Swan M., Polyakov O., Wieschaus E. F. (2017) **Measurement of cortical elasticity in Drosophila melanogaster embryos using ferrofluids** *Proceedings of the National Academy of Sciences* **114**:1051–1056

[38] Cheikh M. I., et al. (2022) **A comprehensive model of Drosophila epithelium reveals the role of embryo geometry and cell topology in mechanical responses** <https://doi.org/10.1101/2022.08.12.503803>

[39] Kong W., et al. (2019) **Experimental validation of force inference in epithelia from cell to tissue scale** *Scientific Reports* **9**

[40] Maxwell J. C. (1864) **On reciprocal figures and diagrams of forces** *The London, Edinburgh, and Dublin Philosophical Magazine and Journal of Science* **27**:250–261

[41] Varignon P. (1725) **Nouvelle Mécanique Ou Statique, Dont Le Projet Fut Donné En 1687: Ouvrage Posthume**

[42] Tighe B. P., van Eerd A. R. T., Vlugt T. J. H. (2008) **Entropy Maximization in the Force Network Ensemble for Granular Solids** *Physical Review Letters* **100**

[43] Stern T., Shvartsman S. Y., Wieschaus E. F. (2020) **Template-based mapping of dynamic motifs in tissue morphogenesis** *PLOS Computational Biology* **16**

[44] Duda M., et al. (2019) **Polarization of Myosin II Refines Tissue Material Properties to Buffer Mechanical Stress** *Developmental Cell* **48**:245–260

[45] Sknepnek R., Djafer-Cherif I., Chuai M., Weijer C., Henkes S. (2023) **Generating active T1 transitions through mechanochemical feedback** *eLife* **12**

[46] Clément R., Dehapiot B., Collinet C., Lecuit T., Lenne P.-F. (2017) **Viscoelastic Dissipation Stabilizes Cell Shape Changes during Tissue Morphogenesis** *Current Biology* **27**:3132–3142

[47] Farhadifar R., Röper J.-C., Aigouy B., Eaton S., Jülicher F. (2007) **The Influence of Cell Mechanics, Cell-Cell Interactions, and Proliferation on Epithelial Packing** *Current Biology* **17**:2095–2104

[48] Hufnagel L., Teleman A. A., Rouault H., Cohen S. M., Shraiman B. I. (2007) **On the mechanism of wing size determination in fly development** *Proceedings of the National Academy of Sciences* **104**:3835–3840

[49] Vanderleest T. E., et al. (2018) **Vertex sliding drives intercalation by radial coupling of adhesion and actomyosin networks during Drosophila germband extension** *eLife* **7**

- [50] Kim S., Amini R., Campàs O. (2022) **A nuclear jamming transition in vertebrate organogenesis** *biorxiv*
- [51] Ramms L., et al. (2013) **Keratins as the main component for the mechanical integrity of keratinocytes** *Proceedings of the National Academy of Sciences* **110**:18513–18518
- [52] Charrier E. E., et al. (2018) **The desmin network is a determinant of the cytoplasmic stiffness of myoblasts: Desmin network: A determinant of the cytoplasmic stiffness of myoblasts** *Biology of the Cell* **110**:77–90
- [53] Pensalfini M., Golde T., Trepat X., Arroyo M. (2023) **Nonaffine Mechanics of Entangled Networks Inspired by Intermediate Filaments** *Physical Review Letters* **131**
- [54] Bi D., Lopez J. H., Schwarz J. M., Manning M. L. (2015) **A density-independent rigidity transition in biological tissues** *Nature Physics* **11**:1074–1079
- [55] Rauzi M., Verant P., Lecuit T., Lenne P.-F. (2008) **Nature and anisotropy of cortical forces orienting Drosophila tissue morphogenesis** *Nature Cell Biology* **10**:1401–1410
- [56] Kale G. R., et al. (2018) **Distinct contributions of tensile and shear stress on E-cadherin levels during morphogenesis** *Nature Communications* **9**
- [57] Merkel M., et al. (2017) **Triangles bridge the scales: Quantifying cellular contributions to tissue deformation** *Physical Review E* **95**
- [58] Bocanegra-Moreno L., Singh A., Hannezo E., Zagorski M., Kicheva A. (2023) **Cell cycle dynamics control fluidity of the developing mouse neuroepithelium**
- [59] Priess J. R., Hirsh D. I. (1986) **Caenorhabditis elegans morphogenesis: The role of the cytoskeleton in elongation of the embryo** *Developmental Biology* **117**:156–173
- [60] Etournay R., et al. (2015) **Interplay of cell dynamics and epithelial tension during morphogenesis of the Drosophila pupal wing** *eLife* **4**
- [61] Lau K., et al. (2015) **Anisotropic stress orients remodelling of mammalian limb bud ectoderm** *Nature Cell Biology* **17**:569–579
- [62] Cost M., Sweeton D., Wieschaus E., Martinez Arias B. (1993) **Gastrulation in Drosophila: Cellular mechanisms of morphogenetic movements** *The Development of Drosophila Melanogaster* :425–465
- [63] Harding M. J., McGraw H. F., Nechiporuk A. (2014) **The roles and regulation of multicellular rosette structures during morphogenesis** *Development* **141**:2549–2558
- [64] Bailles A., et al. (2019) **Genetic induction and mechanochemical propagation of a morphogenetic wave** *Nature* **572**:467–473
- [65] Zusman S. B., Wieschaus E. F. (1985) **Requirements for zygotic gene activity during gastrulation in Drosophila melanogaster** *Developmental Biology* **111**:359–371
- [66] Parks S., Wieschaus E. (1991) **The drosophila gastrulation gene *concertina* encodes a Gα-like protein** *Cell* **64**:447–458

[67] Perkins L. A., Larsen I., Perrimon N. (1992) **Corkscrew encodes a putative protein tyrosine phosphatase that functions to transduce the terminal signal from the receptor tyrosine kinase torso** *Cell* **70**:225–236

[68] Smits C. M., Dutta S., Jain-Sharma V., Streichan S. J., Shvartsman S. Y. (2023) **Maintaining symmetry during body axis elongation** *Current Biology* **33**:3536–3543

[69] Liu Y., Guo Y., Valles J. M., Tang J. X. (2006) **Microtubule bundling and nested buckling drive stripe formation in polymerizing tubulin solutions** *Proceedings of the National Academy of Sciences* **103**:10654–10659

[70] Senoussi A., et al. (2019) **Tunable corrugated patterns in an active nematic sheet** *Proceedings of the National Academy of Sciences* **116**:22464–22470

[71] Heisenberg C.-P., Bellaïche Y. (2013) **Forces in Tissue Morphogenesis and Patterning** *Cell* **153**:948–962

[72] Collinet C., Lecuit T. (2021) **Programmed and self-organized flow of information during morphogenesis** *Nature Reviews Molecular Cell Biology* **22**:245–265

[73] Pinheiro D., Bellaïche Y. (2018) **Mechanical Force-Driven Adherens Junction Remodeling and Epithelial Dynamics** *Developmental Cell* **47**:3–19

[74] Lefebvre M. F., Claussen N. H., Mitchell N. P., Gustafson H. J., Streichan S. J. (2023) **Geometric control of myosin II orientation during axis elongation** *eLife* **12**

[75] Humphrey J. D. (2008) **Vascular Adaptation and Mechanical Homeostasis at Tissue, Cellular, and Sub-cellular Levels** *Cell Biochemistry and Biophysics* **50**:53–78

[76] Latorre E., et al. (2018) **Active superelasticity in three-dimensional epithelia of controlled shape** *Nature* **563**:203–208

[77] Stamenović D., Smith M. L. (2020) **Tensional homeostasis at different length scales** *Soft Matter* **16**:6946–6963

[78] Jodoin J. N., et al. (2015) **Stable Force Balance between Epithelial Cells Arises from F-Actin Turnover** *Developmental Cell* **35**:685–697

[79] Veigel C., Molloy J. E., Schmitz S., Kendrick-Jones J. (2003) **Load-dependent kinetics of force production by smooth muscle myosin measured with optical tweezers** *Nature Cell Biology* **5**:980–986

[80] Laakso J. M., Lewis J. H., Shuman H., Ostap E. M. (2008) **Myosin I Can Act As a Molecular Force Sensor** *Science* **321**:133–136

[81] Barry A. K., et al. (2014) **α-Catenin cytomechanics – role in cadherin-dependent adhesion and mechanotransduction** *Journal of Cell Science* **127**:1779–1791

[82] Mei L., et al. (2020) **Molecular mechanism for direct actin force-sensing by acatenin** *eLife* **9**

[83] Vanderleest T. E., Xie Y., Smits C., Blankenship J. T., Loerke D. (2022) **Interface extension is a continuum property suggesting a linkage between AP contractile and DV lengthening processes** *Molecular Biology of the Cell* **33**

- [84] Wang X., et al. (2020) **Anisotropy links cell shapes to tissue flow during convergent extension** *Proceedings of the National Academy of Sciences* **117**:13541–13551
- [85] Yan L., Bi D. (2019) **Multicellular Rosettes Drive Fluid-solid Transition in Epithelial Tissues** *Physical Review X* **9**
- [86] Tah I., et al. (2023) **Minimal vertex model explains how the amnioserosa avoids fluidization during Drosophila dorsal closure**
- [87] Holley S. A., Ferguson E. L. (1997) **Fish are like flies are like frogs: Conservation of dorsal-ventral patterning mechanisms** *BioEssays* **19**:281–284
- [88] Butler M. T., Wallingford J. B. (2017) **Planar cell polarity in development and disease** *Nature Reviews Molecular Cell Biology* **18**:375–388
- [89] Lavalou J., et al. (2021) **Formation of polarized contractile interfaces by self-organized Toll-8/CirI GPCR asymmetry** *Developmental Cell* **56**:1574–1588
- [90] Schweisguth F., Corson F. (2019) **Self-Organization in Pattern Formation** *Developmental Cell* **49**:659–677
- [91] Lenne P.-F., et al. (2021) **Roadmap for the multiscale coupling of biochemical and mechanical signals during development** *Physical Biology* **18**
- [92] Shindo A. (2018) **Models of convergent extension during morphogenesis** *WIREs Developmental Biology* **7**
- [93] Butler M. T., Wallingford J. B. (2018) **Spatial and temporal analysis of PCP protein dynamics during neural tube closure** *eLife* **7**
- [94] Voiculescu O., Bertocchini F., Wolpert L., Keller R. E., Stern C. D. (2007) **The amniote primitive streak is defined by epithelial cell intercalation before gastrulation** *Nature* **449**:1049–1052
- [95] Saadaoui M., Rocancourt D., Roussel J., Corson F., Gros J. (2020) **A tensile ring drives tissue flows to shape the gastrulating amniote embryo** *Science* **367**:453–458
- [96] Rozbicki E., et al. (2015) **Myosin-II-mediated cell shape changes and cell intercalation contribute to primitive streak formation** *Nature Cell Biology* **17**:397–408
- [97] Dye N. A., et al. (2017) **Cell dynamics underlying oriented growth of the Drosophila wing imaginal disc**
- [98] Dye N. A., et al. (2021) **Self-organized patterning of cell morphology via mechanosensitive feedback** *eLife* **10**
- [99] Hardin J., Weliky M. (2019) **Cell rearrangement induced by filopodial tension accounts for the late phase of convergent extension in the sea urchin archenteron** *Molecular Biology of the Cell* **30**:1911–1919
- [100] Lienkamp S. S., et al. (2012) **Vertebrate kidney tubules elongate using a planar cell polarity-dependent, rosette-based mechanism of convergent extension** *Nature Genetics* **44**:1382–1387

[101] Weng S., Huebner R. J., Wallingford J. B. (2022) **Convergent extension requires adhesion-dependent biomechanical integration of cell crawling and junction contraction** *Cell Reports* **39**

[102] Mitchell N., et al. (2022) **Mitchell, N. et al. Morphodynamic atlas for Drosophila development (2022)**. URL <https://datadryad.org/stash/dataset/doi.10.25349/D9WW43>.

[103] Aigouy B., Umetsu D., Eaton S., Dahmann C. (2016) **Segmentation and Quantitative Analysis of Epithelial Tissues** *Drosophila* :227-239

[104] Guirao B., et al. (2015) **Unified quantitative characterization of epithelial tissue development** *eLife* **4**

[105] Efrati E., Sharon E., Kupferman R. (2009) **Elastic theory of unconstrained non-Euclidean plates** *Journal of the Mechanics and Physics of Solids* **57**:762-775

[106] Ginibre J. (1965) **Statistical Ensembles of Complex, Quaternion, and Real Matrices** *Journal of Mathematical Physics* **6**:440-449

[107] Claussen N. (2023) **Claussen, N. CE simulation public**, [https://github.com/nikolas-claussen/CE\\_simulation\\_public](https://github.com/nikolas-claussen/CE_simulation_public) (2023). URL [https://github.com/nikolas-claussen/CE\\_simulation\\_public](https://github.com/nikolas-claussen/CE_simulation_public).

[108] Virtanen, et al. (2020) **P. SciPy 1.0: Fundamental algorithms for scientific computing in Python** *Nature Methods* **17**:261-272

[109] Thielicke W., Sonntag R. (2021) **Particle Image Velocimetry for MATLAB: Accuracy and enhanced algorithms in PIVlab** *Journal of Open Research Software* **9**

## Editors

Reviewing Editor

**Michel Bagnat**

Duke University, Durham, United States of America

Senior Editor

**Felix Campelo**

Institute of Photonic Sciences, Barcelona, Spain

## Reviewer #2 (Public Review):

Main comment from 1st review:

Weaknesses:

The modeling is interesting, with the integration of tension through tension triangulation around vertices and thus integrating force inference directly in the vertex model. However, the authors are not using it to test their hypothesis and support their analysis at the tissue level. Thus, although interesting, the analysis at the tissue level stays mainly descriptive.

Comments on the revised version:

My main concern was that the author did not use the analysis of mutant contexts such as Snail and Twist to confirm their predictions. They made a series of modifications, clarifying

their conclusions. In particular, they now included an analysis of Snail mutant and show that isogonal deformations in the ventro-lateral regions are absent when the external pulling force of the VF is abolished, supporting the idea that isogonal strain could be used as an indicator of external forces (Fig7 and S6).

They further discuss their results in the context of what was published regarding the mutant backgrounds (fog, torso-like, scab, corkscrew, ksr) where midgut invagination is disrupted, and where germ band buckles, and propose that this supports the importance of internal versus external forces driving GBE.

Overall, these modifications, in addition to clarifications in the text, clearly strengthen the manuscript.

<https://doi.org/10.7554/eLife.95521.2.sa2>

**Reviewer #3 (Public Review):**

In their article "The Geometric Basis of Epithelial Convergent Extension", Brauns and colleagues present a physical analysis of drosophila axis extension that couples *in toto* imaging of cell contours (previously published dataset), force inference, and theory. They seek to disentangle the respective contributions of active vs passive T1 transitions in the convergent extension of the lateral ectoderm (or germband) of the fly embryo.

The revision made by the authors has greatly improved their work, which was already very interesting, in particular the use of force inference throughout intercalation events to identify geometric signatures of active vs passive T1s, and the tension/isogonal decomposition. The new analysis of the Snail mutant adds a lot to the paper and makes their findings on the criteria for T1s very convincing.

About the tissue scale issues raised during the first round of review. Although I do not find the new arguments fully convincing (see below), the authors did put a lot of effort to discuss the role of the adjacent posterior midgut (PMG) on extension, which is already great. That will certainly provide the interested readers with enough material and references to dive into that question.

I still have some issues with the authors' interpretation on the role of the PMG, and on what actually drives the extension. Although it is clear that T1 events in the germ band are driven by active local tension anisotropy (which the authors show but was already well-established), it does not show that the tissue extension itself is powered by these active T1s. Their analysis of "fence" movies from Collinet et al 2015 (Tor mutants and Eve RNAi) is not fully convincing. Indeed, as the authors point out themselves, there is no flow in Tor mutant embryos, even though tension anisotropy is preserved. They argue that in Tor embryos the absence of PMG movement leaves no room for the germband to extend properly, thus impeding the flow. That suggests that the PMG acts as a barrier in Tor mutants - What is it attached to, then? The authors also argue that the posterior flow is reduced in "fenced" Eve RNAi embryos (which have less/no tension anisotropy), to justify their claim that it is the anisotropy that drives extension. However, previous data, including some of the authors' (Irvine and Wieschaus, 1994 - Fig 8), show that the first, rapid phase of germband extension is left completely unaffected in Eve mutants (that lack active tension anisotropy). Although intercalation in Eve mutants is not quantified in that reference, this was later done by others, showing that it is strongly reduced. Similarly, the Cyto-D phenotype from Clement et al 2017, in which intercalation is also strongly reduced, also displays normal extension.

<https://doi.org/10.7554/eLife.95521.2.sa1>

**Author response:**

The following is the authors' response to the original reviews.

***Public Review:******Joint Public Review:******Summary:***

*Brauns et al. work to decipher the respective contribution of active versus passive contributions to cell shape changes during germ band elongation. Using a novel quantification tool of local tension, their results suggest that epithelial convergent extension results from internal forces.*

Reading this summary, and the eLife assessment, we realized that we failed to clearly communicate important aspects of our findings in the first version of our manuscript. We therefore decided to largely restructure and rewrite the abstract and introduction to emphasize that:

- Our analysis method identifies active vs passive contributions to cell **and tissue** shape changes during epithelial convergent extension
- In the context of Drosophila germ band extension, this analysis provides evidence for a major role for internal driving forces rather than external pulling force from neighboring tissue regions (posterior midgut), thus settling a question that has been debated due to apparently conflicting evidence from different experiments.
- Our findings have important implications for local, bottom-up self-organization vs top-down genetic control of tissue behaviors during morphogenesis.

***Strengths:***

*The approach developed here, tension isogonal decomposition, is original and the authors made the demonstration that we can extract comprehensive data on tissue mechanics from this type of analysis.*

*They present an elegant diagram that quantifies how active and passive forces interact to drive cell intercalations.*

*The model qualitatively recapitulates the features of passive and active intercalation for a T1 event.*

*Regions of high isogonal strains are consistent with the proximity of known active regions.*

We think this statement is somewhat ambiguous and does not summarize our findings precisely. A more precise statement would be that high isogonal strain identifies regions of passive deformation, which is caused by adjacent active regions.

*They define a parameter (the LTC parameter) which encompasses the geometry of the tension triangles and allows the authors to define a criterium for T1s to occur.*

*The data are clearly presented, going from cellular scale to tissue scale, and integrating modeling approaches to complement the thoughtful description of tension patterns.*

***Weaknesses:***

*The modeling is interesting, with the integration of tension through tension triangulation around vertices and thus integrating force inference directly in the vertex model. However, the authors are not using it to test their hypothesis and support their analysis at the tissue level. Thus, although interesting, the analysis at the tissue level stays mainly descriptive.*

We fully agree that a full tissue scale model is crucial to support the claims about tissue scale self-organization we make in the discussion. However, the full analysis of such a model is beyond the scope of the present manuscript. We have therefore split off that analysis into a companion manuscript (Claussen et al. 2023). In this paper, we show that the key results of the tissue-scale analysis of the *Drosophila* embryo, in particular the order-to-disorder transition associated with slowdown of tissue flow, are reproduced and rationalized by our model.

We now refer more closely to this companion paper to point the reader to the results presented there.

*Major points:*

*(1) The authors mention that from their analysis, they can predict what is the tension threshold required for intercalations in different conditions and predict that in *Snail* and *Twist* mutants the T1 tension threshold would be around  $\sqrt{2}$ . Since movies of these mutants are most probably available, it would be nice to confirm these predictions.*

This is an excellent suggestion. We have included an analysis of a recording of a *Snail* mutant, which is presented in the new Figures 4 and S6. As predicted, we find that isogonal deformations in the ventro-lateral regions are absent when the external pulling force of the VF is abolished. Further, in the absence of isogonal deformation, T1 transitions indeed occur at a critical tension of approx.  $\sqrt{2}$ , as predicted by our model. Both of these results provide important experimental evidence for our model and for isogonal strain as a reliable indicator of external forces.

*(2) While the formalism is very elegant and convincing, and also convincingly allows making sense of the data presented in the paper, it is not all that clear whether the claims are compatible with previous experimental observations. In particular, it has been reported in different papers (including Collinet et al NCB 2015, Clement et al Curr Biol 2017) that affecting the initial Myosin polarity or the rate of T1s does not affect tissue-scale convergent extension. Analysis/discussion of the *Tor* phenotype (no extension with myosin anisotropy) and the *Eve/Runt* phenotype (extension without Myosin anisotropy), which seem in contradiction with an extension mostly driven by myosin anisotropy.*

We are happy to read that the referees find our approach elegant and convincing. The referees correctly point out that we have failed to clearly communicate how our findings connect to the existing literature on *Drosophila* GBE. Indeed, the conflicting results reported in the literature on what drives GBE – internal forces (myosin anisotropy) or external forces (pulling by the posterior midgut) – were a motivation for our study. We have extensively rewritten the introduction, results section (“Isogonal strain identifies regions of passive tissue deformation”), and discussion (“Internal and external contributions to germ band extension”) in response to the referee’s request.

In brief, distinguishing active internal vs passive external driving of tissue flow has been a fundamental open question in the literature on morphogenesis. Our tension-isogonal decomposition now provides a way to answer this question on the cell scale, by identifying regions of passive deformation due to external forces. As we now explain more clearly, our

analysis shows that germ band extension is predominantly driven by internal tension dynamics, and not pulling forces from the posterior midgut.

We put this cell-scale evidence into the context of previous experimental observations on the tissue scale: Genetic mutants (fog, torso-like, scab, corkscrew, ksr), where posterior midgut invagination is disrupted (Muenster et al. 2019, Smits et al. 2023). In these mutants, the germ band buckles forming ectopic folds or twists into a corkscrew shape as it extends, pointing towards a buckling instability characteristic of internally driven extensile flows.

To address the apparently conflicting evidence from Collinet et al. 2015, we carried out a quantitative re-analysis of the data presented in that reference (see new SI section 3 and Fig. S11). The results support the conclusion that the majority of GBE flow is driven internally, thus resolving the apparent conflict.

Lastly, as far as we understand, Clement et al. 2017 appears to be compatible with our picture of active T1 transitions. Clement et al. report that the actin cortex, when loaded by external forces, behaves visco-elastically with a relaxation time of the order of minutes, in line with our model for emerging interfaces post T1.

We again thank the referees for prompting us to address these important issues and believe that including their discussion has significantly strengthened our manuscript.

**Recommendations for the authors:**

*Minor points:*

*- Fig 2 : authors should state in the main text at which scale the inverse problem is solved. (Intercalating quartet, if I understood correctly from the methods) ? and they should explain and justify their choice (why not computing the inverse at a larger scale).*

We have rephrased the first sentence of the section “Cell scale analysis” to clarify that we use local tension inference. This local inference is informative about the relative tension of one interface to its four neighbors. The focus on this local level is justified because we are interested in local cell behaviors, namely rearrangements. Tension inference is also most robust on the local level, since this is where force balance, the underlying physical determinant of the link between mechanics and geometry, resides. In global tension inference, spurious large scale gradients can appear when small deviations from local force balance accumulate over large distances. We have added a paragraph in SI Sec. 1.4 to explain these points.

*-Fig 2 : how should one interpret that tension after passive intercalation (amnioserosa) is higher than before. On fig 2E, tension has not converged yet on the plot, what happens after 20 minutes ?*

Recall that the inferred tension is the total tension on an interface. While on contracting interfaces, the majority of this tension will be actively generated by myosin motors, on extending interfaces there is also a contribution carried by passive crosslinkers. The passive tension can be effectively viewed as viscous dissipation on the elongating interface as crosslinkers turn over (Clement et al. 2017). Note that this passive tension is explicitly accounted for in the model presented in Fig. 5. Notably, it is crucial for the T1 process to resolve in a new extending junction. In the amnioserosa, the tension post T1 remains elevated because the amnioserosa is continually stretched by the convergence of the germ band. The tension hence does not necessarily converge back to 1. However, our estimates for the tension after 20 mins post T1 are very noisy because most of the T1s happen relatively

late in the movie (past the 25 min mark) and therefore there are only a few T1s where we can track the post-T1 dynamics for more than 20 mins.

We have added a brief explanation of the high post-T1 tension at the end of the section entitled “Relative tension dynamics distinguishes active and passive intercalations”. Further, we have moved up the section describing the minimal model right after the analysis of the relative tension during intercalations. We believe that this helps the reader better understand these findings before moving on to the tension-isogonal decomposition which generalizes them to the tissue scale.

*Page 7-8 / Figure 3: It is unclear how the decomposition into 1) physical shape 2) tension shape 2) isogonal shape works exactly. A more detailed explanation and more clear illustration of what a quartet is and its labels could help.*

We have added a more detailed explanation in the main text. See our response to the longer question regarding this point below.

*-What exactly defines the boundary curve in figure 3E? How is it computed?*

We have added a sentence in the caption for Fig. 3E explaining that the boundary curve is found by solving Eq. (1) with  $l$  set to zero for the case of a symmetric quartet. We have also added a brief explanation immediately below Eq. (1) pointing out that this equation defines the T1 threshold in the space of local tensions  $T_{ij}$  in terms of the isogonal length  $l_{iso}$ .

*-The authors should consider incorporating some details described in the SI file to the main text to clarify some points, as long as the accessible style of the manuscript can be kept. The points mentioned below may also be clarified in the SI doc. The specific points that could be elaborated are: Page 7-8 / Figure 3: It is unclear how the decomposition into 1) physical shape 2) tension shape 2) isogonal shape works exactly. A more detailed explanation and more clear illustration of what a quartet is and its labels could help. The mapping to Maxwell-Cremona space is fine, but which subset is the quartet? For a set of 4 cells with two shared vertices and a junction, aren't there 5 different tension vectors? Are we talking two closed force triangles? Separately, how do you exactly decompose the deformation (of 4 full cell shapes or a subset?) into isogonal and non-isogonal parts? What is the least squares fit done over - is this system underdetermined? Is this statistically averaged or computed per quartet and then averaged?*

We thank the referees for pointing us to unclear passages in our presentation. We hope that our revisions have resolved the referee’s questions. As described above, we have clarified the tension-isogonal decomposition in the main text. We have also revised the corresponding SI section (1.5) to address the above questions. A sketch of the quartet with labels is found in SI Fig. S7A which we now refer to explicitly in the main text.

We always consider force-balance configurations, i.e. closed force triangles. Therefore in the “kite” formed by two adjacent tension triangles, only three tension vectors are independent.

The decomposition of deformation is performed as follows: For each of the four cells, the center of mass  $c_i$  is calculated. Next, tension inference is performed to find the two tension triangles with tension vectors  $T_{ij}$ . Now there are three independent centroidal vectors  $c_j - c_i$  and three corresponding independent tension vectors  $T_{ij}$ . We define the isogonal deformation tensor  $I_{quartet}$  as the tensor that maps the centroidal vectors to the tension vectors. In general this is not possible exactly, because  $I_{quartet}$  has only three independent components, but there are six equations.

The plots in Fig. 3C, C' are obtained by performing this decomposition for each intercalating quartet individually. The data is then aligned in time and ensemble averages are calculated for each timepoint.

For tissue-scale analysis in Fig. 6, the decomposition is performed for individual vertices (i.e. the corresponding centroidal and tension triangles) and then averaged locally to find the isogonal strain fields shown in Fig. 6B, B'.

*- Line 468: "Therefore, tissue-scale anisotropy of active tension is central to drive and orient convergent-extension flow [10, 57, 59, 60]." Authors almost never mention the contribution of the PMG to tissue extension. Yet it is known to be crucial (convergent extension in Tor mutants is very much affected). Please discuss this point further.*

The referees raise an important point: as discussed in our response to major point (2), we now explicitly discuss the role of internal (active tension) and external (PMG pulling) forces during germ band extension. Please see our response to major point (2) for the changes we made to the manuscript to address this.

In particular, we now explain that in mutants where PMG invagination is impaired (fog, torso-like, torso, scab, corkscrew), the germ band buckles out of plane or extends in a twisted, corkscrew fashion (Smits et al. 2023). This shows that the germ band generates extensile forces largely internally. In torso mutants, the now stationary PMG acts as a barrier which blocks GBE extension; the germ band buckles as a response.

The role of PMG invagination hence lies not in creating pulling forces to extend the germ band, but rather in “making room” to allow for its orderly extension. As shown by the genetics mutants just discussed, the synchronization of PMG invagination and GBE is crucial for successful gastrulation.

*-Typos:*

*Line 74: how are intercalations are*

*Line 84: vertices vertices*

*Line 233: very differently*

*Line 236: are can*

*Line 390: energy which is the isogonal mode must*

*Line 1585: reveals show*

*Line 603: area Line 618: in terms of on the*

We have fixed these typos.

<https://doi.org/10.7554/eLife.95521.2.sa0>